Letter of Intent
for
KEK Super B Factory

Part II: Detector

edited by J. Haba

March 10, 2004

Contents

Executive Summary

For the upgrade of the Belle detector in the SuperKEKB project, the first consideration is to maintain the current performance in the very harsh background environment due to the high beam current. The performance of the Belle detector is summarized in the next chapter. To evaluate the possible degradation of the performance due to the extremely high background, we extrapolate the observed background to a level 20 times higher taking the nature of the components of background properly into account.

In the view of vertexing, the silicon micro-strip detector with a shaping time 5 times shorter ($1\mu sec$ to $200nsec$) and a strip length 6 times shorter for the inner layers can have 1/30 of the present occupancy. This may imply that the innermost layer can move even closer to the interaction point than the present one ($1.5cm$) without any loss of vertexing performance. To obtain a robust tracking for low momentum particles, the silicon tracker will be extended out to radius of 15 cm. As for tracking, we can easily reduce the hit loss rate due to overlapping of background by making the time constant in the electronics shorter. Further reduction can be accomplished with the drift cells of half the present size. Simulation studies with overlays of real background taken under current beam conditions show that the degradation of the tracking efficiency for high momentum particles would be small (0.91→0.90) even with 10 times more background. Here a factor of two is included to account for the smaller cell size. The degradation of efficiency for low momentum particles is somwhat larger, 0.94→0.85. We believe we can restore this rather significant loss for low momentum particles by the special reconstruction code currently under development.

On the other hand, the present background level observed in the end-cap part (EECL and EKLM) is rather serious and an upgrade to another advanced technology is necessary. Among several candidates pure CsI crystals with photo tetrode readout is the most promising for the EECL. Bars or tiles of plastic scintillator with a silicon photo multipliers (SiPM) are a good candidate for the replacement of the RPC technology used in the EKLM.

For a particle identification device, the upgrade will be undertaken not only for higher tolerance against background but also for much better K/π discrimination in the momentum range up to 4 GeV/c. Reduction of material in front of the calorimeter and allocation of more tracking volume to CDC is also planned. Among several options to be discussed in the later chapter, the DIRC technology with the Time of Propagation (TOP) scheme is a good candidate for the barrel part while RICH technology with aerogel radiator is considered for the end-cap one. For either option, the development of novel photon detectors with timing resolution better than $100psec$, sensitivity as low as a single photon level and an imaging capability are nedded. The intense R&D work on these is underway. The current plan for the detector configuration is summarized in Fig. 1.

The trigger and data acquisition systems should also be upgraded to handle the 20 times higher occupancy level due to the higher beam current. The DAQ system will be using a pipelined readout scheme in order to cope with the high trigger rate, more than 10kHz, with

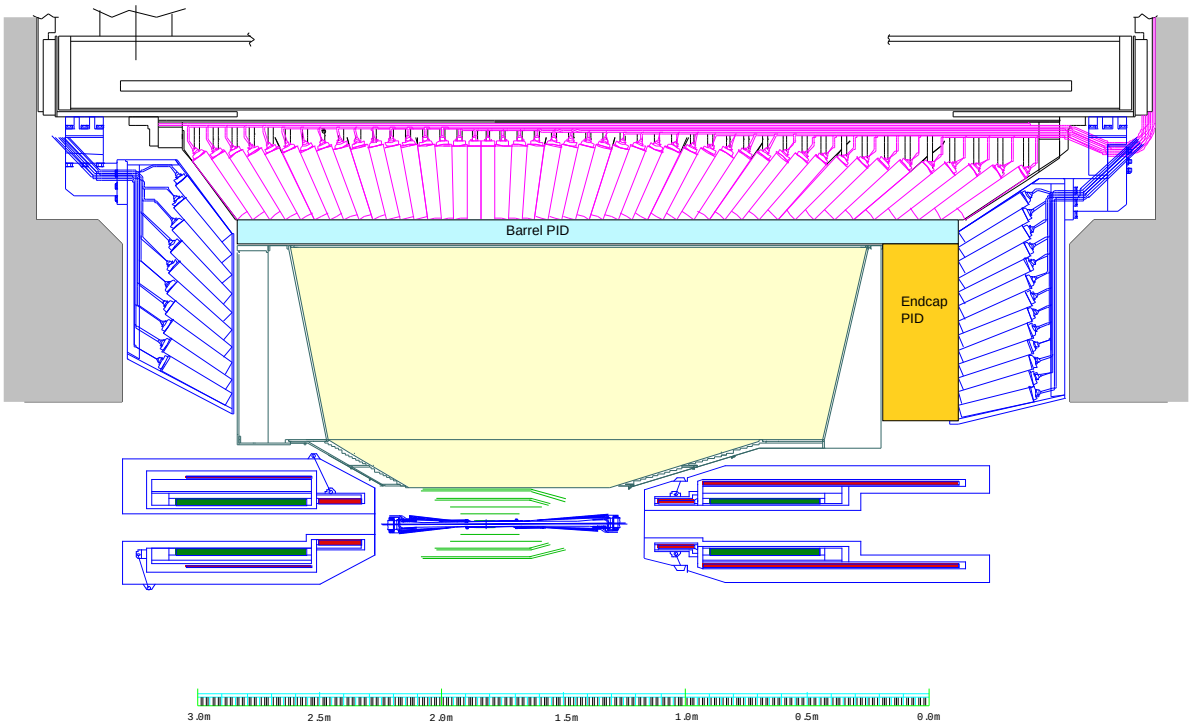

Figure 1: The conceptual illustration of the upgraded Belle.

a low dead time. A readout subsystem consists of a set of modularized common readout platforms called COPPER. They are also modularized and implemented as daughter cards (called as FINNESE) which can be implemented according to various requirements of the detector subsystem. The modules are equipped with a L1 pipeline FIFO so as to record the digitized signal without a readout dead time.

The computing at SuperKEKB is another technological challenge. The online data have to be recorded at a speed of 250 MB/sec after online reconstruction and reduction amounting to the data size of 5 PB/year. Considering the demands from the event skimming and Monte Carlo simulations, we will need a storage system holding 10∼20 PB at the beginning of SuperKEKB, and it should be expandable up to several tens of PB as we take more data. Vast expanding demands are also anticipated in the CPU power and other resources. The GRID technology to be applied in the LHC experiments could be a solution.

Chapter 1

Current performance of the Belle detector

1.1 Beampipe and beam background

The time-dependent CP violation is studied via the measurement of the decay-vertex distribution of the B mesons. It's quality strongly depends on the vertex resolution, and it improves roughly proportional to the inverse of the radius of the innermost layer of the tracker, i.e. depends on the beampipe radius. However, a reduction of the beampipe radius usually results in an increase of beam-induced backgrounds [45]. There are two background sources needed to be considered: synchrotron radiation (SR) and showers from scattered beam particles by the residual gas or intra-beam scattering (Particle background). Another concern is that higher beam currents produce more heating of the beampipe components. High background and high temperature conditions cause the serious aging of the detector and the beampipe itself. Thus, the interaction point (IP) chamber must be designed to realize the low background and the low heating condition.

We had serious background at the begining of the Belle experiment in 1999. We modified the IP chamber by trial and error, and it achieved much lower background than before. In 2003, we reduced beampipe radius from 2.0 cm to 1.5 cm as well as the vertex detector upgrade from SVD 1.6 to SVD 2.0. The IP chamber for the SVD 2.0 is designed based on simulations of the backgrounds, the heating and the cooling. The simulations are developed to reproduce measurements with SVD 1.x. We would like to reduce the beampipe radius down to 1.0 cm in Super-KEKB. The basic design of the IP chamber will be almost same as the SVD 2.0, while there will be some minor differences. That's why the design and performance of the IP chamber for SVD 2.0 is the most important key for the Super-KEKB.

1.1.1 Synchrotron Radiation Background

Simulation Tools

There are two types of the SR's which come into the interaction region. One of them comes from the upstream steering magnets, whose critical energy is a few keV. Another one is the backscattered high-energy photon, SR from QCS-R whose critical energy is about 40 keV, which is scattered in QC2RE chamber. Due to the each energy regions, the former is called 'Soft-SR' and the latter is called 'Hard-SR'.

The simulation consists of the two parts, the simulation of the SR generation and the simu-

lation in the detector. For the detector simulation part, it is important to handle the very low energy interaction at least down to 1 keV and the photo-electric effect for example L-edge x-rays of the gold. The EGS4 [46] (improved version) and the Geant4 [47] fulfill our demands.

Soft-SR

This simulation is performed by using 'srw' (synchrotron radiation wattage program). The srw calculate the SR photons from each magnets. The position and angle of SR hits on various surfaces, together with the energy spectrum and power are passed on to the detector simulation program based on the EGS4.

Hard-SR

When HER electrons exit Belle, they traverse QCS-R off axis by 4 cm where they experience a ~ 0.8 T magnetic field and radiate an enormous number of high energy photons whose critical energy is ~ 40 keV. These photons hit around the downstream (~ 9.5 m) chamber of QC2RE. The scattered photons come back to the detector. The simulation is also separated into the two parts, the simulation of the backscattering and the detector simulation. The position, direction and energy of the Hard-SR photons at the QCS-R, which include the effect of the beam-size and the dynamic effects, are passed to the simulation in the OC2RE based on the Geant4. The information of the backscattered photons are passed to the detector simulation.

The experience in SVD1.x and the comparison with the simulation

During the Summer 1999 operation of Belle, we had two serious problems. The gain of readout chips at the innermost layer of the SVD 1.0 were suddenly dropped and they were broken for two weeks as shown in Figure 1.1. We measured energy spectrum of SVD hits using a special 'single bunch' operation mode. In this mode, the storage ring contained only one train of several bunches closely placed together with total current of about 10 mA, The SVD signal pulses have a decay time of about 1 μsec, while the train takes 10 μsec in one turn. The trigger timing was adjusted for the timing of the train, so called revolution trigger. Figure 1.2 shows the energy spectra taken during the summer 1999 without (top) and with (middle) limits placed on the strength of the steering magnets. The background was reduced in the low energy region less than 25 keV. The failure condition of the steering magnets generated the much Soft-SR, and it was identified as a source of this trouble. The simulation reproduces the azimuthal angle distribution of the gain drop caused by the radiation as shown in Figure 1.3. With average 6.7 mA current, more than 300 kRad radiation dose deposited at that period while the dose required to kill the SVD 1.0 is 200 kRad. Most of Soft-SR backgrounds were generated from the QC1 and BC3 magnets. After this trouble, we avoid it with limit on the strength of the steering magnets.

Another problem is that the CDC and the SVD had a serious background from the Hard-SR. During the summer 1999 shutdown, mylar with a 20 μm-thick gold layer was wrapped around the beryllium section of the beampipe in order to reduce the SR backgrounds. Outside of the fiducial region was further protected by 300 μm of gold. The flux of Hard-SR is depends on the square of the distance from IP to the photon-stop chamber. We changed the distance from $\sim$6 m to $\sim$9.5 m, its reduction factor is $\sim$0.44. We also changed chamber material from aluminum to copper, the background was reduced to 1/3 according to the simulation. The energy spectra of the Hard-SR as aluminum and copper chamber cases are shown in Figure 1.4. The 8 keV K-edge x-rays from copper actually carry more wattage to the interaction region than the case of the aluminum, but the gold coating reduces it to a negligible level. The bottom histogram in

Figure 1.2 shows the energy spectrum taken after these modifications in the interaction region region. The Hard-SR was reduced to ($\sim 1/10$).

We changed the gold coating from outside 20 μm to the inside 10 μm thickness of the beryllium, later. The inside coating is better than outside one as shown in Figure 1.5 because the incident angle of SR to the gold, i.e. the path-length in the gold, is changed by the scattering in the beryllium.

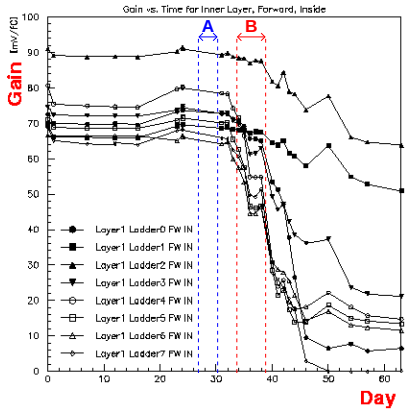

Figure 1.1: Gains of the readout chips of SVD 1.0 as a function of time, during summer 1999.

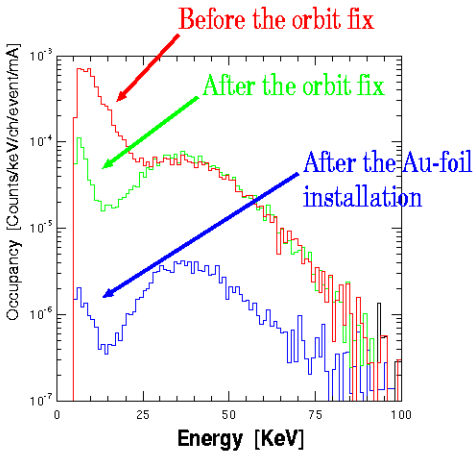

Figure 1.2: The SVD energy spectra taken with single bunch operations. The top histogram is for the run during summer 1999 without limit on steering magnet strength, the second from top is the same with a limit on the steering magnets, and the bottom histogram is the energy spectrum after the modifications described in the text.

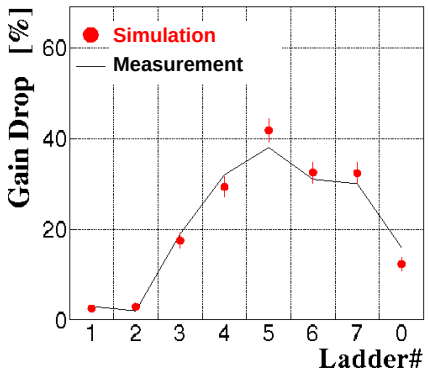

Figure 1.3: The azimuthal angle distribution of the SVD gain drop during the 5.6 days which is the period 'B' in the Figure 1.1

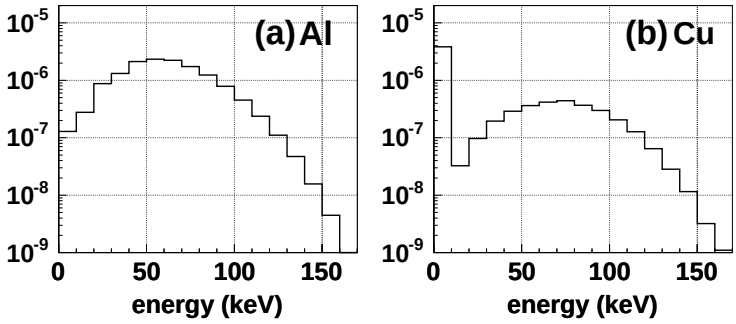

Figure 1.4: Energy spectra of the backscattered photons from the QC2RE chamber to IP whose materials are (a) aluminum and (b) copper in the simulation. The same distance from QC2RE to IP is used in both case.

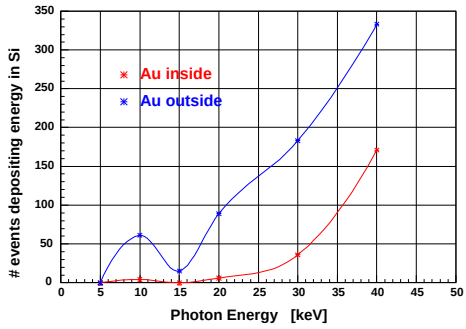

Figure 1.5: The comparison of the gold-coating effectiveness between the inside and outside coating of the beryllium beampipe in the simulation. The inside coating is better than the outside case.

1.1.2 Particle Background

Simulation Tools

We are considering three types of Particle backgrounds, which derived from Bremsstrahlung, Coulomb scattering with the residual gas and Touschek effect (intra-beam scattering). We uses the Decay-TURTLE program package [48] for the beam transport and beam-gas scattering. Even though the scattering location can be anywhere in the ring, the simulation is limited to single turn (multi-turn effects are not simulated). The total scattering cross section for Bremsstrahlung or Coulomb is calculated for given residual gas. The rate of scattering is obtained for the given beam length (entire ring) and the pressure (assuming uniform distribution) as well as for the kinematic cutoffs used for the scattering. The simulation starts at the IP where the beam profile is calculated from the beam optics and the position and direction of one beam particle is generated. The particle is traced up to the pre-selected scattering point where the scattering angle is generated for Coulomb or the energy loss is generated for Bremsstrahlung. Then the scattered particle is traced down the beam line as before.

The momentum vector of a particle after Coulomb scattering is sampled using the approximate relation: $d\sigma/d\theta \propto \sin^{-3}\theta$, where θ is the angle between the momenta before and after scattering with cutoff at a minimum of 0.001 rad. The azimuthal angle is uniform between 0 and 2π. The scattered particle is assumed to change the direction only keeping the same absolute energy. In sampling for the bremsstrahlung, it is assumed that the participating particle does not change its direction. Furthermore, the resulting photon is discarded at this time. The final energy of the particle after bremsstrahlung is take to be [49]: $E = (1 - \varepsilon)E_{beam}$, where E_{beam} is the beam energy, and ε is generated by GEANT3 [50] subroutine GPREME with a cut at a minimum value of ε of 0.05. The Touschek effect is also change (gain and loss) the energy of the beam particles. It is also take into account at the whole of the ring uniformly. The average of the bunch size is assumed, while the actual size is changing with the β oscillation.

If a traced particle survives until the entrance of the QC2 magnet on each side of the IP, it is transferred to 'gsim' which is the simulation of the Belle detector based on GEANT3 [50]. The gsim follows the particle through the detector elements, simulating electromagnetic showers, and keeping track also of its energy losses. Materials associated with magnets and beamline chambers are carefully implemented in order to simulate the development and absorption of showers outside the beampipe.

Currently, the uncertainty of the simulation must be the scale of its factor. In order to reduce the background, the movable masks are put in the both rings. They cuts the tail of the beams. The simulation is considering the reduction by the masks. But, actual relative position between the mask height and beam orbit has large uncertainty. Moreover, the measured pressures are lower than the actual pressures because its sensors are monitoring close to the pumps. Its uncertainty is the factor of a few.

Comparison of the Simulation with the Data in SVD1.4

On December in 2000, we measured radiation dose at the first layer of the SVD 1.4 in each single beam runs. The peak beam currents were 0.5 A for HER and 0.7 A for LER. The measurement dose and the expectation from the Particle background simulation are listed in Table 1.1, where the beam currents are scaled to 1.1 A (2.6 A) for HER (LER) and the vacuum for CO is scale for the 1nTorr. The contribution of the SR background was less than a few kRad/yr. The simulation reproduced the measurement within a factor of a few.

Table 1.1: Comparison of the radiation dose (kRad/yr) on the first layer of the SVD 1.4 between the measurement and the simulation in the single beam runs, where the beam currents are scaled to 1.1 A (2.6 A) for HER (LER) and the vacuum for CO is scale for the 1nTorr.

	measurement	simulation	(	Brem,	Coulomb,	Touschek	)
HER	24	40.5	(	5.9,	34.6,	—	)
LER	82	91.7	(	20.4,	14.8,	56.5	)

1.1.3 SVD2 Beampipe: Design and Status

Design

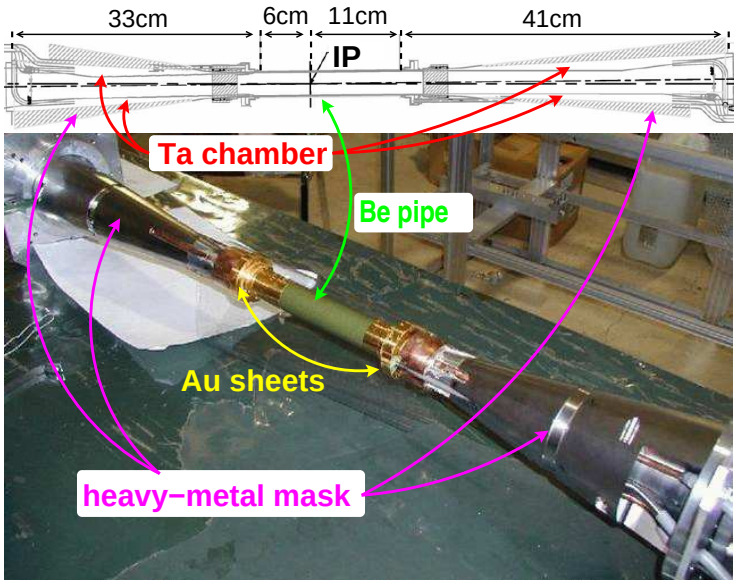

Figure 1.6: The outside view of the beampipe.

We designed SVD 2.0 based on the simulations. The outside view of the beampipe is shown in Figure 1.6. The IP region is consists of two layers of beryllium pipes. Their thicknesses are 0.6 mm for the inner-side and 0.35 mm for the outer-side. There is 0.5 mm space between two pipes for the circulation of the cooling liquid, normal paraffin oil (C_nH_{2n+2}, $n \sim 12$). It is circulated with about 1.15 l/min flow rate, and its temperature is kept 14 °C at the inlet. Its cooling power to 100 W heating is confirmed by the mockup test. In order to reduce the background, the massive Tantalum chambers are jointed to the both sides of the beryllium pipes, and the tungsten heavy metals cover them. The cooling water tubes exit between these metals. The total weight of the IP chamber is 40 kg. Since showers not well contained increase the background, the masks are shaped such that the path length of most particles exceeds 16 radiation length. The Particle background is reduced by factor 2.0 $\sim$ 2.5 due to the inner shape of Tantalum pipes is parallel to the incoming beam for both HER and LER beams. The expected radiation dose from the Particle backgrounds at each layers of the SVD is summarized in Table 1.2. We expected around 70 $\sim$ 80 kRad dose per 100 days operation.

In order to reduce the SR background, the inside of the Be section are coated by the gold

Table 1.2: The radiation dose at each layers of SVD according to the Particle background simulation, where the beam currents are 1.1 A for HER and 1.6 A for LER, and 100 days operation is assumed in a year. the vacuum for CO is 1nTorr are assumed. The error is statistical error of MC.

	L1	L2	L3	L4
HER : Bream.	21.1 ± 4.0	8.3 ± 1.2	2.1 ± 0.2	1.0 ± 0.1
HER : Coulomb	31.7 ± 10.2	8.5 ± 2.0	2.7 ± 0.5	1.5 ± 0.4
LER : Bream.	8.4 ± 1.7	2.5 ± 0.5	0.6 ± 0.1	0.3 ± 0.1
LER : Coulomb	6.0 ± 1.4	1.2 ± 0.2	0.3 ± 0.1	0.2 ± 0.1
LER : Touschek	6.3 ± 3.0	2.3 ± 1.3	0.2 ± 0.1	0.1 ± 0.1

(10 μm). The section outside the tracking regions and the Be-Ta joint section (manifold region) are also covered by the 300 μm thickness of the gold on the outside radial surface. The photon absorption length for various materials are shown in Figure 1.7. The gold absorbs low energy (<8 keV) SR, and high energy SR is converted to less than 20 keV photons via absorption and the photo-electric effect. The beampipe tilt by 11 mrad with respect to the Belle axis (LER axis) makes shallower angle to the HER beam than before. Thus, the block of the Soft-SR is much easier. The inner surface of the Tantalum at the HER upstream side is sawtooth shape. Due to it, the upstream surface of the sawtooth cannot see the beryllium beampipe, and the downstream surface cannot see the single-bounce photons. The HOM loss due to the sawtooth is substantially reduced by the varying-angle design as shown in Figure 1.8.

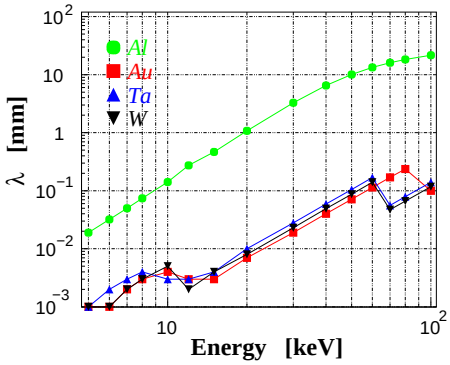

Figure 1.7: Photon absorption length for various materials.

A crescent shape shield (SR-mask) is put on the 9 cm HER upstream from the IP, its inner radius is 1.2 cm and maximum hight is 2 mm. Due to the gold coating, the beampipe tilt and the SR-mask, a few kRad/yr or less radiation dose is expected from the Soft-SR with 1.1 A HER current. At the another side of the beampipe (downstream of the HER), There is no SR-mask to avoid the HOM heating at the beryllium section. More Hard-SR is expected than before due to it, but the Hard-SR cannot incoming to the detector region directly because of its too low input angle into the beampipe (11 mrad) and the Tantalum masks. The Tantalum chamber completely shields the Hard-SR, while the previous beampipes couldn't stop it because they were made by aluminum. Thus, the Hard-SR background into the SVD is scattered or re-emitted in the gold coating, and the expected dose is only 29 ± 3 kRad/yr at 1.1 A HER current, where the error

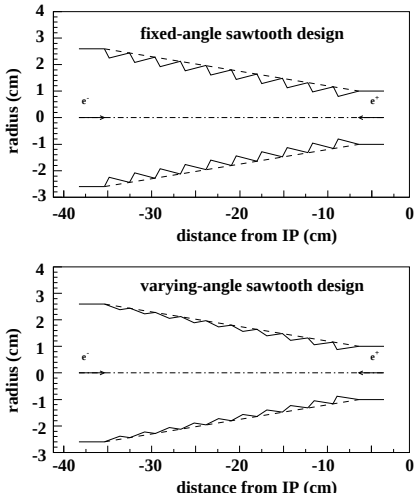

Figure 1.8: The inner surface of the Tantalum mask at the HER upstream side. The fixed-angle and varying-angle sawtooth designs are shown on top and bottom respectively.

is estimated from the uncertainties of the beam orbit (COD error) and the beam-size.

The radiation and the temperature sensors are put on the various place around the beampipe and the SVD. There are 12 dose rate sensors (PIN), 24 integrated dose sensors (RadFET) and 50 temperature sensors (RTD). The PIN and the RadFET are put around on the both manifold regions almost every 60 degree, which close to the readout chips for the first layer of the SVD. Moreover, the RadFET's are put on the both edges of the second and third layer of SVD almost every 120 degree. The RTD's are located on the beryllium beampipe, around manifolds, and below the heavy-metal masks.

Background status

Currently, the beam currents are 1.1 A for HER and 1.6 A for LER at maximum. The average vacuum pressures in the both rings are around 0.8 nTorr for HER and 0.5 nTorr for LER. Measured pressures should be lower than beam position because we only measure them near the vacuum pumps

We can calculate the radiation dose by using the energy deposition on the SVD, i.e. the energy spectrum of SVD and hit-rate. On Nov 21, 2003, we took the HER single beam run data with 'single bunch' operation mode at 15 mA HER current. We can measure the SR background with assuming that the contribution of the Particle background should be low in such a low current. The energy distribution at the first layer of the SVD is shown in Figure 1.9. Due to the Tantalum mask, the higher energy component is not observed in Figure 1.9, while there was it clearly at SVD 1.x as shown in Figure 1.2. Contrastively, the lower energy component is roughly 10 times higher than before. We expected more Hard-SR due to removing the SR-mask at downstream side. The azimuthal angle distribution of the events at the first layer of the SVD indicates that the dominant background is the Hard-SR (Figure **??**). Larger dose are detected at at backward side region (BWD) than forward side region (FWD), where the backward side is the upstream side in the HER and the forward is opposite side. The radiation dose is the maximum at the inner-side direction of the ring for BWD side. The maximum dose is given to the inner-side (horizontal) direction of the ring. It is extrapolated to be 33 kRad/yr

at 1.1 A HER current, where the contribution below the threshold (10 keV) is corrected with the simulation [1]. It is consistent with the expectation.

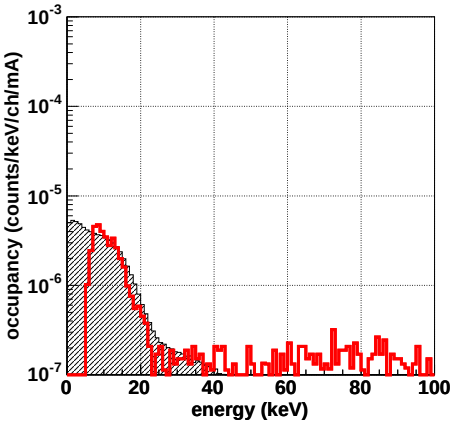

Figure 1.9: The SVD 2.0 energy spectra taken with single bunch operations in Nov 21, 2003 (open histogram) and the expectation from the Hard-SR simulation (hatched histogram), where the energy resolution is assumed 2 keV.

It is difficult to observe the energy spectrum of the Hard-SR in the high energy region more than 30 keV because of the existence of the Particle background. Energy spectra of the HER (0.8 A) and the LER (1.5 A) single beam runs with 1,284 bunches and random trigger are shown in Fiugre **??**. The spectrum shape of the HER is clearly different from the LER. There are SR and Particle background in the HER run, while there is only Particle background in the LER run. We can measure the SR and the Particle background seperately from the HER energy spectrum if the energy spectrum of the Particle background is same as that in LER. We checked that the spectrum shape of the Particle background in HER is same as the LER one. The spectrum difference between worse vacuum and better vacuum in the HER single beam run must be the spectrum of the Particle background. It is same as the LER spectrum as shown in Figure 1.10. The extracted energy spectra of the SR and the Particle backgrounds in HER single beam run is shown in Figure 1.11.

The higher energy component of the SR is observed as the sholder around 50 keV. The Particle background in HER is proportional to (beam-current)$\times$(pressure) while the SR is proportional to the beam-current. Thus, the ratio $N_{particle}/N_{SR}$ in the HER single beam should reproduce the current dependence of the HER pressure, where the $N_{particle}$ is the number of clusters for Particle background and the N_{SR} is for SR. Its ratio well reproduced the current dependence of the vacuum in the HER ring.

The dose from the SR is extrapolated to be 21 kRad/yr in 1.1 A HER current. Its azimuthal angle distributions are also consistent with the Hard-SR simulation. The maximum dose is given to the outer-side direction of the ring for the Particle background. We can also extrapolate the doses with assuming the correlation with the square of currents for the Particle background. In 1.1 A HER current, the Particle background is 44 kRad/yr while the expectation is 53 kRad/yr, they are consistent. However, the Particle background in LER is 43 kRad/yr while the expectation is 21 kRad/yr in 1.6 A current. The overestimation of the Touschek effect is the reason for such a large difference of the LER background.

[1] The Contribution above the threshold is 2/3 of the total dose.

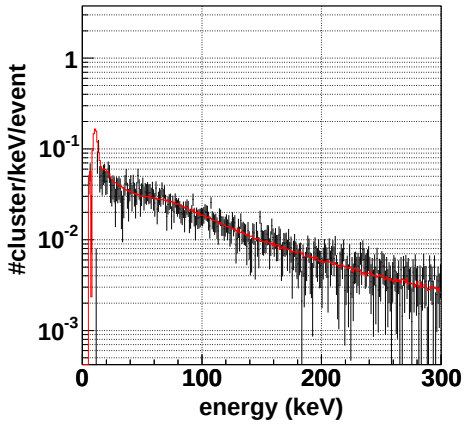

Figure 1.10: Difference of the energy spectrum between normal vacuum condistion and worse vacuum condiction at the same current 0.8 A (cross marker), and the energy spectrum of the Particle background in LER (open histogram). Turn on and off of the vacuum pump (H03 which is 15 m upstream from the detector) makes different vacuum condition. This spectrum difference indicates the energy spectrum of the Particle background in HER. The LER spectrum is normalized with the HER spectrum.

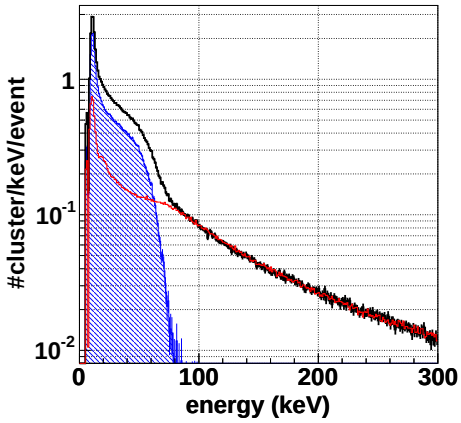

Figure 1.11: Energy spectra in single beam runs in the HER single beam run at 0.8 A (thick histogram), extracted SR background (hatched histogram) and extracted Particle background (thin histogram).

The correlation between the background and the vertical beam-size of LER is shown in 1.12. The background is lower when the beam-size is larger. The beam size at collision is larger than the single beam case when we use the same parameters for the operation. That's why the background in the LER single beam is over estimated. The Touschek contribution is about 20 % or less at the collision, while 50 % contribution at the single beam and 31 % contribution in the simulation. Its contribution should be corrected. In 1.6 A LER current, the backgrounds are corrected to 22 kRad/yr for the measurement and 18 kRad/yr for the simulation. The radiation doses for each sides of the horizontal direction are summarized in Table 1.3. Total dose is 83 (76) kRad/yr at the outer-side (inner-side), it is consistent with design values within factor a few. This is lower than the dose of 100 kRad/yr with the previous beampipe even though the beampipe radius is smaller. The contribution of the SR is high at inner-side direction, which is about 40 % of the total. The contribution ratio between the SR and the Particle backgrounds are also consistent with the expectation.

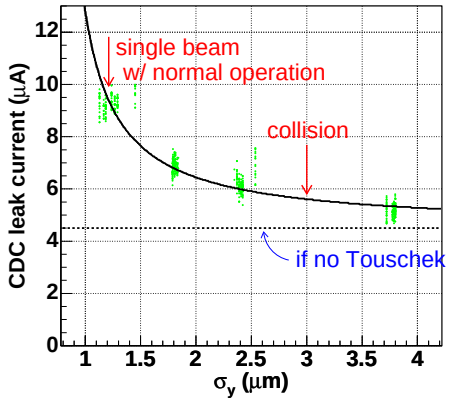

Figure 1.12: Correlation between CDC leak current and the LER vertical beam size. The background is larger with smaller beam size. The beam size is different for collision because of beam-beam effects, thus it is larger than the case of the single beam. That's why the background which measured with the single beam is larger than the case of the collision.

Table 1.3: Radiation doses (kRad/yr) at 1.1 (1.6) A current for HER (LER) for each backgrounds (BG). The values in the brackets indicates expected values of the simulation.

	outer-direction	inner-direction
Particle-BG (LER)	22 (18)	14 (11)
Particle-BG (HER)	44 (53)	29 (33)
SR-BG	17 (8)	33 (29)
total	83 (79)	76 (73)

Heating and cooling power

The beampipe may have a thermal stress from the heating. For the long term operation, reduction of the heating by cooling are very important. There are three sources of heating that

need to be considered: synchrotron radiation, image current heating and HOM (higher-order-mode) heating. We can simulate the heating from SR using the tool for the SR backgrounds.

The heating and the cooling power are also confirmed in the real operation, the temperature rise is less than 1.2 degree at the Be section and it is less than 6.5 degree at the hottest region at Ta chamber. We measure the correlation of the beam currents and the temperature difference of the cooling paraffin between inlet and outlet in single beam runs. The heating from each beams are extrapolated 30 W at 1.5 A of HER current and 65 W at 2.5 A of LER, the total amount of the heating is 95 W while the design value is 100 W.

1.2 Silicon Vertex Detector (SVD)

The Silicon Vertex Detector (SVD) plays a central role in measuring time-dependent CP violation in the neutral B meson system, which is the primary purpose of the present Belle experiment at the energy-asymmetric e^+e^- collider KEKB. The measurements of CP asymmetry parameters require that the resolution of the vertex detector be (at least) better than the average flight distance of B mesons, which is about 200 μm at KEKB. Thus a natural choice was to use double-sided silicon strip detectors (DSSDs) that provide good intrinsic resolution while the amount of material inside the detector acceptance can be kept sufficiently low.

The SVD system has been upgraded several times since the commissioning of the Belle experiment, as listed in Table 1.4. This was in part due to the need for replacing damaged

Name	Installation	Comments
SVD1.0	Dec. 1998	Readout VLSIs with modest (up to ∼200 kRad) radiation hardness (VA1 [1] with AMS 1.2 μm process). Layer 1 (forward, innerside) damaged by unexpected X-rays.
SVD1.2	Sep. 1999	Layer 1 replaced. Gold foil (20 μm thick) on the outer surface of the Beryllium beampipe.
SVD1.4	Aug. 2000	Improved DSSD design ("atoll" design) for the N-side. Semi-radiation-hard readout VLSI (VA1 with AMS 0.8 μm process). Gold foil (10 μm thick) on the inner surface of the Beryllium beampipe. Vacuum leak found in the IP beampipe.
SVD1.6	Dec. 2002	SVD1.2 beampipe restored. Dead DSSD ladders replaced.
SVD2.0	Aug. 2003	A major upgrade (see Table 1.5 for design details).

Table 1.4: History of the Belle SVD upgrade.

detectors and a beampipe, but we also aimed at improving the performance and radiation tolerance. In the following, SVD1.0, SVD1.2, SVD1.4 and SVD1.6 are collectively called SVD1 since they have the same configuration and thus the similar performance. The configuration of SVD1 (SVD2) is shown in Fig. 1.13 (Fig. 1.14). Characteristics of these detectors are also listed in Table 1.5. More details can be found elsewhere [2].

	SVD1	SVD2
Beampipe radius (mm)	20	15
Number of layers	3	4
Number of DSSD ladders in layers 1/2/3/4	8/10/14/NA	6/12/18/18
Number of DSSDs in a ladder in layers 1/2/3/4	2/3/4/NA	2/3/5/6
Radii of layers 1/2/3/4 (mm)	30.0/45.5/60.5/NA	20.0/43.5/70.0/88.8
Angular coverage (acceptance)	$23 < \theta < 140°$ (0.86)	$17 < \theta < 150°$ (0.92)
Total number of channels	81920	110592
Strip pitch (μm) for z	84	75 (73 for layer 4)
Strip pitch (μm) for $r\phi$	25 (50 for readout)	50 (65 for layer 4)
DSSD thickness (μm)	300	300
Total material at $\theta = 90°$ (%X_0)	1.85	2.6
Readout VLSI	VA1	VA1TA
Radiation tolerance (MRad)	∼1	>20
Intrinsic DAQ deadtime/trigger (μs)	128	25.6

Table 1.5: Characteristics of SVD1 and SVD2.

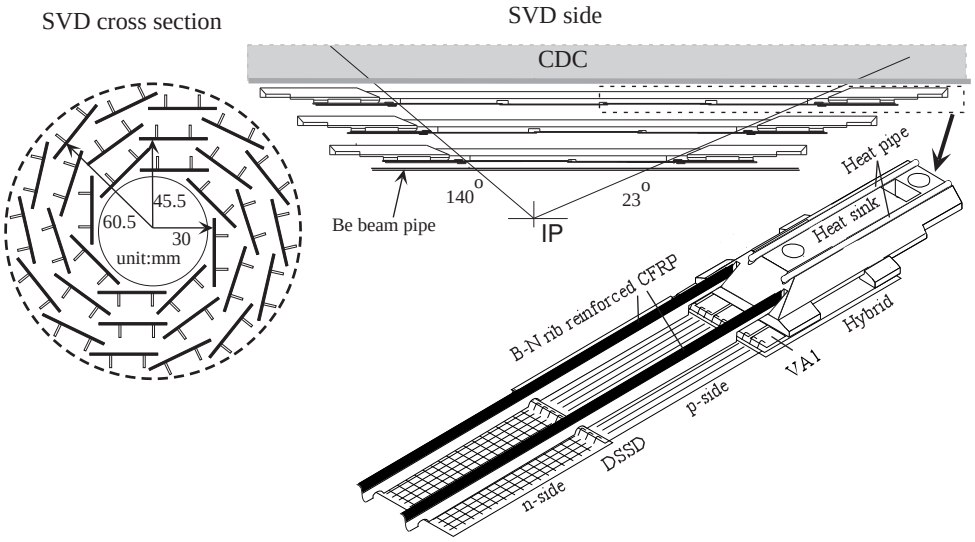

Figure 1.13: Configuration of the SVD1.

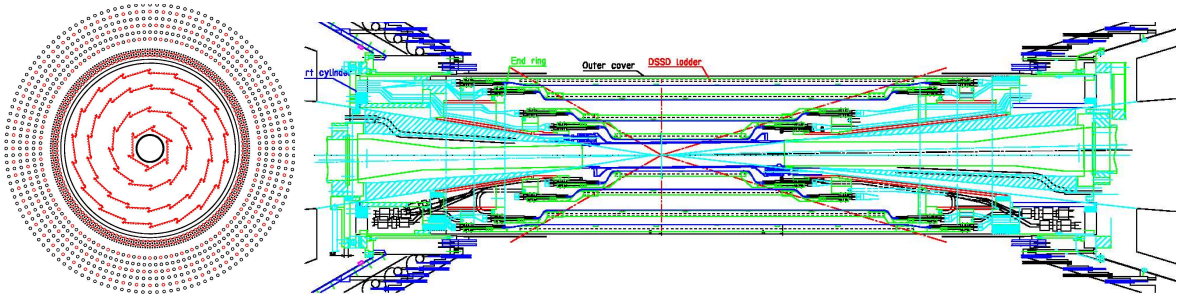

Figure 1.14: Configuration of the SVD2.

Table 1.6 summarizes the performance of the SVD. The basic performance of the SVD can be evaluated from its stability, robustness against noise and background, efficiencies and resolutions. In general we have experienced very stable operations for both SVD1 and SVD2. Therefore there has been no problem in the stability. One exception, however, was the pin-hole problem in the SVD1. In the SVD1, a break-down of a coupling capacitance on a DSSD, which happened a few times a year, induced a big noise due to a huge current flowing into the VA1 chip. This problem was solved in SVD2 by introducing the floating-ground scheme in which no voltage difference is applied between the strip and the readout electrode. Signal-to-noise ratios (S/N) are also satisfactory; simulation studies indicate that $S/N > 10$ is necessary, and indeed that is guaranteed in all layers even after irradiation due to the beam operation. The largest degradation of 30% is observed in the layer 1 ladders of SVD1 for a total radiation dose of about 0.9 MRad. Typical S/N values in SVD1 were 35, 19 and 17 for the p-side of short half-ladders, the n-side of short half-ladders, and long half-ladders, respectively. For the SVD2, we obtain 36, 30, 21, 21 for the p-side of layer 1, 2, 3, 4, and 36, 24, 16, 19 for the n-side of layer 1, 2, 3, 4.

The strip occupancy in the layer 1 of SVD1 was $\sim$6 %. The occupancy was increased in SVD2 due to the fact that the layer 1 is closer to the beamline. The average occupancy is 10%, 3.5%, 2% and 1.5% for layer 1, 2, 3 and 4, respectively.

As regards efficiencies of the system, one important requirement is that the deadtime during the operation be small. The original design goal at Belle was to keep the readout deadtime below 10% at the level-1 trigger rate of 500 Hz. While this was marginally achieved in SVD1 because of the rather large intrinsic deadtime, the situation is much improved in SVD2 since each VA1TA1 chip is read out in parallel. There is another source of deadtime common to SVD1 and SVD2, which is the deadtime due to the pre-triggering. The peaking time of the VA1TA1 shaper circuitry is set at around 1 μs, while the level-1 trigger latency is 2.5 μs. Therefore we send a pre-trigger (called the level-0 trigger) in prior to each level-1 trigger. Since it is made of ToF signals, the level-0 trigger rate is higher than the level-1 rate. This causes non-negligible deadtime and thus inefficiency in the SVD system as shown in Fig. 1.15.

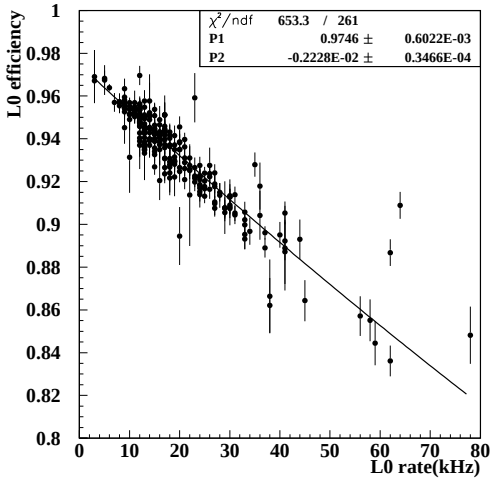

Figure 1.15: Level-0 trigger efficiency vs. level-0 trigger rate.

To evaluate efficiencies in terms of track reconstruction, we define "matching efficiency" as the fraction of CDC tracks within the SVD acceptance that have associated SVD hits in at least two layers, and in at least one layer with both $r\phi$ and z information. In other words, this

provides the probability that a track that travels through the SVD can be used for B decay vertex reconstruction. The track extrapolation from the CDC was done using the Kalman filtering technique. Tracks from K^0_S decays were excluded since these tracks do not necessarily go through the SVD. The inefficiency can be attributed to dead channels of the SVD, fake SVD clusters, and some imperfection in the SVD-cluster finding as well as in track reconstruction with the CDC. The average matching efficiency is found to be around 98% for both SVD1 and SVD2, which agrees with an expectation from Monte Carlo simulation. Figure 1.16 shows the momentum and angle dependence of the matching efficiency in SVD2.

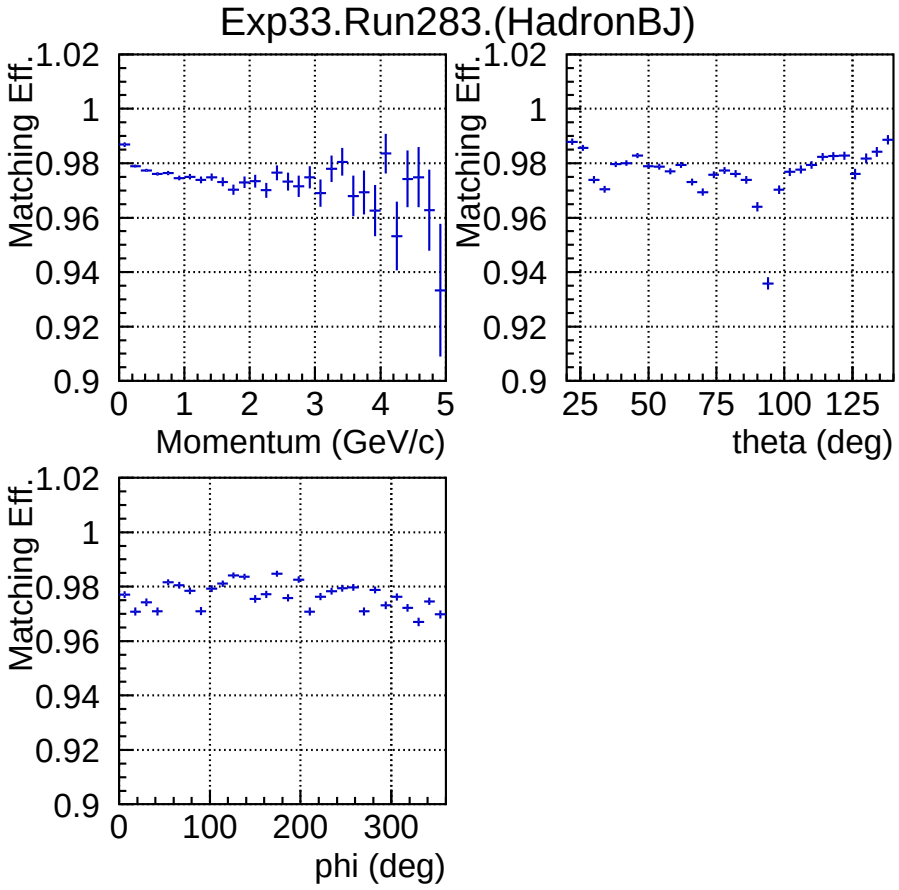

Figure 1.16: Matching efficiencies in SVD2 vs. (top-left) momentum, (top-right) θ and (bottom-left) ϕ.

The most important basic parameter among many others that indicate the performance of the SVD is the impact parameter resolution. Figure 1.17 shows the impact parameter resolutions for the helix parameters dz and $d\rho$, respectively. These are obtained from cosmic ray events taken simultaneously during the collision data taking; i.e. the effects of beam-originated backgrounds are included. The momentum as well as angular dependence is well represented by the following formulae for the SVD1:

$$\sigma_{dz} = 42 \oplus 44/p\beta \sin(\theta)^{5/2} [\mu m], \tag{1.1}$$

$$\sigma_{d\rho} = 19 \oplus 54/p\beta\sin(\theta)^{3/2}[\mu m], \tag{1.2}$$

and for the SVD2

$$\sigma_{dz} = 28 \oplus 32/p\beta\sin(\theta)^{5/2}[\mu m], \tag{1.3}$$
$$\sigma_{d\rho} = 22 \oplus 36/p\beta\sin(\theta)^{3/2}[\mu m], \tag{1.4}$$

where p, β and θ are the momentum (in GeV/c), velocity, and the polar angle of the track, respectively. An advantage of the smaller radii of the beampipe and the innermost DSSD layer in SVD2 is clearly seen. At the Super-KEKB, the background level is expected to be much higher than present. Degradation of vertex resolutions due to the larger background will be discussed in Section 2.3. The vertex resolutions of SVD1 and SVD2 are also explained in the same section.

Parameter	SVD1	SVD2
S/N	> 17	> 16
Occupancy in layer 1 (%)	$\sim$6	$\sim$10
Matching efficiency (%)	98	98
Impact parameter resolution for dz ($p = 1$ GeV/c, $\theta = 90°$)	61	42
Impact parameter resolution for $d\rho$ ($p = 1$ GeV/c, $\theta = 90°$)	57	42

Table 1.6: Performance parameters of SVD1 and SVD2.

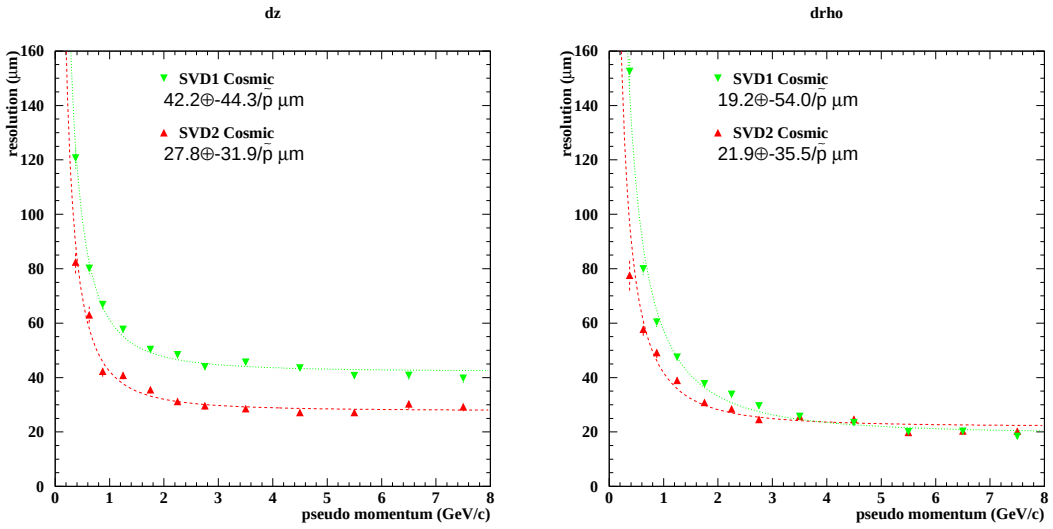

Figure 1.17: Impact parameter resolutions (left) in z and (right) in $r\phi$ coordinates for the SVD1 and SVD2.

1.3 Central Drift Chamber (CDC)

The present CDC has been working well with $10^{34} cm^{-1} sec^{-1}$ luminosity. The momentum resolution is quite good even in rather low momentum region due to filling the Helium-based gas and using aluminum filed wires, as shown in Fig. 1.18. The dE/dx resolution is also reasonably good. The information helps to identify hadrons and electrons.

The total current draw in CDC is shown in Fig. 1.19. As you can see, it has been kept constant even for higher storage beam current from year to year due to improvement of a vacuum condition in the KEKB ring and installation of several masks near the interaction point. A better vacuum system and a better masking system should be applied in Super-KEKB.

The hit rate for the present Belle CDC at the highest beam current is shown in Fig. 1.20., where the hit rate at the inner most layer around 200 kHz. This layer works with a short enough dead time under this condition. The integrated charge on sense wires in the inner most layers for four years operation exceeds 0.2 Coulomb/cm. No significant degradation of the gas gain has been observed. The dark current without the beams is still quit small. The hit rate for most of other layer is less than 10 kHz. If we assume higher beam background by 20 times for Super-KEKB, the hit rate is expected less than 200 kHz, which is similar to that for the inner most layer. From these experiences, it is concluded that the gas chamber works for Super-KEKB.

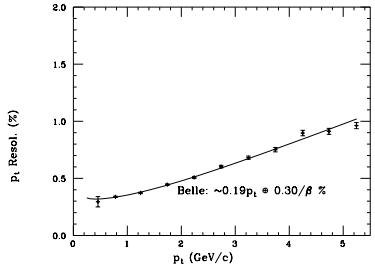

Figure 1.18: The momentum resolution obtained by CDC with SVD.

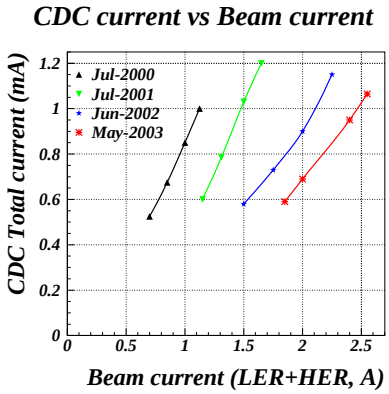

Figure 1.19: The CDC total current draw as a function of the total beam current in KEKB.

In summer of 2003, the cathode part, which corresponds to the inner most three layers was replaced with a new chamber in order to provide a space for SVD2. The new chamber consists of smaller cells about 5 mm× 5 mm due to limited space and reducing the occupancy. The maximum drift time becomes shorter less than 100 nsec under the 1.5 Tesla magnetic field as shown in Fig. 1.21. It is quite promising to reduce the occupancy.

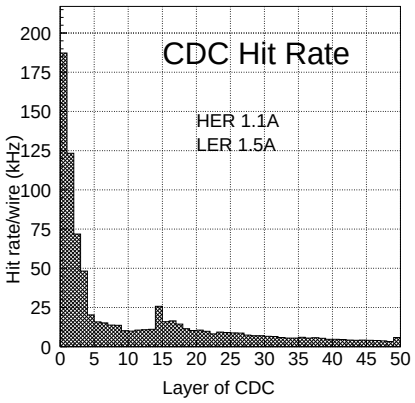

Figure 1.20: The hit rate a wire as a function of the CDC layer.

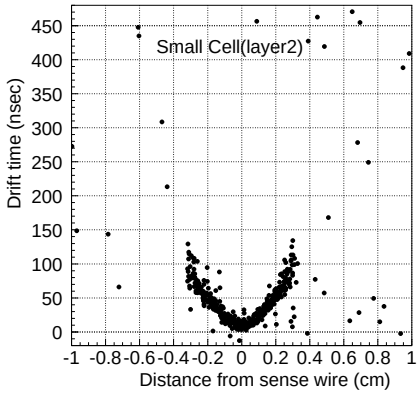

Figure 1.21: The drift time as a function of the distance from the sense wire.

1.4 Particle Identifier

1.4.1 Framework

In the present Belle experiment, identification of charged hadrons (mainly $K^{\pm}/\pi^{\pm}$) is carried out by combining information from three subsystems; the number of photoelectrons ($N_{\mathrm{p.e.}}$) detected in threshold silica aerogel Cherenkov counters (ACC), time-of-flight (t.o.f.) measured in an array of plastic scintillation counters (TOF) and specific ionization energy loss (dE/dx) measured in the central drift chamber (CDC). Figure 1.22 shows a cross sectional view of the three detectors. A detailed description of the detectors can be found elsewhere [3].

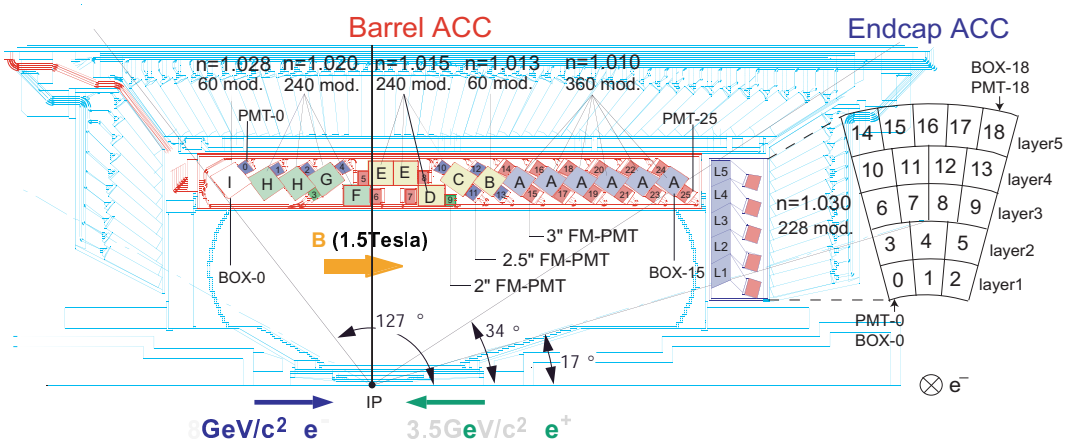

Figure 1.22: Cross-sectional view of the CDC (inner most), ACC and TOF (outer most) detectors.

The ACC system [4] is divided into the barrel and the forward endcap parts. The barrel ACC is composed of 960 counter modules, segmented into 60 cells in the ϕ direction. The endcap ACC is composed of 228 counter modules, arranged in 5 concentric layers. Each counter module is equipped with one or two fine-mesh PMT, whose diameter is either 2, 2.5 or 3 inch. The refractive index (n) of aerogels ranges from 1.010 to 1.028 for the barrel ACC, depending on the polar angular regions, to cover the momentum range from 1.2 to 3.5 GeV/c. For the endcap ACC, $n = 1.030$ has been chosen to serve for the flavor tagging. The detected light yields for light velocity particles ranges from ~ 10 to ~ 26, depending on the type of the ACC module.

The TOF system [5] is segmented into 128 units, where each scintillator bar is 4cm thick, 6cm wide and 255cm long, and equipped with 2-inch fine-mesh PMT at both ends. The measured TOF resolution for minimum ionizing particles is about 100ps, and the system provide more than 3σ K/π separation up to 1.2 GeV/c.

The CDC [6] uses a gas mixture of 50% He and 50% C_2H_6, and has the dE/dx resolution of about 6% for Bhabha electrons. It provides K/π separation up to 0.8 GeV/c and also in the region of relativistic rise (above 2.5 GeV/c).

1.4.2 Present K/π Separation Performance

The information from the three nearly-independent measurements are combined into a single cut variable using a likelihood method. We define a $K^{\pm}$ likelihood ratio $R_K = \mathcal{L}_K/(\mathcal{L}_K + \mathcal{L}_\pi)$, where $\mathcal{L}_K(\pi)$ denotes a product of the three individual likelihoods for the $K^{\pm}(\pi^{\pm})$ mesons. Probability density functions (PDFs) for $N_{\mathrm{p.e.}}$ are obtained from a well-tuned GEANT-based

Monte Carlo simulation, while those for t.o.f. and dE/dx are given in Gaussian forms, each shape deduced from data. Figure 1.23 shows the efficiency (ϵ) and misidentification rate (f) for the $K^{\pm}$ identification, measured with $D^{*+} \to D^0(\to K^-\pi^+)\pi^+$ calibration data, as a function of the track momentum in the laboratory frame (a nominal cut $R_K > 0.6$ is applied). The achieved kaon identification efficiency is about 85% with the misidentification rate lower than 10%, in the momentum region up to 4 GeV/c.

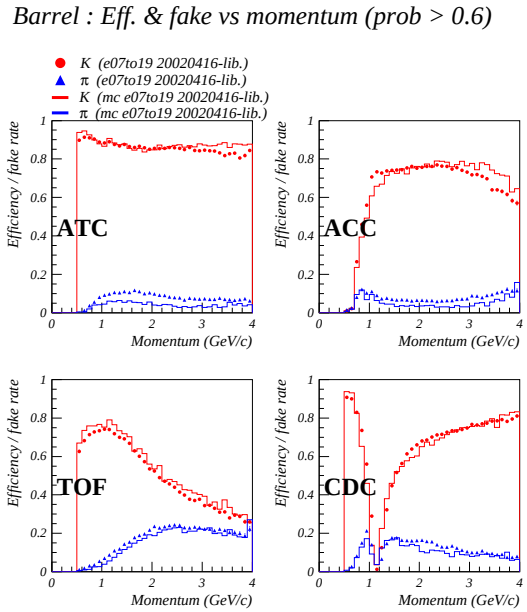

Figure 1.23: Efficiency and misidentification rate for the $K^{\pm}$ (right) identification at the Belle experiment as a function of the track momentum in the laboratory frame.

The inefficiency and misidentification arises from some sources. For example, δ-ray emitted either from the ACC counter box material or the aerogel radiator and also scintillation lights from a diffusive reflector can cause $K^{\pm} \to \pi^{\pm}$ misidentification. The inefficiency arises also from the geometrical gap between the detector modules. There is contribution also from direct particle hits on a PMT glass window, where huge $N_{\text{p.e.}}$ is produced and the identification is no longer possible.

1.4.3 Disadvantages of the Present PID System

The present Belle PID system works effectively for measurements of many B decay channels. However, there are some disadvantages, that motivate the future upgrade, as discussed in detail later.

K/π separation While the present system based on the threshold Cherenkov device has advantage for robust and stable operation, the achieved K/π separation may not be enough for some important channels at the Super-KEKB/Belle experiment. A Cherenkov system based on ring imaging technology, as used in the BaBar experiment, would be a promising approach for improvement. In the BaBar experiment, $K^{\pm}/\pi^{\pm}$ separation is carried out mostly by using the Detector-of-Internally-Reflected-Cherenkov-light (DIRC). The DIRC counter consists of long quartz bars facing to a water-filled expansion region, called the standoff box. Approximately 10,000 photomultiplier tubes are located on the wall of the standoff box to reconstruct a ring

image. Table 1.7 compares the performance for the kaon identification between Belle and BaBar, based on numbers referred from [3] and [7], although they cannot be directly compared.

Table 1.7: Comparison of the $K^{\pm}$ and $\pi^{\pm}$ identification performance at the Belle (upper row) and BaBar (lower row) experiments.

p [GeV/c]	ϵ_K [%]	f_π [%]	ϵ_π [%]	f_K [%]
1.80–2.00	85.4 ± 0.3	10.2 ± 0.3	86.5 ± 0.3	10.5 ± 0.3
1.75–2.00	~ 99	~ 2	—	—
3.00–3.50	83.8 ± 0.3	7.2 ± 0.2	89.5 ± 0.2	11.2 ± 0.2
3.25–3.50	~ 87	~ 11	—	—

Angular coverage for the high momentum PID In the present system, the forward endcap part functions only for the flavor tagging, and it does not provide meaningful K/π separation above 2.0 GeV/c. In this angular region, the track momentum from two-body decays of the B meson reach slightly above 4GeV/c. If based on a threshold device, aerogels with refractive index of about 1.007 was desired to cover the momentum region of interest. However, it was too difficult to develop such a system at the time of construction of the present Belle.

Material thickness Another disadvantage of the present system is an amount of materials, that affect the performance of the electromagnetic calorimeter located outside. The material thickness in radiation length of the present system is about $\sim *\%$ in total, $\sim *\%$ from ACC and $\sim *\%$ from TOF scintillator. The major contribution to the ACC material comes from the fine-mesh PMT's.

1.4.4 Background situation

The background level for the present Belle PID systm was evaluated using the real beam data taken in 2003 and Table 1.8 summarizes the background situation with an assumption of 10 A total current.

detector	hit rate(kHz)	dead time(%)
TOF	170	12
EACC(1st layer)	18	1.3
EACC(5th layer)	6	0.4

Table 1.8: The hit rate estimated assuming total current is 10 A. The dead time shown here is limited by the present readout specifications.

As for the TOF system, the measured PMT single rate is 44 kHz with 20 nsec full width signal in typical runs, where the sum of HER and LER current is about 2.5A. Then, assuming a linear dependence, it is exptrapolated to 170 kHz for 10 A current. This indicates the inefficiency of the TOF counter can go up to 12 % in case that the present MQT and the time stretcher board are applied. Therefore, the present TOF system does not work, unless we develop a detector with finer segmentation or a fast readout with signal processing time of less than 100ns.

As for the ACC system, Figure 1.24 shows the background rate as a function of the EACC layer number, for four different sectors in the ϕ direction. The hit rate is the maximum 2.6 kHz at the innermost layer at r = 500 mm, and decreases to 1.0 kHz at the outermost layer at r = 1030 mm. The hit rate has also a clear ϕ dependence, as shown in the figure, and is the lowest in the sector #10, located at the bottom part of the detector. This can be understood because there is massive material in front of the bottom part of the EACC, which is the supporting system of the QCS magnets.

The current dependence of the hit rate for each layer is plotted in figure 1.24, where the horizontal axis stands for a sum of LER and HER currents. Assuming a linear dependence again, one can extrapolate into 18 kHz for 10 A and 39 kHz for 20 A for the innermost layer. Note that hit rate for the barrel ACC, located just inside of the TOF counter, is almost similar to that observed at the outermost EACC layer, which is evaluated to be 6 kHz for 10 A. The intrinsic dead time for high current enviroment with the present MQT readout system can be estimated to be 1.3 % dead time for 10 A.

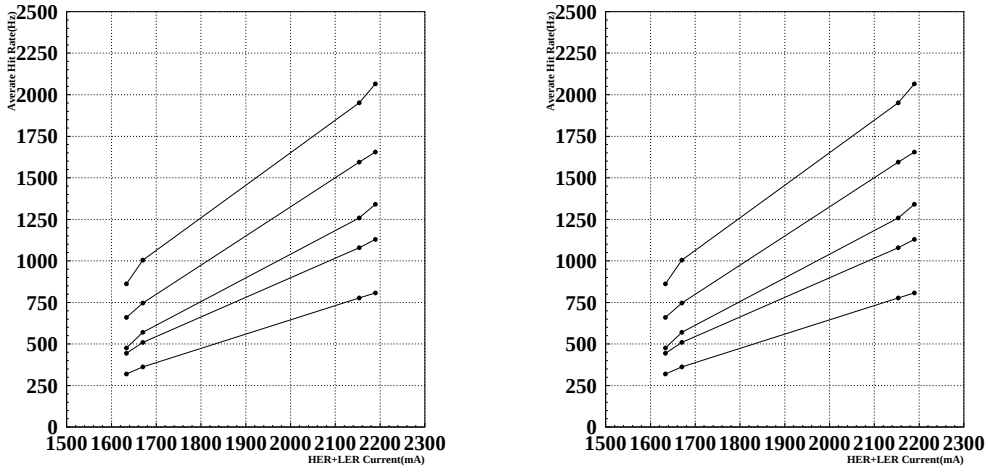

Figure 1.24: Layer dependence of the EACC hit rates for 4 sectors in a typical run (left), and EACC hit rates as a function of a sum of HER and LER currents (right).

1.5 Electromagbetic calorimeter ECL

1.5.1 Performace

The BELLE calorimeter includes barrel part and two endcaps covering solid angle of 91% of 4π. The calorimeter consists of 8736 CsI(Tl) crystals (Fig. 1.25), each having tower shape with about 6 cm $\times$ 6 cm cross section and 30 cm length (16.2 radiation lengths). Total weight of the CsI(Tl) is about 43 tons.

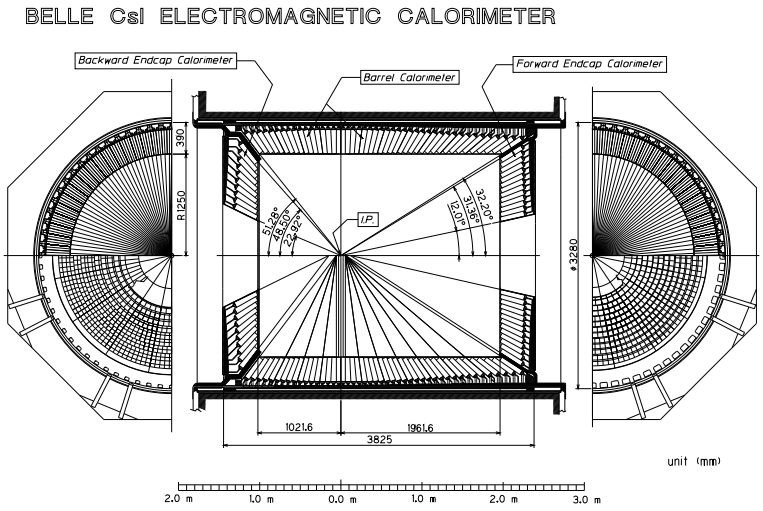

Figure 1.25: *Overall configuration of ECL.*

The counter design is shown in Fig. 1.26. Each crystal is wrapped by one layer of white

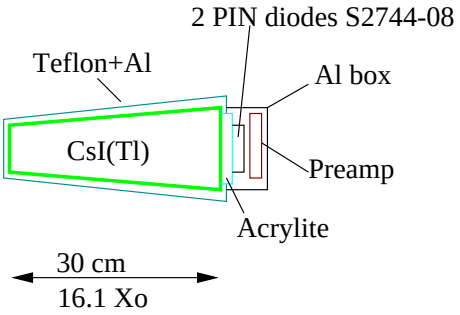

Figure 1.26: *Counter layout.*

200μm thick Gore-Tex film reflector and put in 50 μm thick aluminized mylar envelope. The light of each crystal is detected by two PIN photodiodes (Hamamatsu S2744-08) of 2cm^2 which are glued to the large end face of the crystal. Each photodiode is coupled with a preamplifier mounted on the crystal. The lightoutput corresponds to about 5000 photoelectrons per MeV.

The electronics scheme is presented in Fig. 1.27. The preamplifier signals come to the shaper boards located in the crates around detector. The shaper board contains $CR-(RC)^4$ shaping circuit with $\tau = 1$ μs and MQT300 chip. The latter converts the signal magnitude to three time intervals which are measured by multi-hit TDC 1877S. This circuit provides measurement in three ranges: $\sim$ 0.06 MeV/bin, $\sim$ 0.5 MeV/bin and $\sim$ 4 MeV/bin , where bin is one TDC

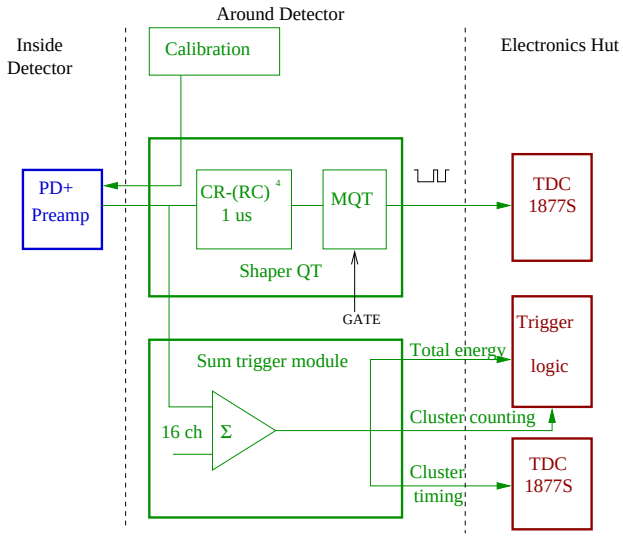

Figure 1.27: *Electronics channel.*

count. Sparsification allows readout only channels with energy deposition exceeding certain threshold(0.5 MeV). The energy noise equivalent is about 200 keV per channel.

The shaper board is also equipped with the fast shaping curcuit with $\tau = 200$ ns. The signal from this curcuit is used for trigger and providing the event timing.

The calorimeter was assembled in autumn of 1998 and it has been under operation since June 1999. All counters are alive and show designed performance. The intrinsic electronics noise corresponds to the expected value of 200 keV/channel. However, during the high luminosity run the beam background causes pileup which increases the total noise level. The pileup noise is about 200 $\sim$ 400 keV in barrel and 600 $\sim$ 1200 keV in endcaps for the luminosity of 10^{34} cm^{-2}s^{-1}.

Each counter is calibrated by Bhabha and $e^+e^- \to \gamma\gamma$ reactions, i.e. calibrated at the highest energy point. To estimate the nonlinearity of the energy reconstruction the processes $\pi^0 \to \gamma\gamma$ and $e^+e^- \to e^+e^-\gamma$ are used. The measured nonlinearity for the photons amounts about 2% at 100 MeV. This effect has been monitored and an appropriate correction is applied for physics analysis.

The fig. 1.28 shows the distribution of reconstructed photon energies normalized to calculated from angles values for $e^+e^- \to \gamma\gamma$ events with two clusters. The obtained energy resolution for barrel and forward endcap is about 1.7%, for backward endcap — 2.9%. These value are in good agreement with Monte Carlo predictions. Worse energy resolution in backward endcap is due to the passive material in front of calorimeter which is about 0.8 X_0 and 0.4 X_0 in endcaps and in barrel respectively. In backward region where the photons energy is lower the effect of passive material is larger.

The distribution of two photon invariant mass(fig. 1.29) shows clear peaks of π^0 and η with mass resolution of 4.8MeV/c^2 and 12MeV/c^2 respectively. The comparison of the calorimeter performance and Monte Carlo prediction are demonstrated in the fig. 1.30. The π^0 mass peak resolution is shown in dependence on photon energy for the symmetrical case of pion decay($E_1 \approx E_2$). As one can see the data are in good agreement with MC for the photon energies higher of 300 MeV. For lower energies the mass width for data about 10% large. One of the possible explanation is that the pileup noise is not fully taken into account in MC.

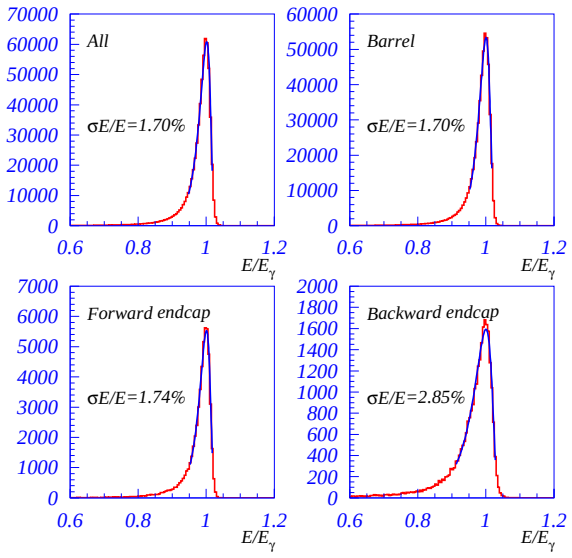

Figure 1.28: *Reconstructed energy distribution for* $e^+e^- \to \gamma\gamma$.

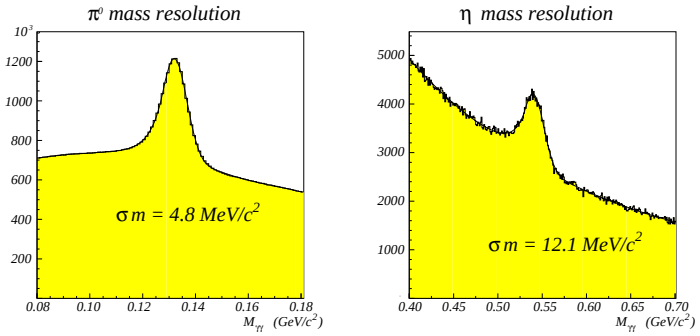

Figure 1.29: *Two photon invariant mass distribution.*

1.5.2 Effect of Background

High background conditions create some issues to be overcome in terms of detector operation. For an electromagnetic calorimeter case, we have to deal with several problems such as radiation damage of the crystals, pileup noise of the counters and fake photons.

The radiation damage causes a decrease of the light output of the calorimeter crystals which results in the degradation of the energy resolution. In the Belle detector the accumulated radiation dose is monitored by measuring the average photodiode (PD) currents in different parts of the calorimeter. During four year operation the accumulated dose is about 20 Rad for the barrel and about 100 Rad for endcaps. The light output degradation caused by the dose is shown in Fig. 1.31 and is in agreement with the radiation hardness measurement before installation(Fig. 1.32). Assuming a 20 times higher radiation dose we can expect the light output degradation about 10% for the barrel and about 25% for the endcaps that is not critical for the calorimeter performance.

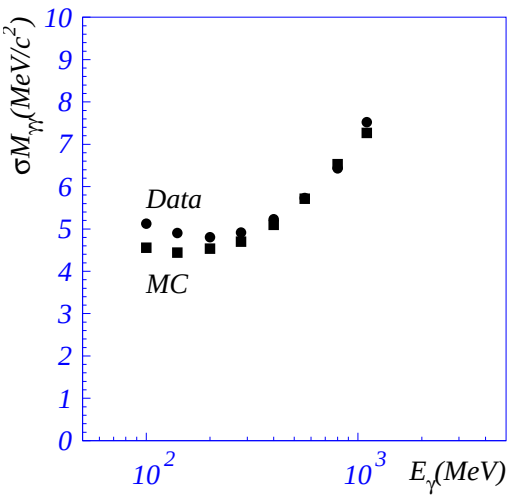

Figure 1.30: π^0 *mass resolution for symmetric case* $E_{\gamma 1} \approx E_{\gamma 2}$.

Another effect of the radiation is an increase of the silicon PIN diode dark current. The time dependence of the dark current for the Belle detector is shown in Fig. 1.33. For the barrel calorimeter the increase of the dark current is about of 20% while for the forward endcaps the dark current has already increased a factor of ten. A possible explanation of this phenomena is the effect of a neutron radiation dose. The effect of the dark current increase limits usage of the PIN diodes in the endcaps for the upgraded detector.

The main origin of the beam background is from the lost beam particles interacting in a support structure around the detector. The interaction of initial particles produces an electron-photon showers. Photons produced in such showers penetrate inside the detector and can make hits. The spectrum of the shower photons is peaked at low energies but some part of the photons can have energies of tens and hundreds MeV. Background photons with high energy are reconstructed as real photons while the large number of low energy photons randomly overlapping with real signals produce an effective pileup noise.

The spectrum of the background photons was obtained by a random triggered event sample. The energy and angular distribution of such events is shown in Figs. 1.34, 1.35. For the luminosity of $5 \times 10^{33}\, s^{-1} cm^{-2}$ the average number of the background photons with energy more than 20 MeV is 3 per events: one fake photon comes to the barrel and the other two come to the endcaps.

Low energy background photons overlapping with a real signal induce smearing effect. The pileup noise as well as the electronic noise contribute to the energy resolution. These effect can be expressed as: $\approx \sigma_{\rm noise}\sqrt{n_{\rm crystals}}/E$, where $\sigma_{\rm noise}$ is the noise level of each counter to which pileup and electronics contribute, $n_{\rm crystals}$ is number of crystals included in a cluster which has the energy E. When E is a few hundred MeV, $n_{\rm crystals}$ is typically from 6 to 9.

The value of the noise level ($\sigma_{\rm noise}$) has been measured by the pedestal width. The average pedestal width as a function of the polar angle (θ) is shown in Fig 1.36. After subtraction of the electronic noise, which is equivalent to 200 KeV, we find the contribution of the pileup noise. Neglecting the beam-beam interaction effects, we can present the pileup noise of $\sigma(\theta)$ as

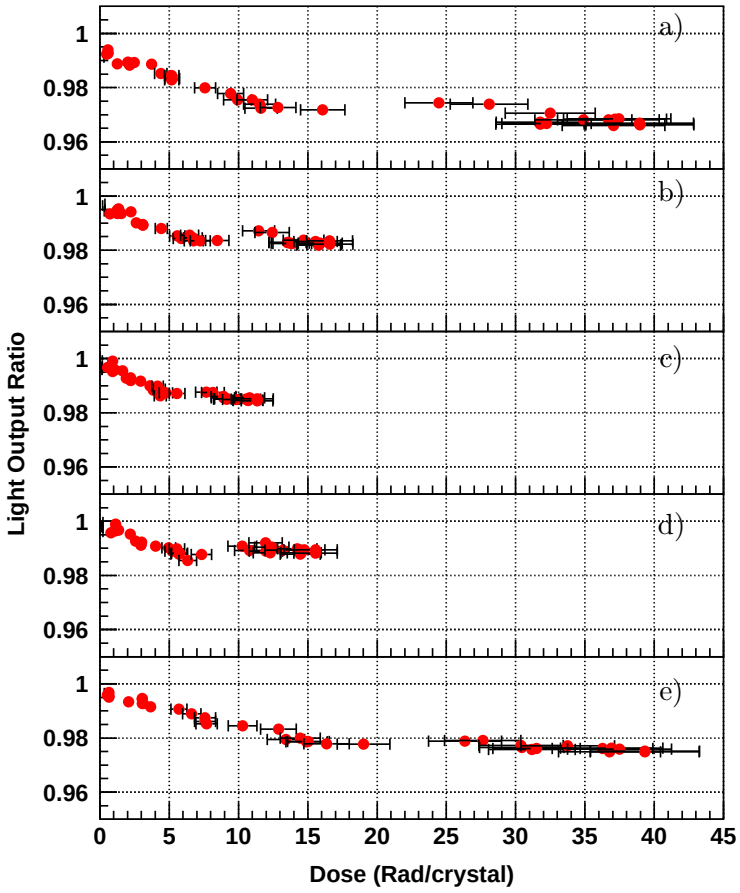

Figure 1.31: Dependence of the light output degradation on a dose. Five figures correspond to different calorimeter parts: a) innermost forward calorimeter; b) outer forward calorimeter; c) barrel; d) outer backward calorimeter; e) innermost backward calorimeter.

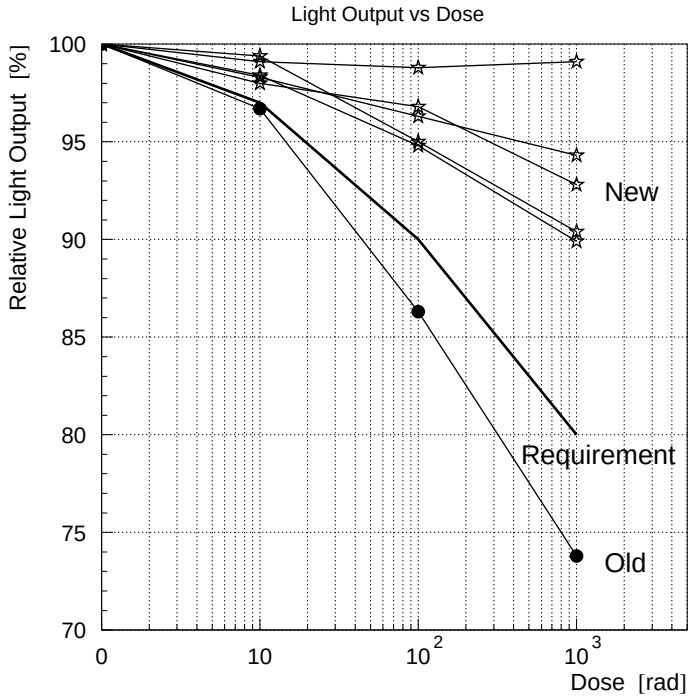

Figure 1.32: Light Output degradation measured with test crystals([35]) "OLD" corresponds to crystals at very early production stage and "NEW" corresponds to crystals produced by the improved method for mass production. .

a contribution of two components coming from LER and HER:

$$\sigma(\theta) = \sqrt{(\alpha_{LER}\sigma_{LER}(\theta))^2 + (\alpha_{HER}\sigma_{HER}(\theta))^2}, \tag{1.5}$$

where $\sigma_{\rm LER}$ and $\sigma_{\rm HER}$ give θ dependence of each beam. The pileup noise depending on beam currents and vacuum pressure are denoted by $\alpha_{\rm LER}$ and $\alpha_{\rm HER}$. $\sigma_{\rm LER}$ and $\sigma_{\rm HER}$ are measured with a single beam data as shown in Fig. 1.37. The measurements of the pileup noise at various beam currents are in good agreement with the simple parameterization (1.5).

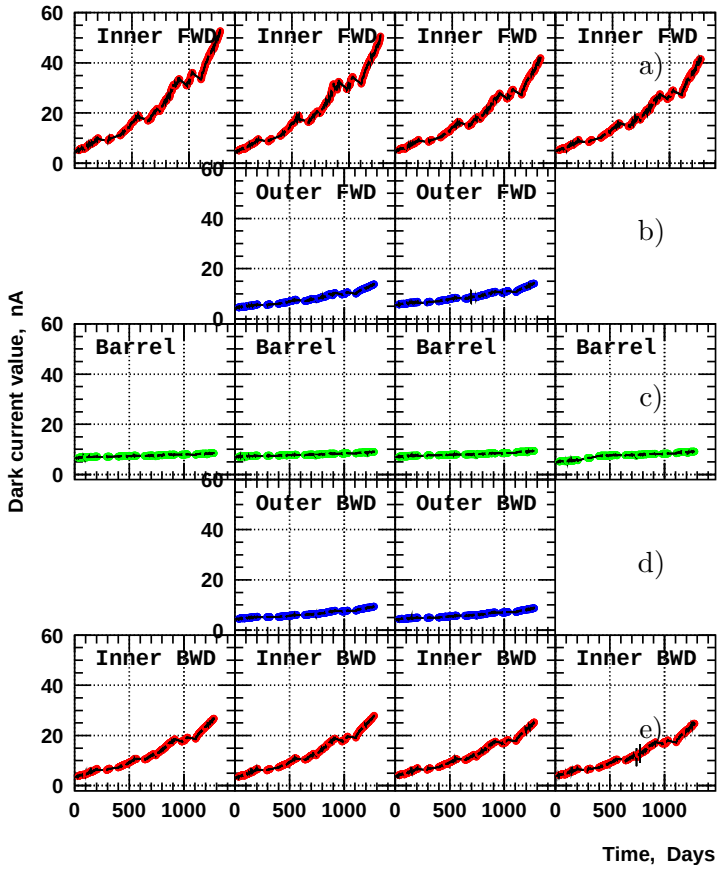

Figure 1.33: The PIN diodes dark current dependence on time. a) innermost forward calorimeter; b) outer forward calorimeter; c) barrel; d) outer backward calorimeter; e) innermost backward calorimeter.

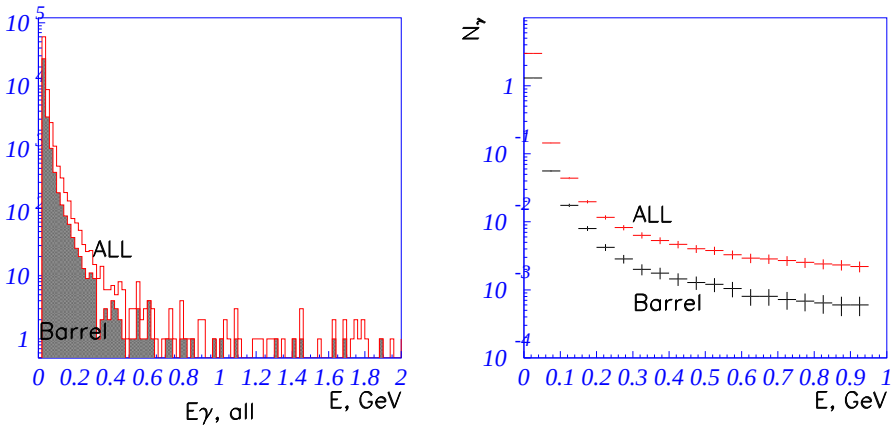

Figure 1.34: a) Energy distribution of background clusters. b) The number of background clusters with energy more than E per event.

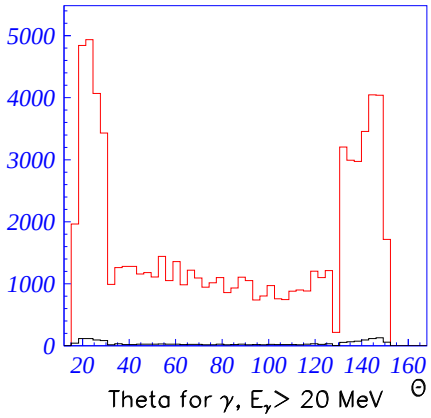

Figure 1.35: Angular distribution of the background clusters.

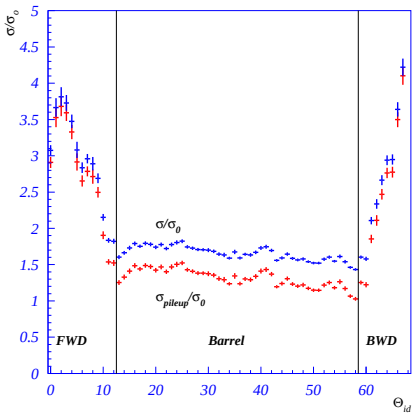

Figure 1.36: Dependence of a pedestal width on the theta-number of the crystal ring (θ_{id}). The pedestal width is normalized to the electronic noise $\sigma_0 = 200\,keV$. The measurements were carried out for $I_{HER} \approx I_{LER} \approx 360mA$.

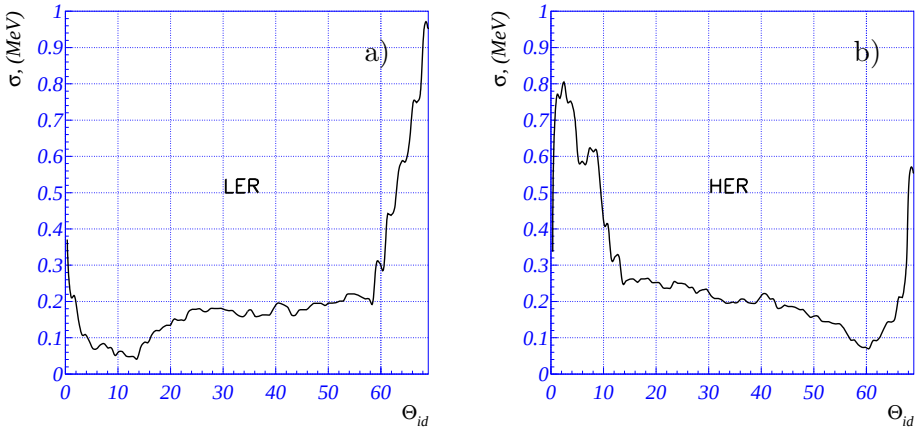

Figure 1.37: Theta dependence of the pileup noise contribution from the a) LER and b)HER beam.

1.6 KLM

The Belle K_L and muon detector (KLM) consists of an alternating sandwich of 4.7-cm thick iron plates and resistive plate counters (RPCs) [3, 9] located outside the superconducting solenoid. The iron plates serve a dual role as the flux return for the solenoidal magnetic field. One iron-RPC superlayer octant (quadrant) of the barrel (endcap) is shown in Fig. 1.38. The RPCs, whose cross section is illustrated in Fig. 1.39, use 2-mm thick soda-lime glass for the electrodes, with a bulk resistivity on the order of $10^{12}\,\Omega\cdot$cm.

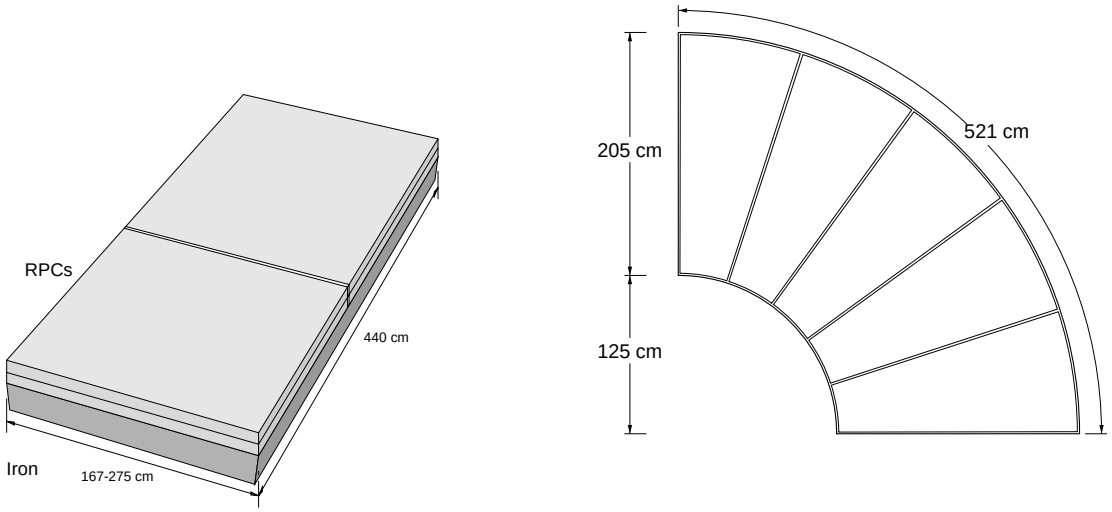

Figure 1.38: *One iron-RPC layer octant in the KLM barrel (left), and one quadrant in the KLM endcap (right). The barrel octant consists of four single-gap RPCs arranged in two layers; the endcap quadrant consists of ten single-gap RPCs arranged in two layers.*

The operating gas is a mixture of argon, butane and HFC134a (freon) in the proportions 30 : 8 : 62 by volume, flowing at a rate of 4 (8) cc/min/layer in the barrel (endcap). The $\sim 4\,$kV/mm electric field in the gas gap produces a streamer from one electrode to the other upon the passage of an ionizing particle. The discharge is naturally quenched by the high resistivity of the glass; the $\sim 2\,\text{mm}^2$ spot in the vicinity of this discharge remains dead until the glass surfaces slowly recharge. A streamer in either RPC gas gap is imaged on both planes of the exterior orthogonal copper readout strips. The signals from these 38000 strips are digitized and then serialized into a time-slice stream (12 strips per stream, $1\,\mu$s window) that is fed into a LeCroy multihit TDC. The time information for each hit is retained and is used in the analysis software to impose an in-time window of 50 ns relative to the trigger time.

The RPC performance is quite sensitive to the background hit rate, due to the long recovery time of a discharged spot on the glass electrode. The efficiency is shown as a function of the ambient rate in Fig. 1.40 and as a function of calendar time in Fig. 1.41. No aging effects are visible in either the barrel or the endcap. (One sensitive measure of aging is the performance during cosmic ray runs interspersed within each run cycle.)

The barrel RPCs exhibit an efficiency drop with ambient rate of $-0.05/(\text{Hz/cm}^2)$, and are presently operating at a rate of $\simeq 0.05\,\text{Hz/cm}^2$, dominated by cosmic rays and random discharges. The dependence of the noise rate on LER current, HER current, and luminosity is quite mild except in the innermost layer (see Fig. 1.42, where extrapolations to the conditions

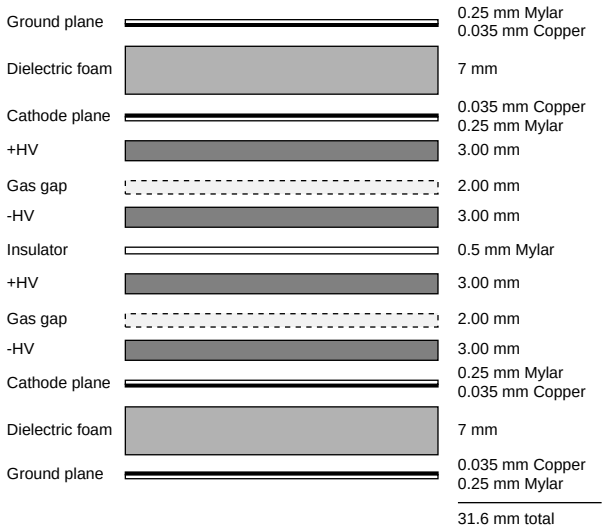

Figure 1.39: *Exploded side view of one RPC superlayer.*

of SuperKEKB lead to a noise rate of 0.7 (or 2.5) $\mathrm{Hz/cm^2}$ at a luminosity of 1.0 (or 5.0) $\times$ $10^{35}\,\mathrm{cm^{-2}s^{-1}}$, corresponding to an efficiency of 96% (or 87%). This projected noise rate in the innermost layer is 20 times greater than seen now. All other barrel layers are projected to have efficiencies above 93%, even at the higher luminosity. Thus, there is no need to replace the barrel RPCs for SuperKEKB.

The endcap RPCs, on the other hand, show an efficiency drop with ambient rate of roughly $-0.3/(\mathrm{Hz/cm^2})$—an order of magnitude more sensitive to background than the barrel RPCs—and exhibit substantially more scatter around the average trend. It is not clear if these effects are due to a difference in material/construction or a distinction in the nature of the ambient background and the RPC response thereto. The background is highest in the outermost layers due to inadequate shielding, and is attenuated with depth into the RPC/iron stack at a rate that is consistent with soft neutrons but entirely inconsistent with photons. (See Fig. 1.43.) In single beam runs, these neutrons are presumed to arise arise from spent electrons or positrons striking the beam pipe far upstream or downstream of the interaction point. In luminosity runs, additional neutrons are generated
from very-small-angle Bhabha scattering that deflects the electron and/or positron into the beam pipe far upstream or downstream of the interaction point. Compared to the innermost barrel layer, the outermost endcap layer's noise rate is at least five times more sensitive to the LER current, HER current, and luminosity. (See Fig. 1.44.) To the extent that a linear extrapolation is valid, the predicted rates in all endcap layers are between 0.5 and 3.0 (or between 2.0 and 13) $\mathrm{Hz/cm^2}$ at projected luminosities of 1.0 (or 5.0) $\times 10^{35}\,\mathrm{cm^{-2}s^{-1}}$, corresponding to efficiencies between 86% and 30% (or between 50% and 0). These projected rates are more than 30 times the present background rate; if layers 12 and 13 were to be turned on again in SuperKEKB, they would suffer a background rate that is 40 times greater than seen now in layer 11. Absent any improvement in shielding of neutrons or the RPCs' sensitivity to them, the endcap RPCs are an unlikely candidate for muon and K_L detection in the SuperKEKB era.

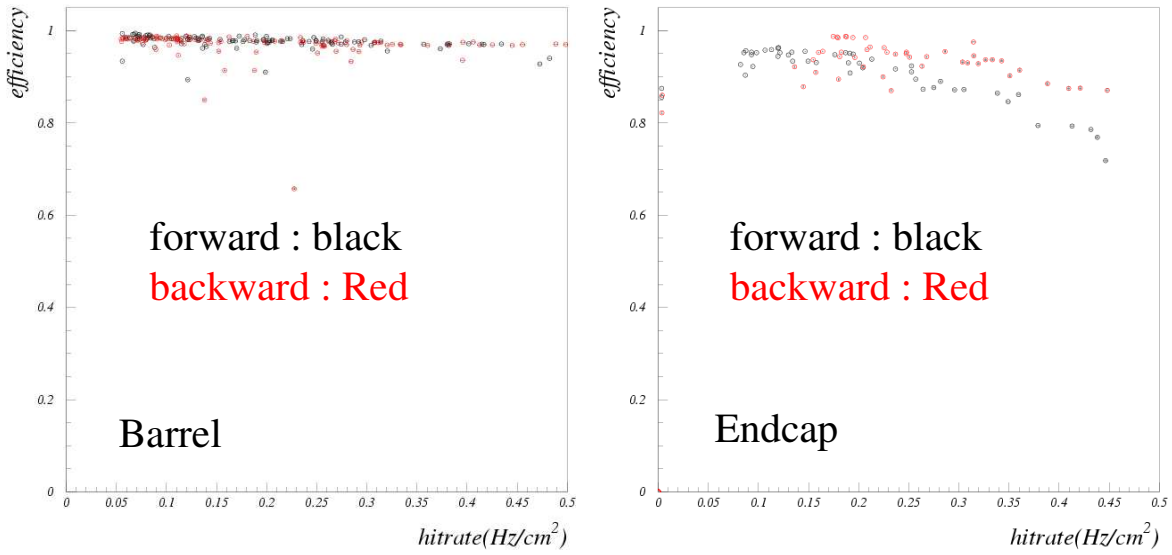

Figure 1.40: *Dependence of RPC superlayer efficiency on ambient hit rate.*

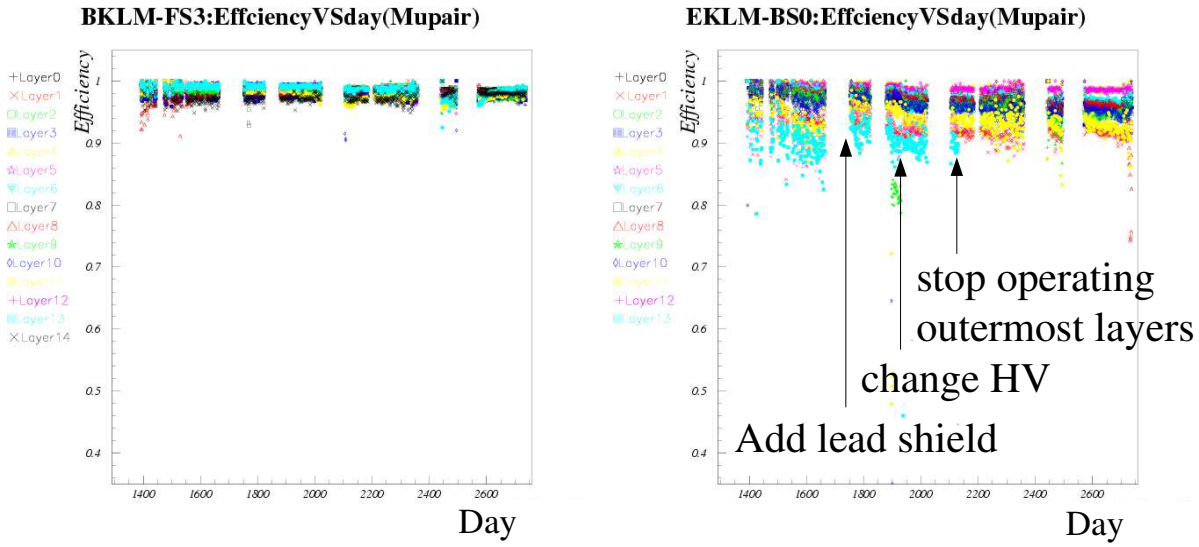

Figure 1.41: *Dependence of RPC superlayer efficiency on time for all superlayers in Forward Barrel Octant 3 (left) and Backward Endcap Quadrant 0 (right). Day 1300 corresponds to October 1999, while Day 2750 corresponds to July 2003.*

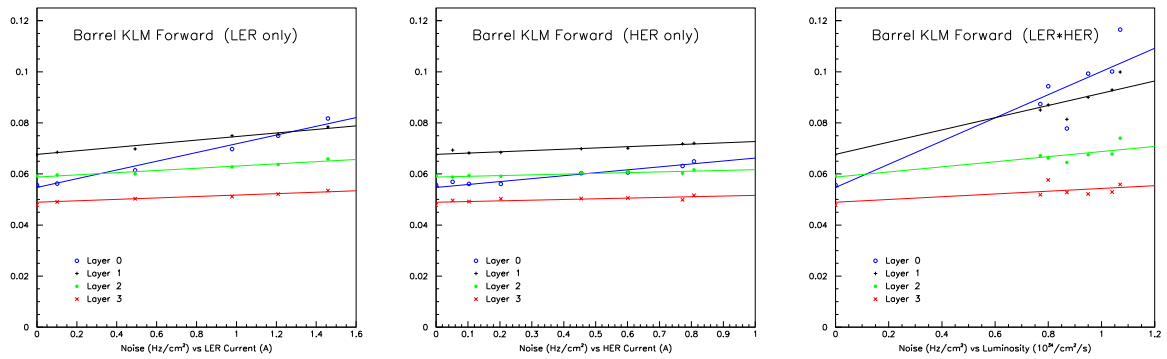

Figure 1.42: *Dependence of the noise rate in barrel layers 0–3 as a function of LER current, HER current, and luminosity.*

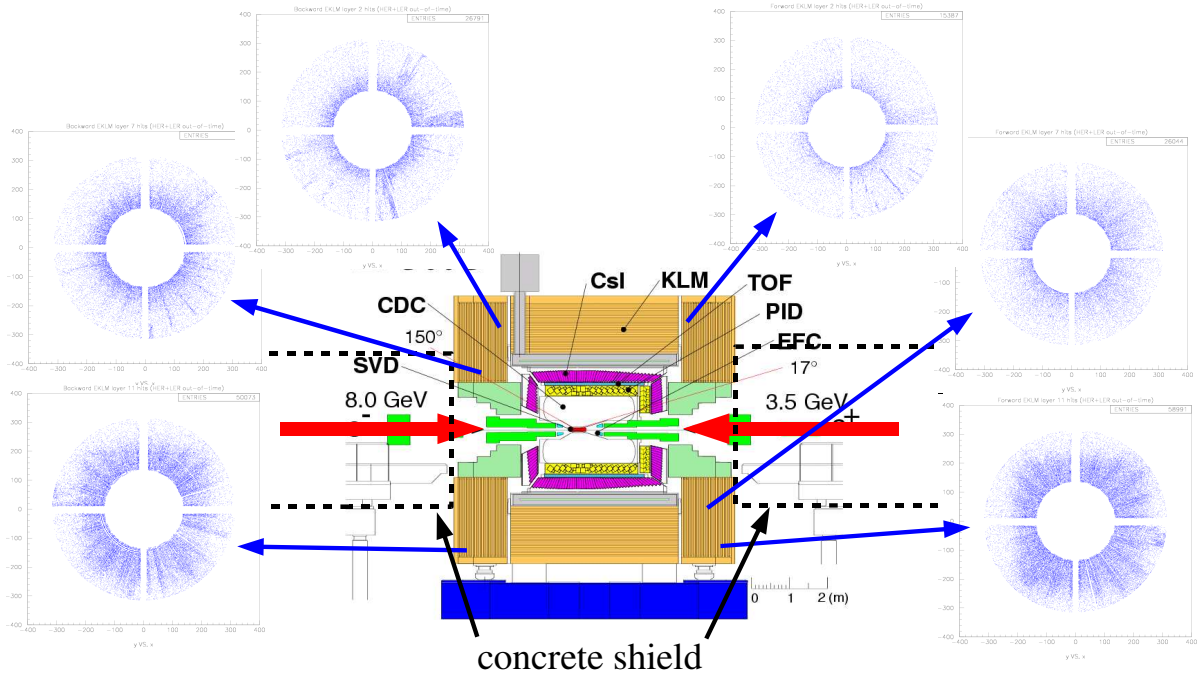

Figure 1.43: *Background hits in three typical superlayers of the backward (left) and forward (right) endcap KLM with* $I_{e^+} = 1.5\,\mathrm{A}$ *and* $I_{e^-} = 1.0\,\mathrm{A}$. *The hits in the outermost layers clearly delineate the concrete shield that surrounds the beam lines, within which the exposure to neutrons is highest.*

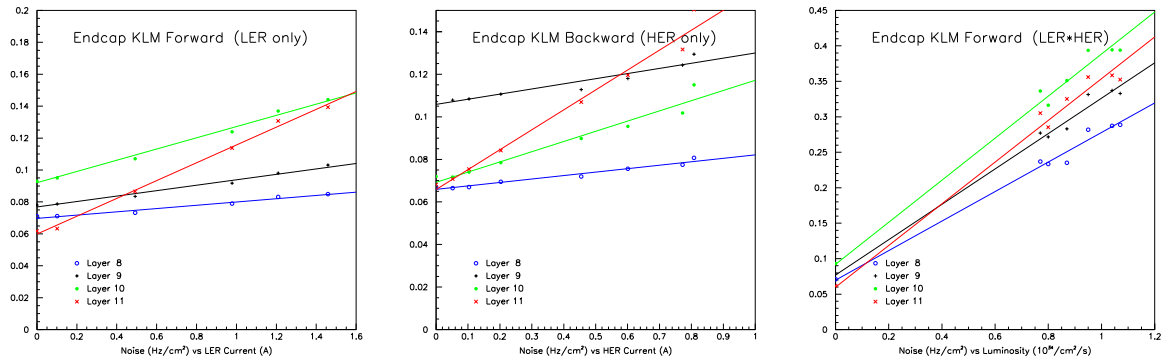

Figure 1.44: *Dependence of the noise rate in endcap layers 0–3 as a function of LER current, HER current, and luminosity.*

1.7 Trigger and DAQ system

1.7.1 Trigger

The trigger signal is generated using a combination of fast signals from several detectors. Fig. 1.45 shows the block diagram of the trigger system. The average trigger rate of the present

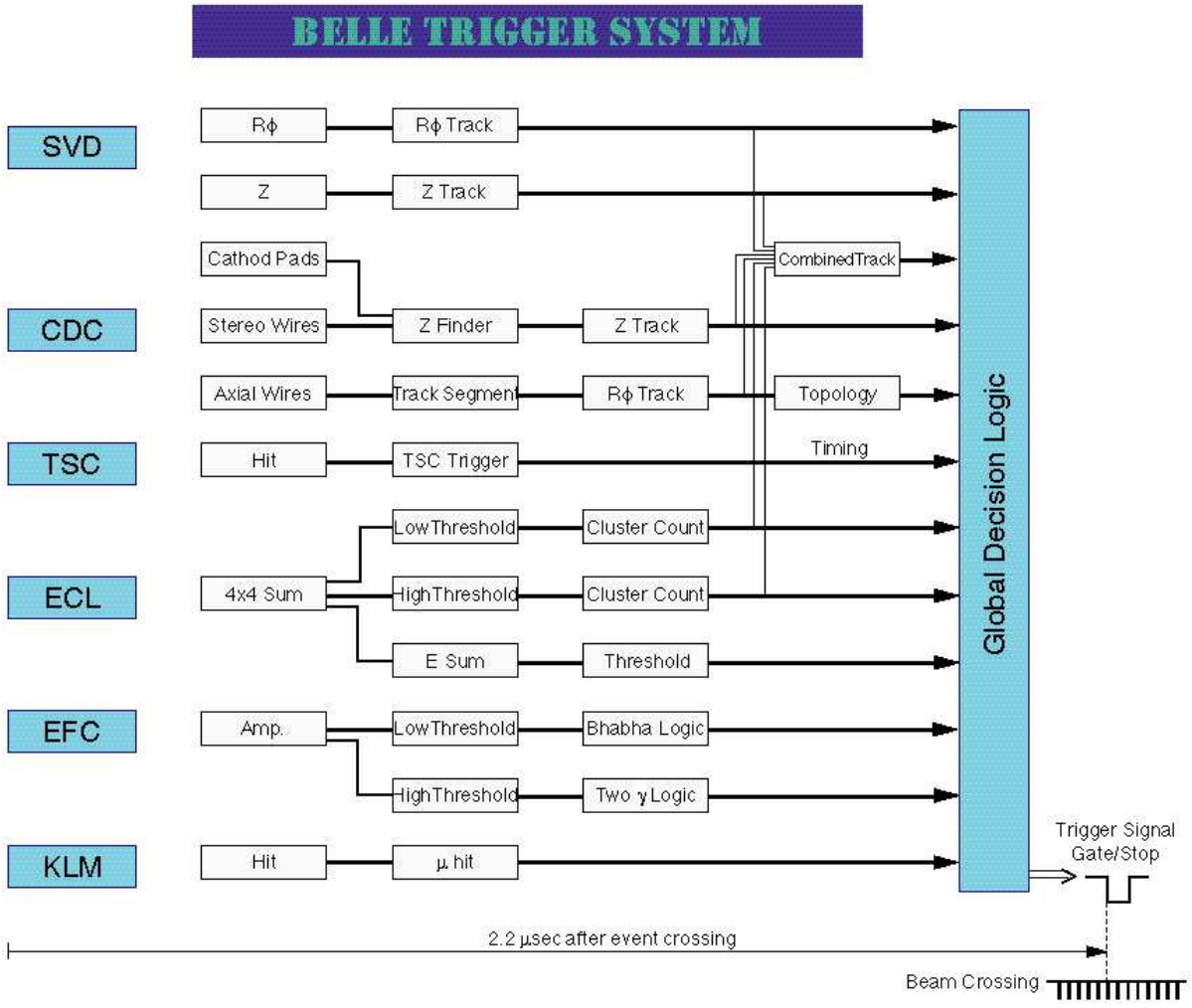

Figure 1.45: Belle Trigger System

Belle trigger system is plotted in Fig. 1.46 as a function of the average luminosity (a) and as a function of the average beam current (b). Each point corresponds to one run. Globally there is a linear correlation in both plots. The variation of the trigger rate is due to the KEKB condition. The most sensitive parameters of the KEKB accelerator to the trigger rate are the HER current and the vacuum of HER. In a good condition, the average trigger rate is about 400Hz at the luminosity of $10^{34}\ cm^{-2}s^{-}1$. This rate is well under the present DAQ limit. The trigger efficiency for hadronic events are measured in offline using redundant trigger sub-systems(the charged track trigger, the energy sum trigger, and the isolated cluster counting trigger). It is measured to be more than 99%, which is satisfactory higher than the requirements from physics analyses.

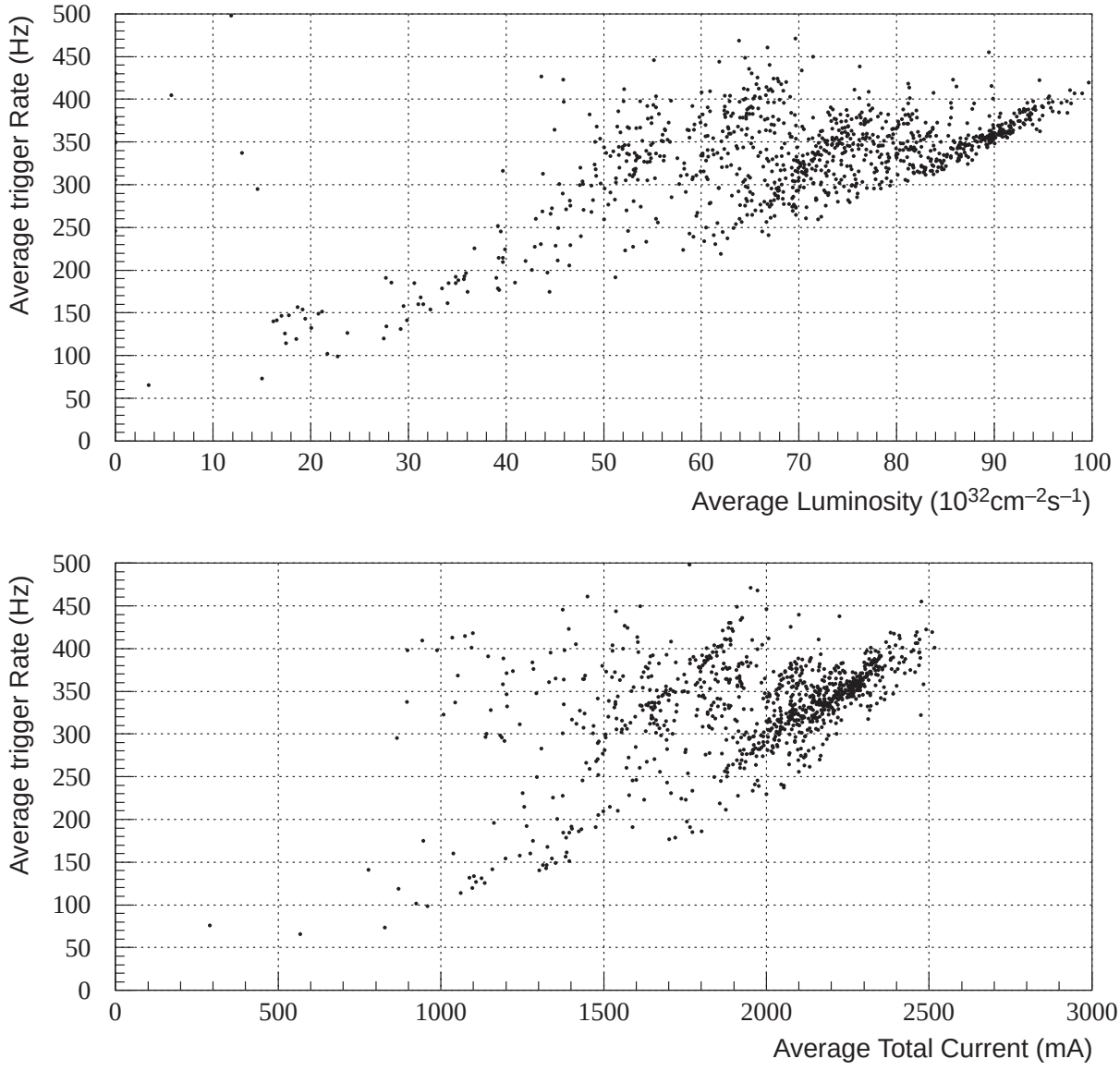

Figure 1.46: The average trigger rate versus the average luminosity (a) or the total currents (b) . Each point corresponding to one run, taken in autumn 2003.

1.7.2 Data Acquisition System

Fig. 1.47 shows the schematic view of the Belle data acquisition system. The signal from detectors except SVD are digitized by a unified readout system based on the Q-to-T conversion with FASTBUS TDCs. Digitized signals are sent to a VME crate by an intelligent FASTBUS controller and transfered to the event building farm through a 100base-TX network. The data from SVD are processed by a PC-based readout system and sent to the event building farm directly via the network. Event building farm consists of three layers of PC servers. The first layer servers receive the data from VME readout systems and perform a partial event building for connected subdetectors. The software trigger processing using the partially-built event is also done (Level 2.5 trigger) and the veto signal is sent to the second layer servers to reject the event data from other layer 1 servers. The final event building is done on the layer 3 server and the event is sent to the storage system.

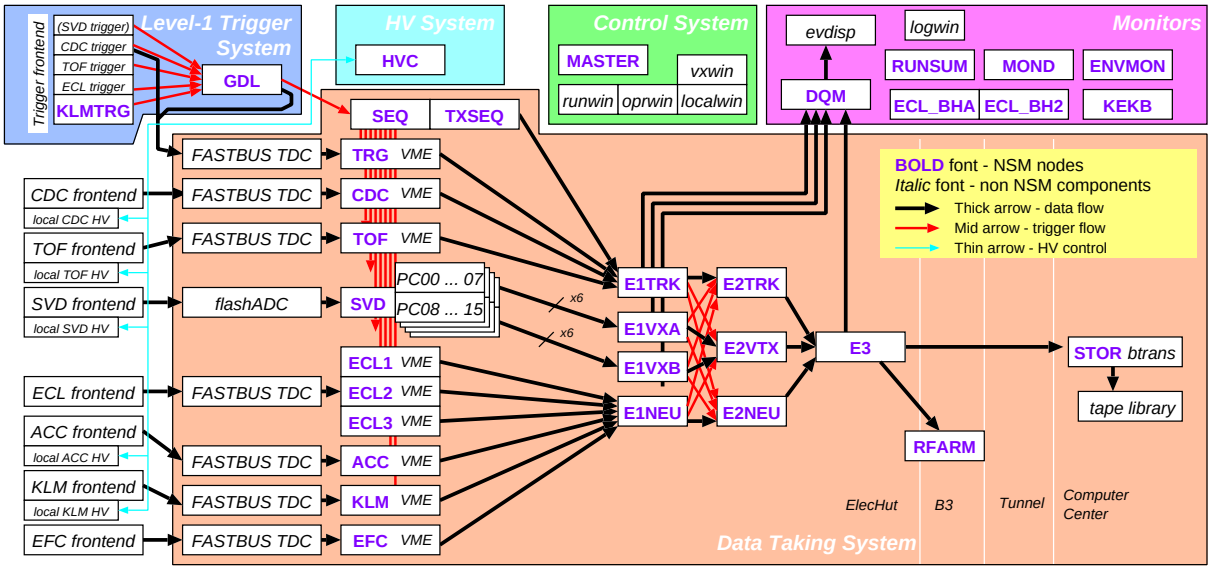

Figure 1.47: Global design of data acquisition system

The current readout system is not a pipelined system and therefore it has a readout dead time. Fig. 1.48 shows the distributions of readout time for some of detectors during when the data cannot be recorded. The readout time for SVD is almost fixed at 30 μsec. The time for other detectors consists of two components. One is the constant latency caused by the readout overhead which is around 30 μsec. The other is the component which is proportional to the data size and makes the tail component in the distribution. The total dead time fraction meaasured as a function of the trigger rate is shown in Fig. 1.49. As seen, the dead time fraction increases almost linear to the trigger rate. At a typical operating trigger rate of 400Hz, the fraction is around 2%.

If the same readout system is used in the environment at SuperKEKB where the trigger rate is expected to be more than 10KHz, a linear extrapolation of the dead time fraction gives more than 50% and the system is totally unusable. Therefore a development of a new data acquisition system based on the pipeline readout technology is necessary.

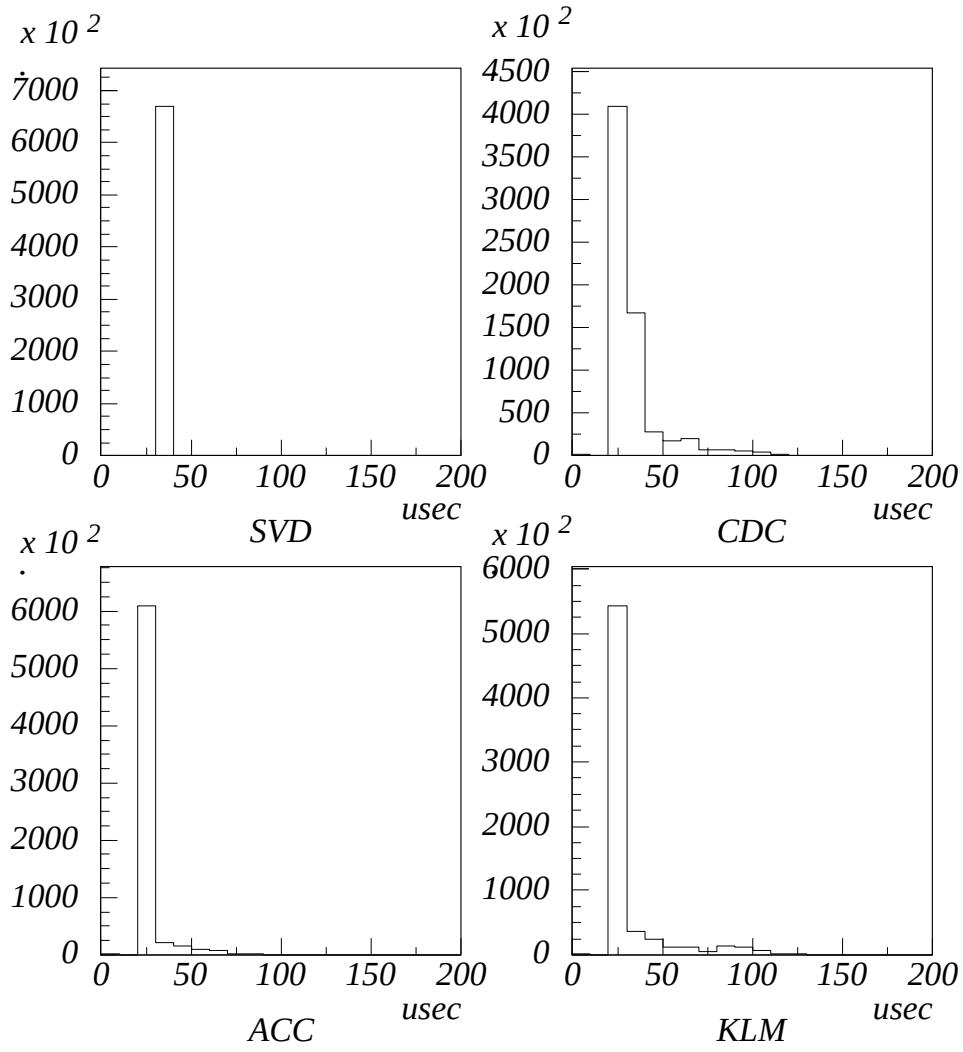

Figure 1.48: The distributions of the readout time for SVD, CDC, ECL, and KLM.

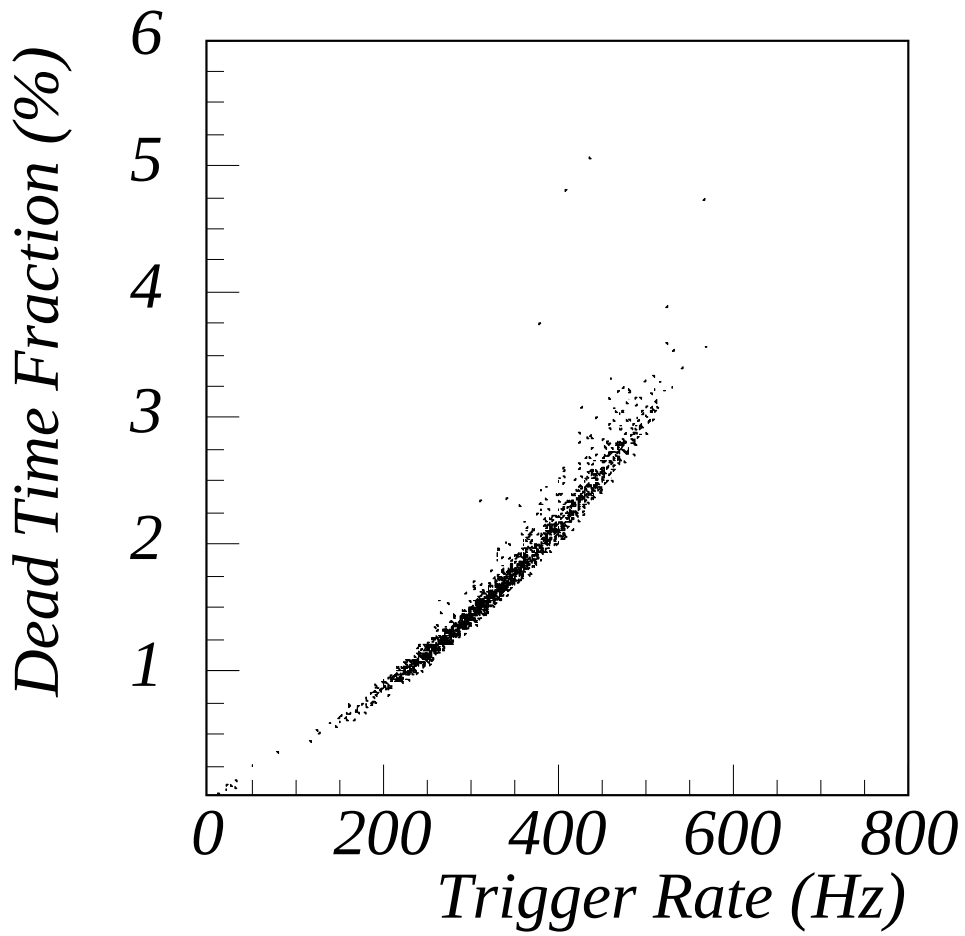

Figure 1.49: The dead time fraction as a function of the trigger rate.

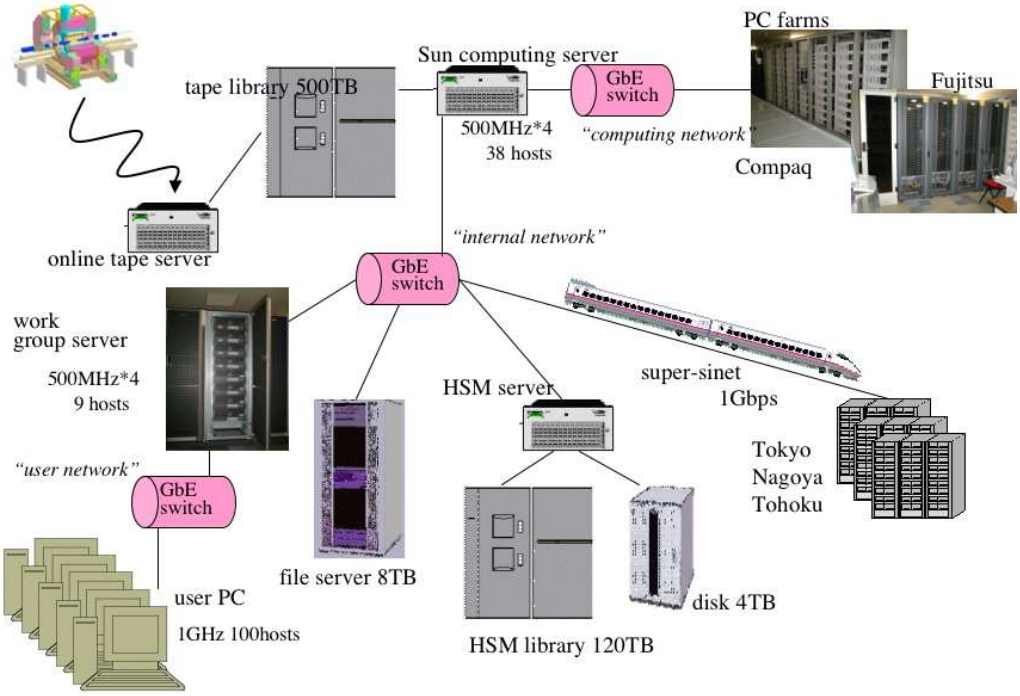

Figure 1.50: Belle computing system.

1.8 Computing System

Here we will briefly sketch the current Belle computing system and details can be found in [54].

1.8.1 KEK B-computing system

The second generation KEK B-computing system has been in operation since Feb. 2001. Figure 1.50 shows a schematic view of this system, which consists of Ultra SPARC compute servers, Ultra SPARC work group servers, user PC's, PC farms and three independent networks connecting them. The first network connects Ultra SPARC servers and the PC farms. The 38 servers are operated under the LSF batch queuing system. Of the 38 servers, twenty servers are equipped with 2 SONY DTF2 tape drives each which are mounted in a robotic tape library system of 500TB capacity. The PC farms are used for the DST/MC productions.

The second network is for user analyses connecting work group servers, the compute servers and data storage systems. Nine Ultra SPARC work group servers are mainly used interactively. The hierarchical mass storage system (120 TB capacity) with 4 TB staging disks in addition to 8 TB file servers contain all Belle data for user physics analyses. The third network links between the work group servers and 100+ user PC's. Everybody can use her/his own PC for analysis, or use to login onto one of the work group servers and analyze data interactively. Users can submit batch jobs to the compute servers from the work group servers.

The computing resources are summarized in Table 1.9.

1.8.2 Data flow

Raw data from the Belle detector are sent to an online Ultra SPARC server and written to DTF2 tapes (raw data tapes). The DST production is proceeded in the following way. One

host	processor	clock	#CPU's	#nodes
computing server	SPARC	500MHz	4	38
work group server	SPARC	500MHz	4	9
user PC	P3	1GHz	1	100

Table 1.9: A summary of computing resources for the Belle computing system.

vendor	processor	clock	#CPU's	#nodes	total CPU
Dell	P3	500MHz	4	16	32GHz
Dell	P3	550MHz	4	20	44GHz
Compaq	P3	800MHz	2	20	32GHz
Compaq	P3	933MHz	2	20	37GHz
Compaq	Intel Xeon	700MHz	4	60	168GHz
Fujitsu	P3	1.26GHz	2	127	320GHz
Compaq	P3	700MHz	1	40	28GHz
Appro	Athlon	1.67GHz	2	113	377GHz
NEC	Intel Xeon	2.8GHz	2	84	470GHz
Total				500	1508GHz

Table 1.10: A breakdown of the PC farm CPU's.

of the compute servers of Sun hosts is employed as a tape server, where two DTF2 tapes, one for the raw data tape and the other for the DST tape, are mounted. Raw data are read on the tape server and then distributed over tens of hosts in the PC farm, where the events are processed. After the event reconstruction, the processed data are sent back to the tape server and are recorded in the output tape as DST.

1.8.3 PC farms

In order to process data quickly, hundreds of rack mountable PC's have been purchased since 1999 and installed into our computing system. The primary purpose was to boost up computing power for the beam data processing as well as the MC production. Recently, we have constructed a new PC farm not only for DST/MC productions but also for user physics analyses. Ten login PC servers have been set up and users can submit her/his jobs into 84 PC compute servers which are operated under the LSF batch queuing system.

Table 1.10 summarizes our PC farms. As we can see, our system is heterogeneous from various vendors. In total, CPU power of 1508 GHz is equipped in our system.

1.8.4 Network

The one remarkable thing related to the network configuration is that so called Super-SINET [55] has been available between KEK and major Japanese universities since 2002. The Super-SINET is the fast network up to 10 Gbps dedicated to academic activities. We also have gotten dedicated 1 Gbps lines to several collaborating groups such as Nagoya and Tohoku universities and Tokyo Institute of technology. As a result, we can mount a disk located at Nagoya university onto a computer at KEK using NFS via this network, and reconstructed beam data have been directly recorded onto the disk as if it were located inside the KEK site.

The Super-SINET is also used for copying a bulk of MC/beam data between KEK and universities.

Chapter 2

Considerations for the detector at super-KEKB

2.1 Expected background conditions

Usually, the vacuum pressures are proportional to the beam currents for each rings since photons from the synchrotron radiation hit the wall of chambers. That's why the Particle background is proportional to the square of the beam current because the number of the scattered particles by the residual gas is proportional to the current times vacuume pressure and the Touschek scattering is described as the function of the square of the current. On the other hand, the synchrotron radiation is just proportional to the beam current. In the Super-KEKB beam currents will be increas to 4.1 A in HER and to 9.4 A for LER. The expected backgrounds at the innermost layer of the SVD 2.0 are shown in Table 2.1. About 17 time higher background is expected if the detector is same. Thus, the detector R&D is performed with assuming at least 17 times higher background than now.

Table 2.1: Radiation doses (kRad/yr) for each backgrounds (BG). Left-side values of the arrows are measurements in our current detector at 1.1 (1.6) A current for HER (LER). Right-side values are extrapolated values assuming that the SR is proportional to the beam current and the Particle background is proportional to the square of the current. It is expected that 17 times higher background if the detector is same.

	outer-direction	inner-direction
Particle-BG (LER)	22 → 759	14 → 483
Particle-BG (HER)	44 → 611	29 → 403
SR-BG	17 → 63	33 → 123
total	83 → 1433	76 → 1009

2.2 Guideline

As mentioned in the chapter of the physics goal, the current performance of the Belle detector system shown in the previous chapter is the minimum requirements on the detector for the SuperKEKB. On the other hand it is eveident that the detector might not be able to keep its capability in the harsh environment expected in the SuperKEKB without extensive upgrade. The biggest concern is the effect of very high occupancy of the detector elements due to extremly severe background from the beam. It might degrade vertexing in the SVD, tracking in the CDC or calorimetry in ECL.

As given above, we can make a natural extrapolation of the background toward the SuperKEKB environment to be 17 times higher than that we have now at the luminosity of $10^{34}\,cm^{-2}s^{-1}$. From our past experience, a quadratic growth of spent particle background could be dumped since the vacuum scrubbing at higher current would always imporve the desorption coefficient of the wall inside the beam pipe. We are, therefore, confident that the above extrapolation is not smaller than what would be. In the present conceputual work, we assume the20 times high occupancy level as a ballpark figure whenever we consider the feasibility of the upgrade.

As for the particle identification, the current performance of the Belle detector is not always ideal and its further upgrade is highly effective for improvement in every physics result discussed in the previous chapter. A material budget is another concern in the upgrade. The current particle identification devices (ACC and ToF) compose a significant part of the material in front of the calorimeter. We are considering several options to realize the better idenification capability. They are discussed in the next chapter.

Because of its inherent inability of high rate counting, KLM is one of the most vulnerable subdetector in the Belle system. Even under the present background condition at the luminosity of $10^{34}\,cm^{-2}s^{-1}$, the outermost two layers in the endyoke are useless due to high count rate. For the detector at the Super KEKB, they should be able to work under 20 times higher background. It is, thus, inevitable to work more seriously on shielding in front of the detector to reduce the bcakground significantly or to replace the present detector elements (RPC) with other class of ones having higher counting capabilty.

2.3 Strategy for tracking/vertexing

2.3.1 Degradation of tracking

At a Super B Factory, in view of charged track reconstruction, a significant demand is to keep the higher reconstruction efficiency and good momentum resolution. These are crucial if an event reconstruction needs a lot of charged tracks, such as the full reconstruction of the other side B meson, and if the tracking efficiency is directly proportional to the physics reach in the extreme rare decay search.

A possible concern under the high occupancy at the $10^{35} \sim 10^{36}$ machine is that an considerable dead time of the gas chamber and its readout system would cause a short of sampling hits to search proper trajectories of charged particles. Small p_t track reconstruction such as a slow π from D^* decay would be even difficult since the number of usable sampling hits are proportional to its p_t, and further, background hits from the effects of beam gas, synchrotron radiation, and spent electrons are locally populated in the inner part of the drift chamber around the interaction point. In this chapter, we concentrate to evaluate the impact to the tracking with a drift chamber under the expected occupancy.

Here, we look into these problems and evaluate the impact of our physics under the target luminosity.

2.3.2 Chamber gas charge up

The huge hit rate would cause a charge up of chamber gas without enough relaxation time. The actual data reveals the limit in terms of the drift chamber operation. Figure 2.1 shows the wire single rates of current CDC at the operation luminosity of $10^{34}/\mathrm{cm}^2/\mathrm{sec}$. The horizontal axis shows the layer number from the inner most and vertical axis is a typical single rate of each sense wire. The inner most sense wire reaches up to 200 kHz of single rate and still works well. This implies at least the sixth layer of the current CDC configuration positioned at 15 cm from the beam axis will work even under 10 times higher single rate. This gives guideline to set the chamber configuration of inner wall.

2.3.3 Dead time of the readout electronics

Another concern is a dead time of a readout electronics. The accidental activity may cloud out proper hits of charged tracks. This causes a decrease of the number of usable hits and further, the degradation of tracking resolution. To estimate the impact, the full simulation of current Belle detector configuration is used to make sure a dominant problem by extrapolating to the expectation under the target luminosity. The background level under our target luminosity, however, widely depends on the design of the beam crossing region, machine vacuum level, beam current, and so on. This means the background level is still unknown. In addition, the KEKB has recently indicated and kept the beam background level as low as that we started the operation three years ago, even with increasing the luminosity up to $10^{34}/\mathrm{cm}^2/\mathrm{sec}$. There is a room to improve the beam background reduction during the accelerator operation by changing the configuration of masks and the vacuum level. Therefore, in this Monte Carlo study, we simply investigate here the track reconstruction efficiency according to several amounts of the accidental overlays within a possible range: the multiplier of the accidental overlay is varied to 1, 5, 10, and 20 times of the current hit map from the actual data in order to reproduce the expected occupancy level of our target luminosity. Also, to make clear the impact of readout dead time, two different dead time are introduced; 2.2 μsec and 0.6 μsec. Historically, Belle

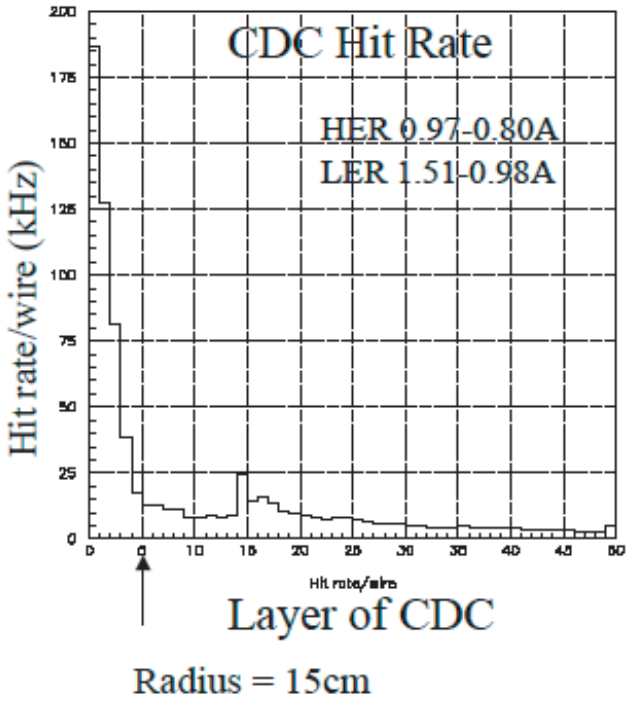

Figure 2.1: CDC single rate under $10^{34}/\mathrm{cm}^2/\mathrm{sec}$ by each wire. The horizontal axis shows the layer number from the inner most and vertical axis is a typical single rate of each sense wire. The inner most sense wire reaches up to 200 kHz of single rate and still works well. This implies at least the sixth layer positioned at 15 cm from the beam axis will work even under 10 times higher single rate.

started with the readout system with 2.2 μsec dead time. Newly developed readout system with 0.6 μsec dead time has been installed in inner three layers in 2003 and the production carries on. These two setups envisage the current and possible reach of reconstruction efficiency and tracking resolution by the improvement of readout system.

Figure 2.2 shows a part of event displays of a $B^0 \to \pi^+\pi^-$ decay with two types of readouts mentioned above under 20 times higher accidental overlay. Blue and red circles indicate properly reconstructed hits on axial and stereo wires, respectively. The left figure shows the track reconstruction with 2.2 μsec dead time while the right figure shows the same track reconstruction but shorter 0.6 μsec dead time. As seen, the shorter dead time configuration(right figure) reconstructs more hits for the track reconstruction. This implies the dead time matters at the track reconstruction in the higher occupancy.

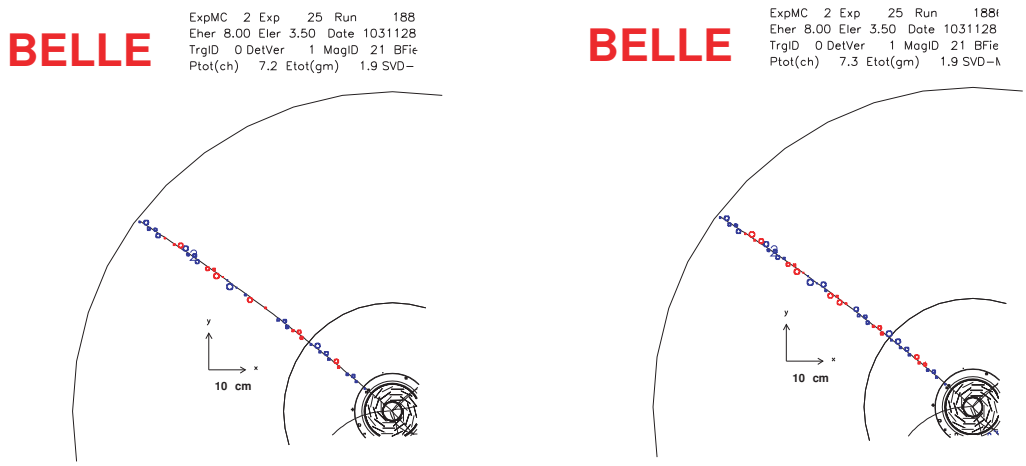

Figure 2.2: CDC Event displays with different electronics. a part of event displays of a $B^0 \to \pi^+\pi^-$ decay with two types of the readouts with different dead time at 20 times multiplied accidental overlay. Blue and red circles indicate properly reconstructed hits on axial and stereo wires, respectively. The left figure shows the track reconstruction with 2200 nsec dead time mostly from the electronics while the right figure shows the same reconstruction but 600 nsec dead time. As seen, shorter dead time configuration(right figure) gives more reconstructed hits for the track reconstruction.

Figure 2.3 shows the reconstruction efficiency of $B^0 \to \pi^+\pi^-$ decay with varying the amount of accidental overlay. The other side B is assumed to decay according to its natural branching fraction. The reconstruction is done by choosing two charged tracks properly reconstructed which satisfies a loose B meson mass constraint. The left figure shows the reconstruction efficiencies of $B^0 \to \pi^+\pi^-$ decay including the geometrical acceptance and the right one is the square root of the reconstruction efficiency in the left figure, which is approximately the single track efficiency of medium to high momentum tracks. The degradation of tracking efficiency is not significant with 0.6 μsec configuration while a fall is seen with 2.2 μsec configuration. The single track efficiency gives only a few percents fall with 0.6 μsec dead time electronics. This implies the current CDC system is still usable for medium to high momentum charged tracks under the higher occupancy even with current detector configuration, electronics, and hit search/track reconstruction algorithm.

To look at an impact on the slow π reconstruction, The same simulation is done for $B^0 \to D^{*-}(\to \bar{D}^0\pi_s^-)\pi^+$ decays. Figure 2.4 shows the result. The left figure shows the reconstruction

efficiency of $B^0 \to D^{*-}(\to \bar{D}^0\pi_s^-)\pi^+$ decays(and c.c.) including the detector geometrical acceptance. The right figure shows the slow π reconstruction efficiency estimated from the efficiency of $B^0 \to D^{*-}\pi^+$ decay divided by that of $B^- \to D^0\pi^-$ decay. This result indicates the slow π efficiency is degraded according to the increase of the occupancy. This is because the length of trajectory of slow π is short and only in the inner part of the detector where the single rate is very high, and usable hit is only a few. Figure 2.5 shows the situation. The left figure shows the failed reconstruction of a slow π under 20 times higher accidental overlay while the right figure is the succeeded reconstruction indexed as '10' without any accidental overlay for the same event. The actual Monte Carlo trajectory is almost same as the succeeded reconstruction but has a kink by the multiple scattering. Under the high occupancy, we still have some hits to reconstruct the slow π by our eyeball fit. Therefore there is a chance to recover this kind of slow π tracks by improving the reconstruction algorithm.

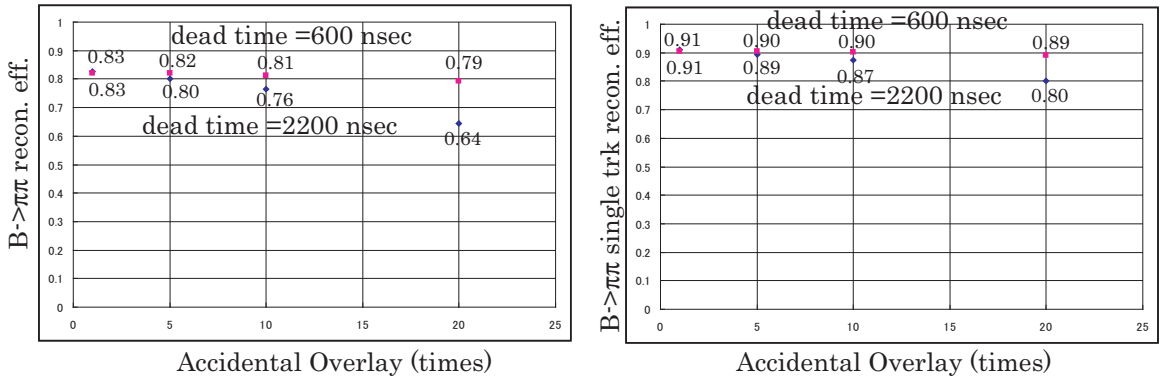

Figure 2.3: The reconstruction efficiency of $B^0 \to \pi^+\pi^-$ decay. $\bar{B}^0 \to$ anything with varying the amount of accidental overlay. The left figure shows $B^0 \to \pi^+\pi^-$ decay including the geometrical acceptance and the right is a square root of the reconstruction efficiency in the left figure, which is approximately the single track efficiency of medium to high momentum tracks.

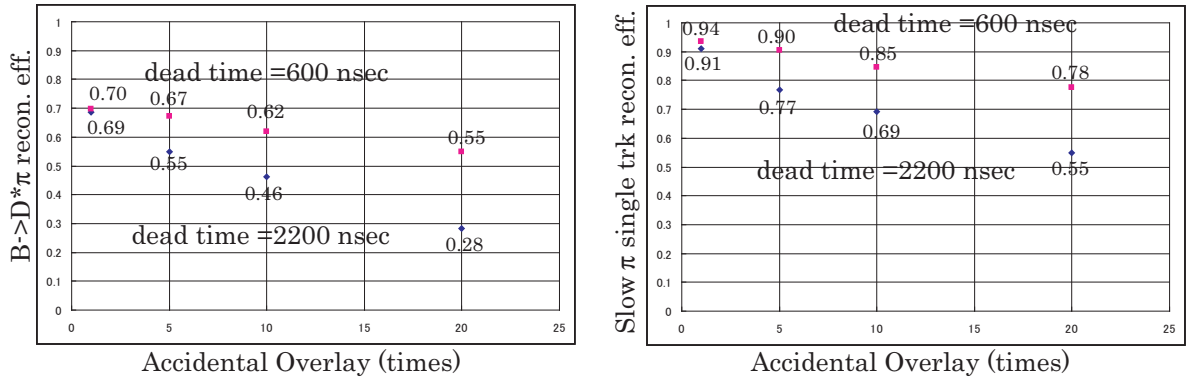

Figure 2.4: Reconstruction efficiency of $B^0 \to D^{*-}(\to \bar{D}^0\pi_s^-)\pi^+$ decays in terms of the amount of accidental overlay. The left figure shows the reconstruction efficiency of $B^0 \to D^{*-}(\to \bar{D}^0\pi_s^-)\pi^+$ decays(and c.c.) including the detector geometrical acceptance. The right figure shows the slow π reconstruction efficiency estimated from the efficiency of $B^0 \to D^{*-}\pi^+$ decay divided by that of $B^- \to D^0\pi^-$ decay.

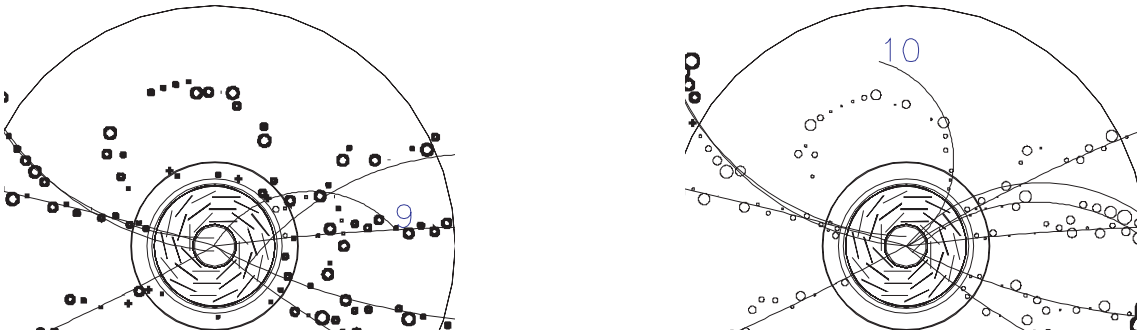

Figure 2.5: Event display of the slow π reconstruction. The left figure shows the failed reconstruction of a slow π under 20 times accidental overlay while the right figure is a succeeded reconstruction indexed as '10' without accidental overlay in the same event. The actual Monte Carlo trajectory is almost same as the succeeded reconstruction but has a kink by the multiple scattering.

2.3.4 Degradation of the vertex resolution

A high precision vertex detector is essential for CP violation studies at the B-factory experiments. At a higher luminosity environment as the Super-KEKB, large beam backgrounds are expected which possibly deteriorates the vertex resolution. Therefore, in this section a prospective simulation study based on the current vertex detector SVD2 is presented.

To simulate this environment, the random-triggered events recorded with the SVD2 were overlaid on the MC generated events. Here, we assumed the next four conditions; "no background overlaid", "the nominal background", "the nominal background increased by a factor 2" and "the nominal background increased by a factor 5". Furthermore, all detectors but SVD2 remained in the no-background condition for check the background effect only on the SVD2.

The vertex resolution along the z-axis was determined for the specific decay mode, the CP-side B decayed in $J/\psi K^0_S$ while the tag-side B decayed freely. The residual between the reconstructed and generated B vertex position is summarized in Fig. 2.6 with the difference of the reconstructed ΔZ and generated one. As can be seen in Fig. 2.6, more than 40% degradation relative to the nominal background case was observed under the 5$\times$ background environment. This is partially because the occupancy in the innermost layers of the overlaid random-triggered events is about 50% and partially because an adequate algorithm for differentiating the signal from the background has not been fully tuned at this stage. This makes difficult to find out true hit cluster from a heap of fake ones.

To clarify the background effect on the innermost layers from the others, two supplemental conditions were tested. One is the 5$\times$ background only on the innermost layers without any background on the remaining and the other is vice versa. Figure 2.7(b),(c) and (d) show the resulting ΔZ vertex resolutions for "5$\times$ background on all layers", "5$\times$ background only on the innermost layers" and "5$\times$ background except for the innermost layers",respectively. For comparison, the result in the nominal background case is also presented in Fig. 2.7(a).

These figures indicate that the rms of the ΔZ residual distribution gets significantly worse once the background on the innermost layers are taken into considerations for detemining the

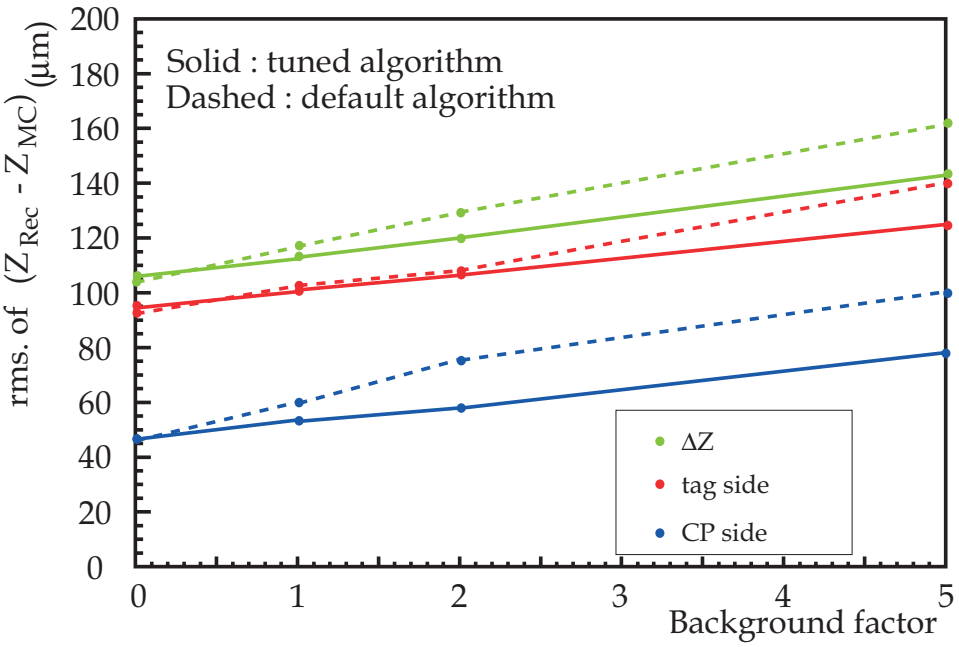

Figure 2.6: The background dependence of the vertex resolution

vertex position. In other words, reducing the background effect on the innermost layers is one of the most important issues to achieve the good ΔZ vertex resolution.

From this SVD2 case study, however the details are still under investigation, the high granularity and the low hit occupancy especially in the inner layers are simultaneously required for the hardware. For the software side, the effective algorithm capable to differentiate the signal cluster from the background is also necessary.

2.3.5 Strategy

As shown above, a conventional drift chamber is a viable option for the tracker outside the radius of 15 cm if proper reduction of occupancy is realized by applying shorter dead time elecronics, shorter drift time and so on. With a smaller drift cell configuration, the expected occupancy can be reduced to the level of 10 times of the present one so that the predicted degradation of tracking efficiency is as small as 1 for higher momentum tracks and 10 can be improved much by developping a special tracking code for slow particles. As for vertexing, the shaping time of the present electronics can be reduced with a modern ASIC chip by a factor of five and the expected occupancy for the layer placed at the position of the 1st layer of the present SVD2 could be reduced to the 4× level. Further reduction is also possible by a proper optimaization of the design of sensors. In this way, we can expect the degradation of vertexing to be kept within 10the conventional technology with a silicon microstrip detector. Our base line option for the tracker is, therefore, the silicon micro strip tracker (r¡15cm) surrounded by a small cell drift chamber which would enable to reconstruct tracks under a Super KEKB environment as well as the present Belle does.

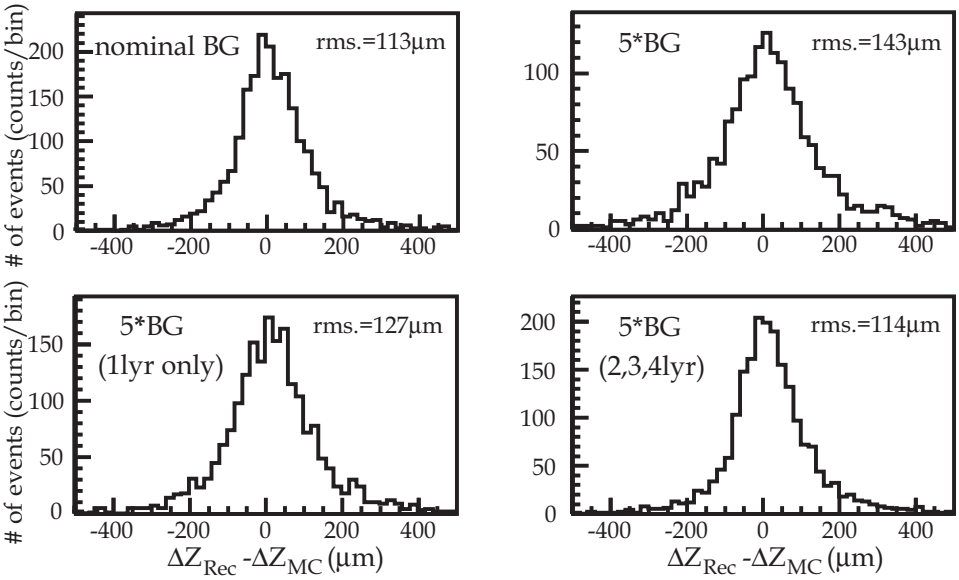

Figure 2.7: The residual of the ΔZ between the reconstructed and generated B vertex.

2.4 Strategy for Calorimetry

As mentioned in the previous chapter, the average number of the background photons with energy more than 20 MeV is 3 per events: one fake photon comes to the barrel and the other two come to the endcaps for the luminosity of $5 \times 10^{33}\,\mathrm{s}^{-1}\mathrm{cm}^{-2}$ If the background is 20 times higher, we will have about 60 background showers which exceed 20MeV. Such a number of fake clusters will cause additional combinatorial background. The combinatorial background can be suppressed by applying a tighter cut on the minimal photon energy which will result in a decrease of the π^0 efficiency.

Another concern is low energy background photons which overlap with a real signal and induce smearing effect (pileup noise).

The pileup noise is proportional to the fluctuations of the number of background photons, so we can expect that the coefficients $\alpha_{HER},\ \alpha_{LER}$ in Eq.(1.5) are proportional to the square root of the product of the currents and vacuum pressure:

$$\sigma = \overline{E_\gamma}\sqrt{\nu\tau_{eff}} \sim \sqrt{IP}, \tag{2.1}$$

where $= \overline{E_\gamma}$ is the average background photon energy, ν is the average background rate, τ_{eff} is a sensitive time of a counter which is determined by the decay time of the scintillator and the shaping time of the electronics, I is the beam current and P is the vacuum pressure around the IP region. Figure 2.8 shows dependence of the coefficient $\alpha_{HER},\ \alpha_{LER}$ on $\sqrt{IP}$, which does not contradict to Eq. (2.1).

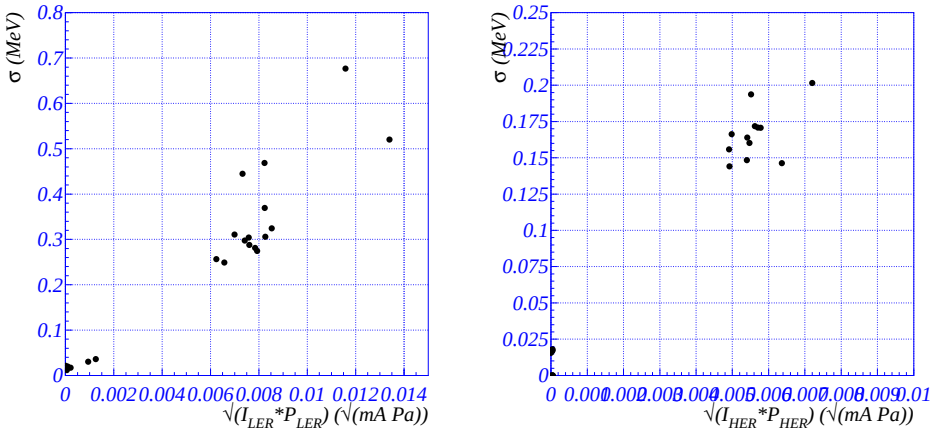

Figure 2.8: Dependence of the pileup noise on $\sqrt{PI}$ for $\theta \approx 90°$.

Assuming the dependence of Eq (2.1) we extrapolate the pileup noise behavior to the luminosity $10^{35}\,\mathrm{s}^{-1}\mathrm{cm}^{-2}$. In the barrel the pileup noise will be of the order of 0.7-1.5 MeV while in the backward endcap it can be up to 4 MeV. Such a noise will deteriorate the energy resolution for low energy photons.

2.4.1 Improvement of calorimeter performance

To keep sufficient performance in the high background environment, we have to find a way to suppress a fake hit rate and pileup noise. The beam crossing interval is much shorter than the decay time of the scintillation and shaping time constant of the electronics, so that we can

assume that the timing of fake hits due to beam background photons uniformly distributes with respect to the real physics events. Consequently, we can distinguish the fake hits from real hits by measuring the timing of calorimeter hits and comparing them to the event timing determined by either among calorimeter crystals or other detector subsystems.

By utilizing wave-form sampling with pipeline readout, we can reconstruct the counter hit timing and can reduce pileup noise effect. A counter signal is continuously digitized with $0.5\mu s$ clock interval and several measurements are recorded when trigger comes. In order to maximize such digital signal processing effect, analog electronics should optimized as well. We plan to use shorter shaping time $\tau = 0.5\mu s$ instead of current value of $1\mu s$ [1]. In this section, signal hit reconstruction method by wave-form sampling readout is described and changing the crystal into pure CsI in the Endcaps is discussed as well.

Since the pileup noise is due to overlapping of signals, another possible way to reduce it is to decrease a signal duration. The simplest way is to use shorter shaping time of the electronics. However, making the shaping time essentially smaller than the decay time of the scintillator, leads to the effective increase of the electronic noise. We plan to reduce the shaping time from $\tau = 1\mu s$ to $\tau = 0.5\mu s$.

2.4.2 Signal hit reconstruction

To estimate effects of the beam background for the current calorimeter and test the performance of possible upgrades, we've carried out MC which took into account the signal shape and the background measured under present conditions.

To simulate pipeline readout, we assume the obtained signal amplitudes (s_i) are recorded in 16 points around the maximum of the signal with a time interval $\Delta t = 0.5\mu s$.

For each set of the generated data(s_i) the magnitude A and time t_0 are reconstructed by χ^2 minimization:

$$\chi^2 = \sum_i (s_i - AF_c(i\Delta t - t_0))(S^{-1})_{ij}(s_j - AF_c(j\Delta t - t_0)) \rightarrow min, \tag{2.2}$$

where S is an error matrix which is calculated according to the electronics and pileup noise correlation.

Figure 2.9 shows the MC results for the difference between the reconstructed and true time of pulse about the signal and fake clusters. Knowledge of the reconstructed time t_0 allows to suppress the number of the fake reconstructed photons. Applying a cut $|t_0 - t_{trig}| < 500ns/E(MeV)$, where t_{trig} is the true event timing which is given by the trigger in real experiment, we suppress the number of the fake photons by a factor of 7, keeping the efficiency of the cut for real photons at more than 90% for photon energies above 20 MeV. For the case of background increase by a factor of 5 and new readout scheme the number of fake photons will be even smaller. However, for the case of 20 times larger background the pileup noise will be a factor of 3 larger than we have now. In this case we'll need to increase the photon threshold up to 30 MeV to keep the same level of the combinatorial background.

The pileup noise behavior for the current and upgrade electronics is shown in Fig. 2.10. For the case of 5 times larger background the pileup noise will be at the level which we have at the Belle calorimeter now, however, in case of the 20 times higher background the pileup noise of the barrel will be about 0.8 MeV/counter. For that value of the pileup noise its contribution to

[1] Making shaping time shorter than the decay time of the scintillation leads to effective increase of the electronics noise.

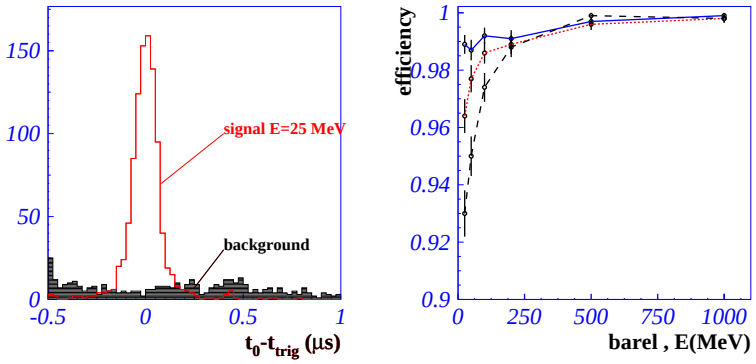

Figure 2.9: a)The time distribution for signal and fake photons. b)Inefficiency due to the time cut for different background conditions. Solid line – 5 ($E > 20$ MeV) clusters per barrel; Dotted line – 10 ($E > 20$ MeV) clusters per barrel; Dashed line – 20 ($E > 20$ MeV) clusters per barrel.

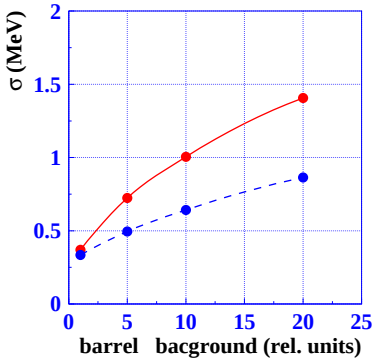

Figure 2.10: Dependence of the pileup noise per crystal for the current (solid line) and modified(dashed line) barrel calorimeters. The background at Belle for $10^{34}\,cm^{-2}s^{-1}$ is taken for unity.

the energy resolution of the calorimeter will be comparable to the shower fluctuation effect at one hundred MeV.

Such suppression of the background is not enough for the endcap case. The next possible step is to use a scintillator with a shorter decay time and proportionally to decrease the shaping time. The pileup noise will decrease $\sim \sqrt{\tau}$ and fake photons rate $\sim \tau$.

2.4.3 Pure CsI for the endcap

The characteristics of heavy scintillating crystals with a short decay time are listed in Table 2.2. Scintillators such as BaF_2, CeF_3, $PbWO_4$ have a low light output. Characteristics of Lu-based scintillators are reasonably good but such scintillators are very expensive (more than 20\$/cm^3) and there is no large scale production of these scintillators. Pure CsI that has a short decay time of about 30 ns and sufficiently high light output is not so expensive (3.5\$/cm^3). Having the same physical parameters as CsI(Tl) used in the barrel, pure CsI is a good candidate for a material in endcaps.

The light output of pure CsI crystals is lower than that for doped crystals, so to keep the

crystal	ρ, g/cm^3	X_0, cm	λ_{em}, nm	n	N_{ph}/MeV	τ, ns
CsI(Tl)	4.51	1.86	550	1.8	52000	1000
CsI	4.51	1.86	305/400	2	5000	30/1000
BaF_2	4.89	2.03	220/310	1.56	2500/6500	0.6/620
CeF_3	6.16	1.65	310	1.62	600	3
$PbWO_4$	8.28	0.89	430	2.2	25	10
$LuAlO_3$(Ce)	8.34	1.08	365	1.94	20500	18
$Lu_3Al_5O_{12}$(Ce)	7.13	1.37	510	1.8	5600	60
Lu_2SiO_5(Ce)	7.41	1.2	420	1.82	26000	12/40

Table 2.2: Characteristics of some heavy scintillators.

electronic noise value at the same level one needs to use photodetectors with internal gain. One of the option is to use vacuum phototetrodes. Hamamatsu has developed 2" UV sensitive phototetrodes R2185UV with a low output capacity C$\approx$ 10 pF. The low capacity is important since the charge sensitive preamplifier noise is proportional to that value. These devices have a quantum efficiency of about 15-20% and internal gain factor of about 40-60. We tested several pure CsI crystals of the same size as the endcap calorimeter counters. The light output and nonuniformity distribution for these counters are shown in Fig. 2.11. Using the crystals and the

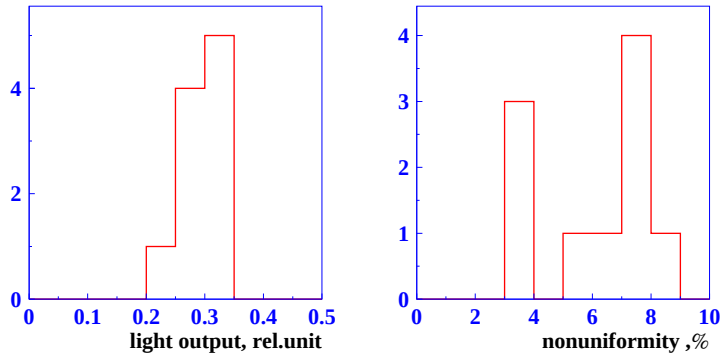

Figure 2.11: Light output and nonuniformity distribution for 10 pure CsI counters.

phototetrodes(PT), we constructed counters shown in Fig. 2.12. The phototetrode is connected to the pure CsI crystal via an optical grease. The anode of the phototetrode is connected to the input of the standard preamplifier used in the Belle calorimeter. The signal from the preamplifier goes to a specially designed electronic CAMAC module consisting of the CR-$(RC)^4$ shaper with a shaping time τ = 30ns and 2×12bits flash ADCs working with a clock time Δt = 30ns. The obtained noise of this electronics is about 980 electrons while the light output varies from 5000 to 9000 electrons per MeV. The energy noise equivalent(ENE) for such a case is 110-180 keV. In the magnetic field the gain factor of the phototetrode is decreasing but still is reasonably high (Fig. 2.13). Taking into account the degradation of the gain factor due to the magnetic field we can expect the ENE of about 400-500 keV for the magnetic field of 1.5 T. The cosmic spectrum obtained with such counters is shown in Fig. 2.14. Hamamatsu hopes to get a higher quantum efficiency and gain factor of the phototetrodes but even the current electronic noise is lower than the pileup noise we have for $L = 10^{34}\,\mathrm{cm}^{-2}\mathrm{s}^{-1}$. Usage of the scintillator and electronics with a

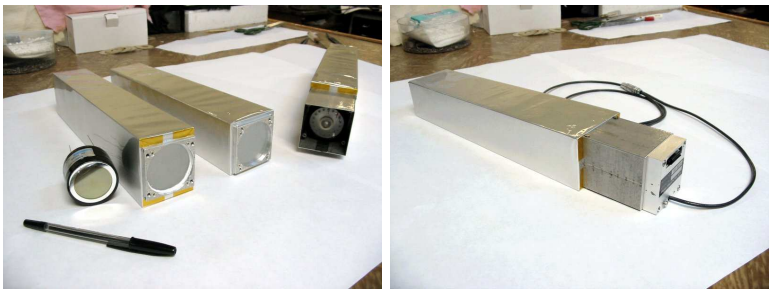

Figure 2.12: Pure CsI counters.

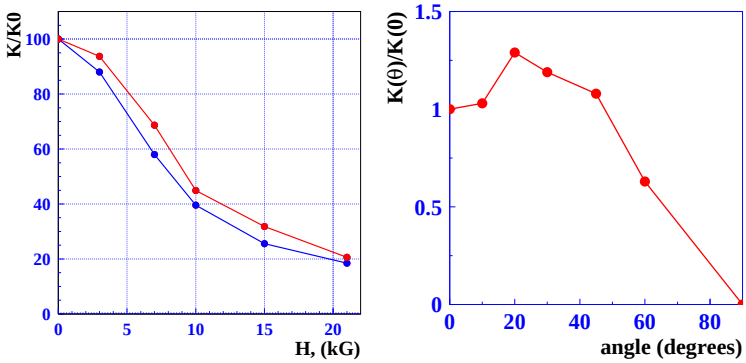

Figure 2.13: a) Gain factor dependence on the magnetic field along the phototetrode axis b) Gain factor dependence on the angle between the magnetic field direction and the phototetrode axis, H=15 kG.

shorter time allows to suppress the pileup noise by a factor of about 5.5 as has been shown by MC simulation. We have also carried out a direct comparison of the pileup noise for the counter based on pure CsI and one of the CsI(Tl) counter from the Belle detector. The pileup noise was simulated by photons from a ^{60}Co radioactive source. The background intensity was varied by changing the distance between the Co-source and crystals. The pileup noise was calculated from the width of the test pulse signal. Figure 2.15 shows the effective noise of the pure CsI counter depending on that of the CsI(Tl) counter. The results of the measurement agree with the MC prediction.

The shorter time of the crystal and shaper allows to suppress the effect of fake photon rate. Since there will be a few thousand bunches distributed uniformly along the ring, we assume that the fake photon background is uniformly distributed in time. Under this assumption the number of fake photons will be a factor of $\tau_{CsI(Tl)}/\tau_{pureCsI} \approx 33$ lower.

Another suppression factor can be obtained by using wave shape analysis. In the case of pipeline readout a signal amplitude is continuously digitized every clock time $\Delta t \approx 24ns$ and several measurements around the signal maximum are recorded when trigger comes. From the wave shape analysis we obtained both the amplitude and time of the signal. According to Monte Carlo simulation, applying time cut we can suppress the fake photon rate background by an additional factor of 5. Thus, we have a resulting suppression factor $33 \times 5 \approx 160$.

Pure CsI calorimeter is a good option for the endcap calorimeter. Even in the case of 20 times larger background the resulting fake rate is expected to be lower than in the current barrel

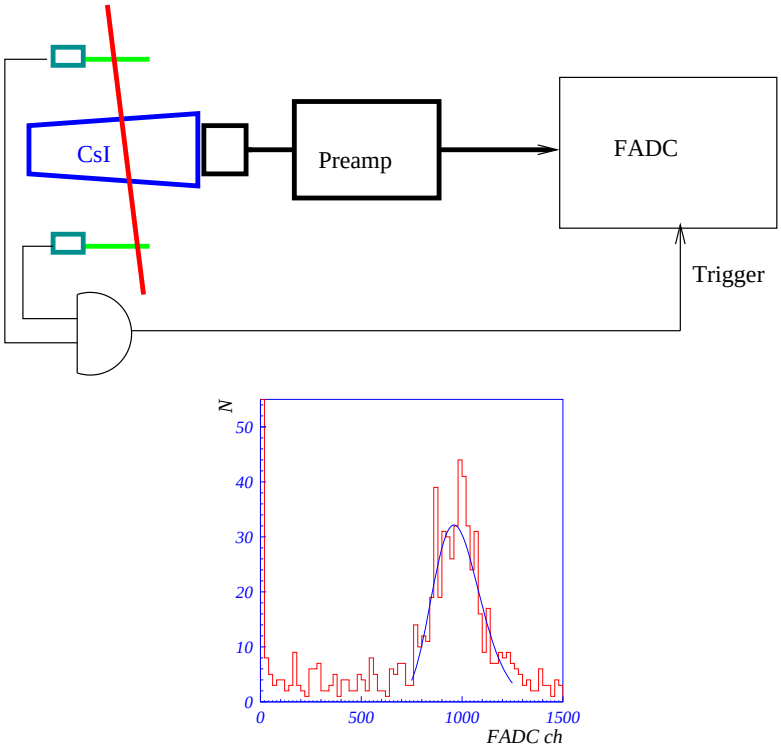

Figure 2.14: Cosmic spectra from the counter.

calorimeter.

The approximation of the pileup noise for the higher background is shown in Fig. 2.16. Even for the background a factor of 20 higher than now the pileup noise with pure CsI crystals is at an acceptable level.

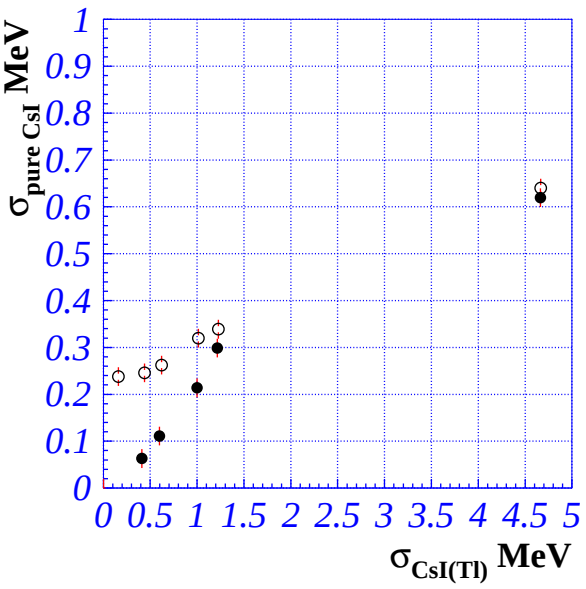

Figure 2.15: Noise of pure CsI counter as function of the noise of the standard Belle CsI(Tl) counter. Open points are the width measurement, black points are results after the electronic noise subtraction – only pileup noise effect.

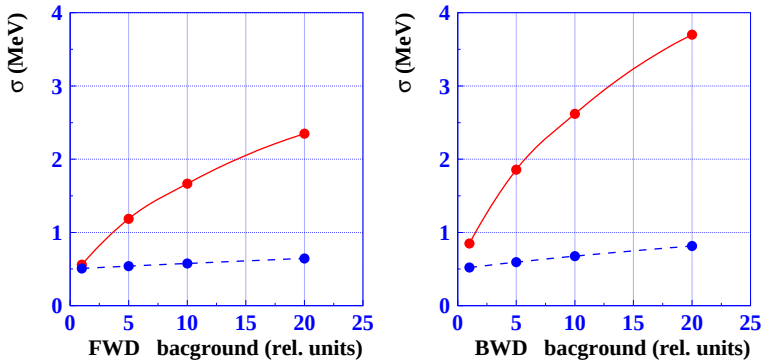

Figure 2.16: Dependence of the pileup noise for the current (solid line) and modified (dashed line) endcap calorimeters on the background. The background at Belle for 10^{34} cm^{-2}s^{-1} is taken for unity.

2.5 Requirements for Particle Identifier

2.5.1 Impact of PID Improvement on Physics Reach

Particle identification, especially the K/π separation, plays a crucial role in the B-factory experiments. This situation will remain unchanged also at the Super-KEKB/Belle experiment, which aims at precise test of Kobayashi-Maskawa scheme for the CP violation and search for new physics effects in B meson decays. For the precise measurement of the ϕ_1, ϕ_2 and ϕ_3 angles, the particle identification is essential in the following aspects.

- Flavor tagging in any type of time-dependent CP asymmetry measurements.
- Reconstruction of charmless two-body decays such as $B \to \pi\pi$, $K\pi$, ϕK and $\eta' K$.
- Reconstruction of $B \to DK$ and $D\pi$ decays.

Moreover, in search for new physics effects in B meson decays, importance of the K/π separation increases. One such example is;

- $b \to s\gamma$ and $d\gamma$ decays; it is noted here that these two decays have only weak kinematical separation and also that the branching fraction of $b \to d\gamma$ is expected to be at least an order of magnitude lower than the $b \to s\gamma$.

Another aspect to be considered is the μ/π separation in the momentum region below 0.7 GeV/c, where the KLM detector cannot be used for the muon identification. A typical example is;

- Forward-backward asymmetry A_{FB} in $b \to s\ell^+\ell^-$.

In order to meet these requirements, the upgraded PID system should have more than 4 σ K/π separation in the wide momentum region up to 4 GeV/c. Such system would provide similar μ/π separation up to 0.7 GeV/c.

In following, impacts of PID improvement are demonstrated for some bench-mark physics channels.

Measurement of $B \to \rho\gamma$

This mode proceeds through the $b \to d\gamma$ process, and is useful for the measurement of $|V_{td}|$. $B^+ \to \rho^+\gamma$ can be also used to measure the CP asymmetry, which is expected to be large in the SM. The time-dependent asymmetry of $B^0 \to \rho^0\gamma$ is expected to be small in the SM, but can be large in some non-SM models. Hence, this mode is a sensitive probe for new Physics.

However, $B \to \rho\gamma$ decays suffer large background from $B \to K^*\gamma$ decays by mis-identifying a kaon from K^* as a pion, because $b \to d\gamma$ is suppressed by the factor of $|V_{td}/V_{ts}|^2 < 0.06$ compared to $b \to s\gamma$. The branching fraction of $B \to \rho\gamma$ is predicted to be $(0.85 \pm 0.30 \pm 0.10) \times 10^{-6}$ and $(0.49 \pm 0.17 \pm 0.04) \times 10^{-6}$ for the charged and neutral mode [8], while that of $B \to K^*\gamma$ is around 4×10^{-5}. Therefore, the separation of kaons and pions is a critical issue for the study of $B \to \rho\gamma$.

The effect of the PID to the experimental sensitivity is studied using simple FSIM program. The reconstruction of $B \to \rho\gamma$ is performed for the $B \to K^*\gamma$ and $B \to \rho\gamma$ MC samples. The selection criteria are based on the present analysis at Belle: we apply π^0/η veto, $|M(\pi\pi) - M_\rho| <$ 200 MeV/c^2 and $|M(K\pi) - M_{K^*}| > 80$ MeV/c^2, where M_ρ (M_{K^*}) is the nominal $\rho(K^*)$ mass and $M(K\pi)$ is the invariant mass of the two pions assuming kaon mass for the higher momentum

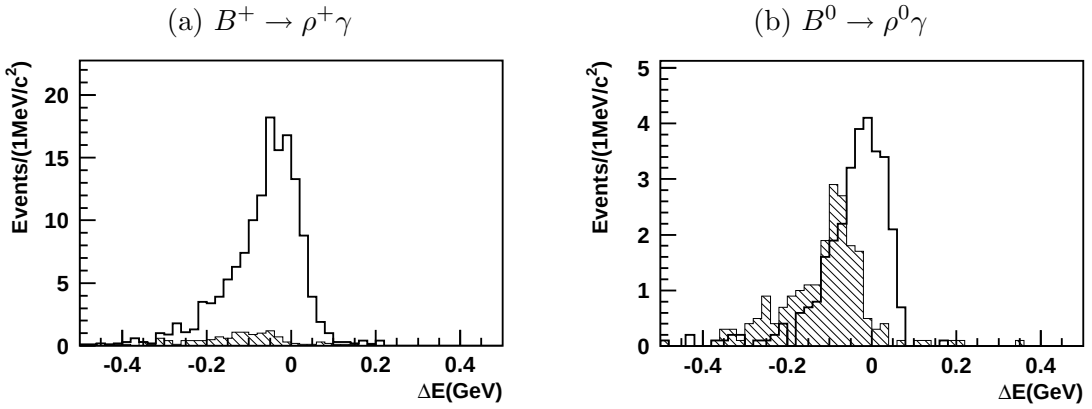

Figure 2.17: ΔE distribution for (a) $B^+ \to \rho^+\gamma$ and (b) $B^0 \to \rho^0\gamma$. Open histograms show the $B \to \rho\gamma$ signal, while shaded histograms show the contributions from $B \to K^*(892)\gamma$ assuming 3% of kaon-to-pion misidentification rate. Histograms are scaled to 5 ab^{-1}.

charged pion. The selection criteria for continuum background suppression are not applied. We assume 10% efficiency for this kind of selections, and scale the histograms afterward. In order to see roughly the contribution of the PID performance to the study, the π efficiency is fixed to be 90% and the mis-identification rate is varied. For simplicity, the performance is assumed to be independent of the momentum of the charged particle.

Figure 2.17 show the ΔE distributions after applying $M_{\rm bc} > 5.27$ GeV/c^2, assuming 3 % mis-identification rate. The histograms are scaled to 5 ab^{-1}, taking into account the assumed 10% efficiency for continuum background suppression. The distributions for the $B \to K^*\gamma$ are shifted by around -100 MeV because of the mass difference between kaons and pions. However, the ΔE distribution for the signal also has a large tail in the lower side mainly due to the energy leakage of the high energy photons at the calorimeter. So, this energy shift is not enough to separate $B \to \rho\gamma$ and $B \to K^*\gamma$. As seen from Fig. 2.17, 3 % mis-identification rate is still too large to separate $B^0 \to \rho^0\gamma$ events from $B\ to K^*\gamma$ background.

Figure 2.18 shows the relation between S/N and kaon-to-pion misidentification rate. Here, S/N is the ratio of the number of $B \to \rho\gamma$ signal and $B \to K^*(892)\gamma$ background events that fall into -200 MeV/$c^2 < \Delta E < 100$ MeV/c^2. In order to make the $B \to K^*(892)\gamma$ background small enough, the misidentification rate of less than 1% ($\sim 4\sigma$ K/π separation) should be achieved.

μ/π separation for $b \to s\ell^+\ell^-$

The contribution of the PID system to the separation between muons and pions is also useful for various physics, because the KLM detector cannot identify muons with momentum less than 0.7 GeV/c^2. An example of such a physics is the $b \to s\ell\ell$ process. This process is considered to be sensitive to non-SM physics, and, in order to explore New Physics, we measure the $\hat{s}$ dependence of the branching fraction and forward-backward asymmetry $A_{\rm FB}$ both for inclusive and exclusive modes. Here, $\hat{s} = M^2(\ell^+\ell^-)/M_B^2$ (M_B is the B meson mass). Because the contribution of $c\bar{c}$ resonances such as J/ψ causes theoretical uncertainty in the region $\hat{s} \geq M_{J/\psi}^2/M_B^2$, measurement at low $\hat{s}$ region is important.

Figure 2.19 shows the $M^2(\ell^+\ell^-)$ distribution for the $B^+ \to K^+\ell^+\ell^-$ signal MC, assuming 50 ab^{-1} for various μ momentum selection. Here, muon identification efficiency is assumed to be 90% independent of the momentum. As seen from the figure, the efficiency at $M^2(\ell^+\ell^-) <$

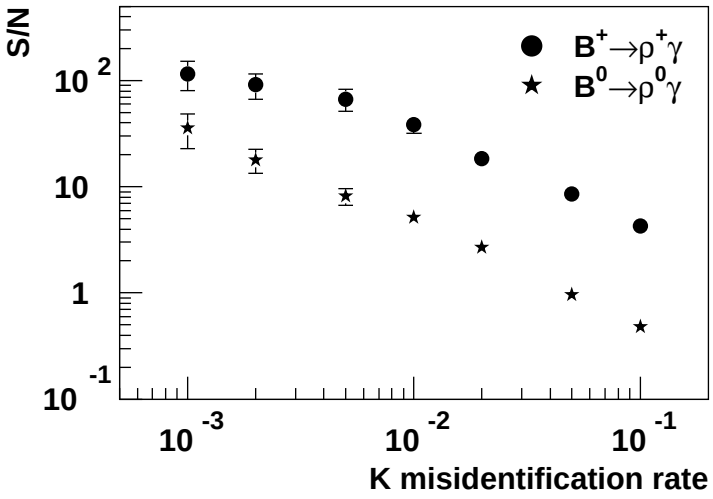

Figure 2.18: Ratio of the $B \to \rho\gamma$ signal the and $B \to K^*(892)\gamma$ background (S/N) for various kaon-to-pion misidentification rate.

9 GeV/c^2 is increased as the minimum momentum of the μ selection is lowered. If we can separate muons at a low momentum region, we can increase the signal events at low $\hat{s}$ region resulting in better measurement on the branching fraction and $A_{\rm FB}$.

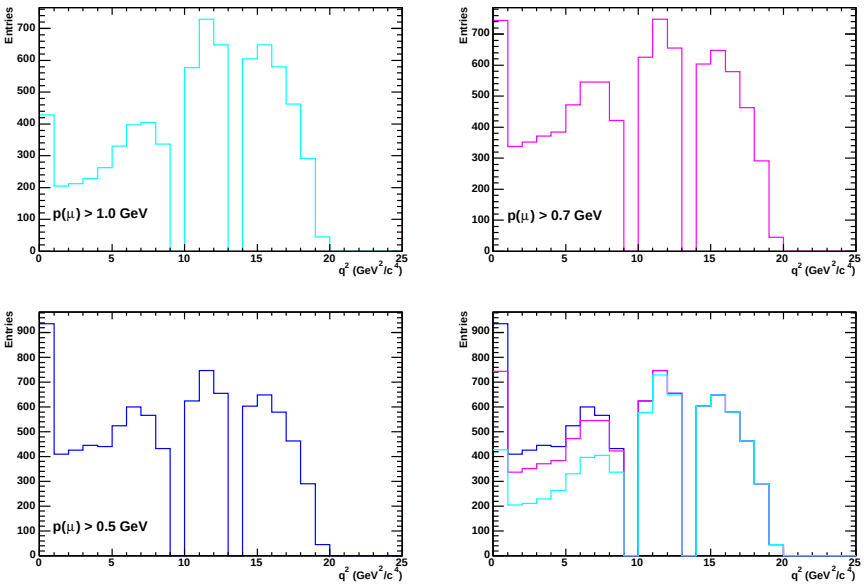

Figure 2.19: $q^2 = M^2(\ell^+\ell^-)$ distribution for $B^+ \to K^+\ell^+\ell^-$ signal MC assuming 50 ab^{-1}, for $p(\mu) > 1$ GeV/c^2, $p(\mu) > 0.7$ GeV/c^2 and $p(\mu) > 0.5$ GeV/c^2.

Table 2.3: Operating conditions for the Trigger and DAQ at Belle and requirements for Super Belle

	Belle ($L = 10^{34}$)	Super Belle ($L = 10^{35}$)
Physics trigger rate (Hz)	100	1K
Actual trigger rate (Hz)	500	10-30K
Event size at L1 (KBytes/event)	40	200-300
Data flow rate at L1 (MBytes/s)	20	>2000
Data flow rate at storage (MBytes/s)	10	<250
Reduction factor in DAQ	2	10

2.6 DAQ requirements

Table 2.3 shows the current condition of the trigger and data acquisition system together with the expectations at SuperKEKB. The trigger rate at SuperKEKB is estimated from a linear extrapolation of the measured rate at Belle scaled by the luminosity. The expected increase in the background rate is also taken into account in the calculation. The event size is expected to increase up to a few hundred Kbytes because of the wider use of pixel detection devices and wave form sampling to cope with the high occupancy. The resulting data flow after the Level 1 trigger will be more than 2GBytes/sec. An event reduction rate in the current DAQ system of 2 at the Level 2.5 trigger is obtained by requiring the vertex to be within a fiducial region. If the same reduction factor is assumed at SuperKEKB, the data flow at storage reaches more than 1GBytes/sec, which is very difficult to manage. A sophisticated data reduction close to a factor of 10 is required in the data acquisition system in order to have a manageable data storage rate of less than 250MB/sec.

Chapter 3

SuperBelle at SuperKEKB

3.1 Beampipe and expected beam background for Super-KEKB

As described in section 1.1.3, the design of the beampipe for SVD 2.0 was succesfull, and our simulation is reliable. We would like to use a smaller radius beampipe (1 cm) in Super-KEKB. The design of the beampipe is almost the same as the SVD 2.0. The differences are the beampipe radius, the SR-mask shape, and the larger apertures at both ends of the Tantalum pipes.

We should not reduce the height of the SR-mask because of the large background from Soft-SR (2 MRad/yr) at the first layer of the SVD. The doses for various mask heights are shown in Figure **??**-(a). The machine parameters used in the simulation are; 33 nm for the horizontal emittance, 6.4 % for $x - y$ coupling, $\beta_x^*/\beta_y^* = 30$ cm / 0.3 cm, 4.1 A (9.1 A) of HER (LER) beam current, 100 days/yr of operation time with full currents, 3 mA/sec and 10 min for the injection rate and time, respectively, and 20 injections/day is assumed. The doses in the horizontal direction on the forward side (FWD), which is the downstream side of the HER, are strongly dependent on the mask height. The dose is reduced to 200 kRad/yr when we use the same height for the SR-mask as in SVD 2.0. Moreover, we can reduce the Soft-SR dose to ~ 80 kRad/yr if we use a ϕ-symmetric shape mask as shown in Figure 3.1-(b). About 50 kRad/yr dose comes from the magnet QC2 during beam storage while the contribution of QC1 is high during beam injection.

Hard-SR is not sensitive to the reduction of the beampipe radius while the Soft-SR component is very sensitive to the beampipe radius. The expected dose from Hard-SR is only 150 kRad/yr, and the total expected dose is 230 kRad/yr.

On the other hand, much higher backgrounds are expected from the lost particle component. A dose of about 3 MRad/yr dose at the first layer of the SVD is expected assuming a 1 nTorr pressure for CO. Thus, the background will be dominated by the particle component. At the first layer of the SVD, the total background is expected to be about 30 times higher than in the case of SVD 2.0. The radiation hardness of the DSSD (10 MRad) and the readout chips (20 MRad) are still larger than the expected radiation dose, and they can be improved with lower temperature operation.

We can calculate the heating in the same way as for SVD 2.0. The difference of the SR-mask shape slightly changes (+0.8 / -4.5 %) the HOM heating. The expected heating is 780 W total. This can be handled with a higher flow rate of the cooling liquid.

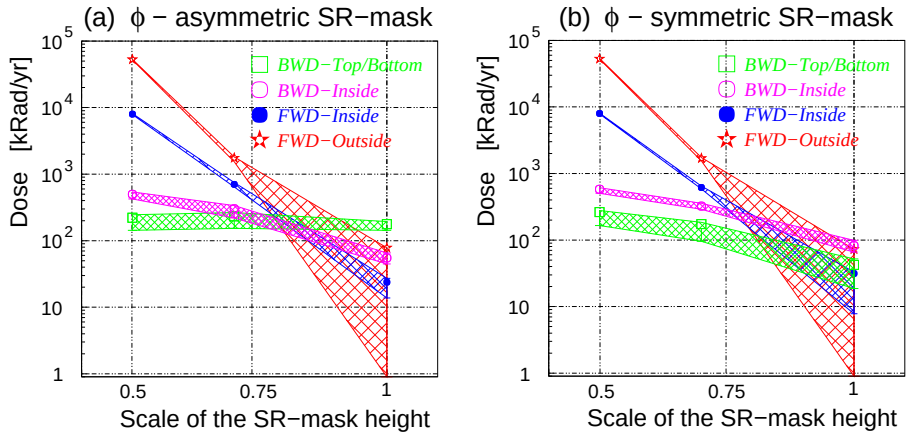

Figure 3.1: The correlation between the mask hight and the expected dose at the first layer of the SVD in Super-KEKB for a (a) ϕ-asymmetric and (b) ϕ-symmetric SR-mask. The horizontal axis indicates the mask height; the same height as the SVD 2.0 mask corresponds to a scale of 1.

3.2 Vertex Detector

3.2.1 Overview of VTX for SuperKEKB

The vertex detector (VTX) at a high-luminosity asymmetric e^+e^- collider is indispensable for time dependent physics that includes precise measurements of the mixing-induced CP violation parameters $\sin 2\phi_1$, ϕ_2 and ϕ_3, searches for a new source of CP violation in $B^0 \to \phi K^0_S$ and related decays, and the search for $D - \overline{D}$ mixing. The VTX also plays an important role in reducing the track reconstruction errors, which is beneficial in many analyses.

Although the performance of the current vertex detector at Belle is adequate for measurements of time dependent CP asymmetries, further improvements are highly desirable at SuperKEKB. We aim for a better impact parameter resolution, which will help reduce the background in rare B decays. This can be achieved primarily by locating the first layer of the VTX closer to the interaction region, and by introducing finer z segmentation. Better low-momentum tracking capability is also important. Efficient and robust track finding with the VTX alone is possible by introducing 5 or more layers of DSSDs. A large VTX, which provides precise three dimensional reconstruction of $K^0_S \to \pi^+\pi^-$, will also result in efficient vertex reconstruction for B mesons using only the K^0_S and an Interaction-Point (IP) constraint.

One of the major obstacles in achieving the better performance mentioned above is the larger background level at SuperKEKB. The high luminosity of the SuperKEKB machine and the proximity of the closest layers of the SVD to the interaction point require fine segmentation of the detector both time-wise and space-wise. According to the studies for SVD1 and SVD2, we need to keep the occupancy below 10% to guarantee the quality of the reconstructed vertices. Our present design goal is to achieve a reduction factor of 20 from the design of SVD2 or better. The expected annual radiation dose could reach 3 MRad at $R = 1$cm, thus the sensors for the innermost layers and readout electronics should be radiation hard. The readout deadtime should also be small at the target level-1 trigger rate of 10kHz. To meet all these requirements, we adopt an analog pipeline readout scheme for DSSDs with short strips that are readout by multi-layer flex circuitry. We choose the APV25, which has been developed for the CMS silicon tracker readout, as the best solution. Details of the APV25 are discussed in Section 3.2.3. The high background level also imposes a constraint on the usage of the drift chamber; by extrapolating the present background level, we conclude that we must extend the VTX to $r \simeq 15$ cm. While this requires some R&D on the mechanical structure, the larger volume and the resulting larger number of layers are beneficial for efficient low-momentum tracking and vertexing with K^0_S and IP as mentioned above.

Another important requirement exists for the effective thickness of the VTX. The impact parameter precision at a B-factory experiment, because of the low momenta of B decay products, is severely degraded by multiple scattering. In fact, the multiple scattering contribution dominates the impact parameter error, e.g. for the current SVD2 this corresponds to $\sigma_{ms}(z) = 28\mu\mathrm{m/p}\beta\sin^{5/2}\theta$ for $p < 1$GeV. Keeping the multiple scattering term small imposes severe constraints on the thickness of the detector's active material, the cooling medium and the support structure.

Figure 3.2 shows an overview of the VTX. Table 3.1 also shows the specifications of the DSSDs assumed in the default configuration. The inner wall of the beampipe is located at r = 1 cm. The VTX consists of 6 layers of sensors. In our default option, the two innermost layers are striplet detectors that are also readout with APV25's. More details of the striplet detectors are discussed in the next section. As an alternative and a future upgrade option, we also consider thin pixel detectors, which are discussed in Section 3.2.2. The 5th and the outermost layers

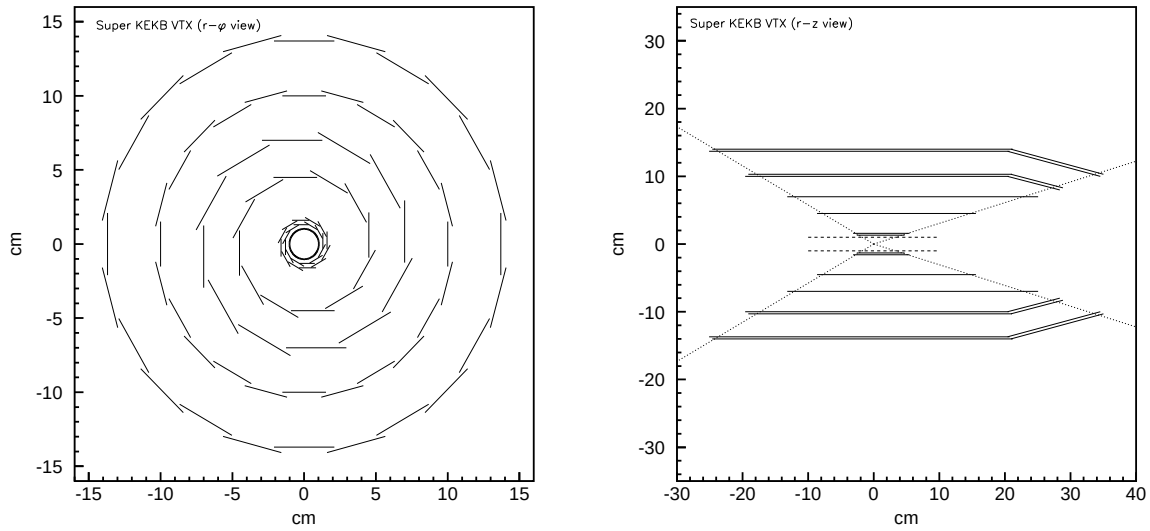

Figure 3.2: An overview of the SuperKEKB VTX detector.

consist of the barrel (layer 5a, 5b, 6a, 6b) and conical (s5a, s5b, s6a, s6b) parts since the structure with the barrel part alone requires very long ladders.

3.2.2 Innermost Layer

Striplet Detectors with UV-Coordinate

Considering the various technical difficulties in pixel detectors, the idea of DSSD sensors with short strips, hereafter *striplet sensors*, is becoming attractive, since the technology of DSSD sensors has been established for long time. As it is difficult to make the n-type strip width narrower than 50 μm, shortening of the strip length is practical in order to reduce the sensitive area per strip. However, if strips are merely cut into a few pieces, assembly with wire-bonds for the strips left at the middle of a sensor is not trivial. It is also difficult to supply bias voltages to strips that are placed away from the bias ring. In order to achieve a realistic striplet sensor, the parallelism of the strips should be discarded. If the strips are placed at an angle with respect to the DSSD outer shape, for example by 45 degrees, the strip length becomes ∼1.4*sensor width. In the case of the Super B vertex detector, the dimensions of the L1 sensors, which are placed r=13 mm from the interaction point, is about 8.5 mm x 71 mm (See previous section). One DSSD sensor covers the full angular region (15 to 150 degrees in the laboratory frame). Therefore, by introducing the striplet configuration with a 45-degrees slant angle, the strip size becomes 11 mm x 50 μm. Comparing this shape with normal strip shape, 71mm x 50 μm, we can expect to reduce the occupancy by a factor of 6.

In addition, by adopting a readout chip with a shaping time 4-5 times faster than SVD2 readout, the tolerance to background can be improved by factor of 20-30. A schematic drawing of the L1 striplet sensor is shown in Fig. 3.3. A magnified view of the right top corner is shown in Fig. 3.4. The cyan regions show the P-side readout strips while the black regions show the N-side strips. Due to the existence of readout pads and polysilicon bias resistors, the lengths of the shortest strips are 2 mm. Due to this limitation, triangular dead regions exist in the

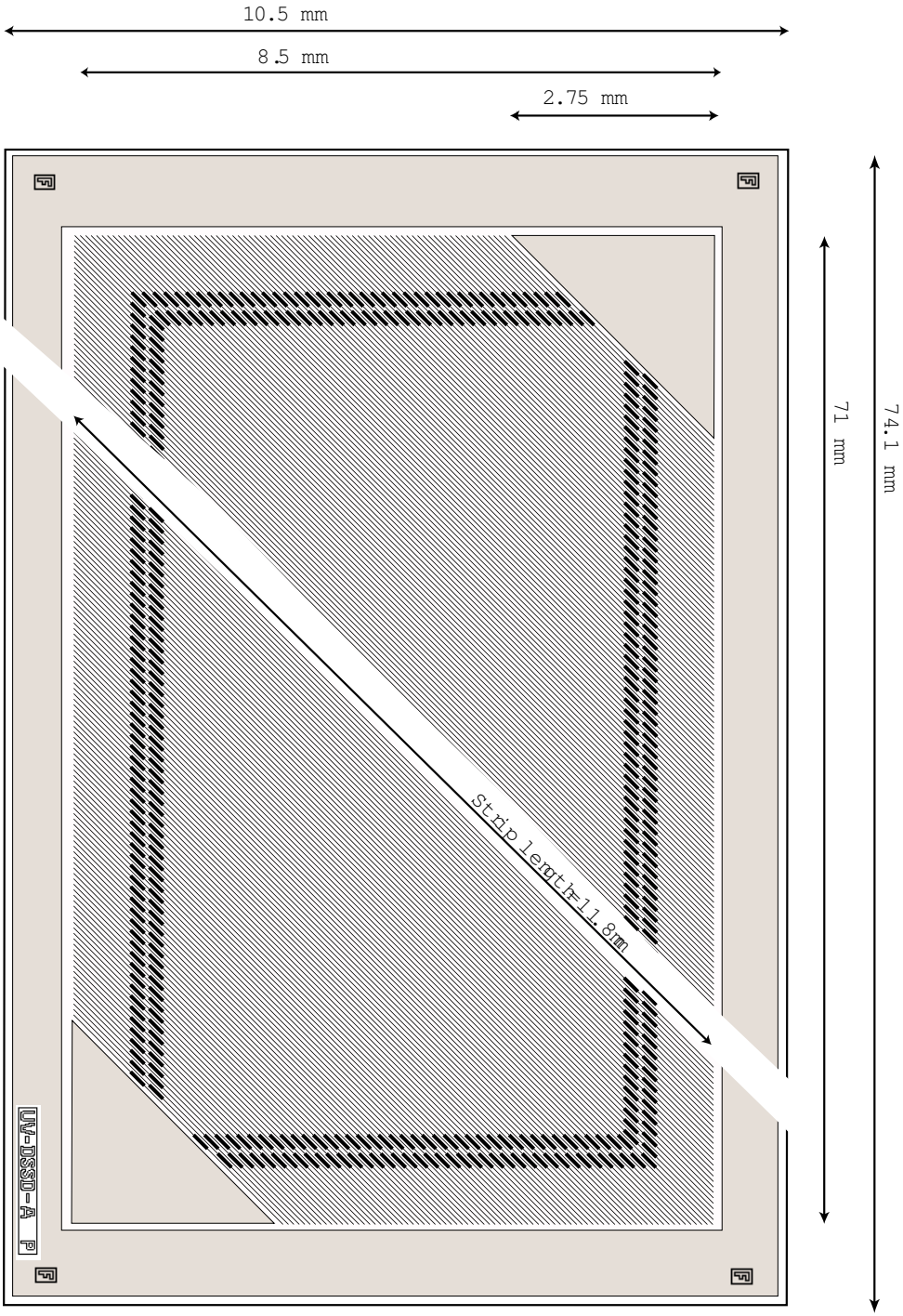

Figure 3.3: A schematic drawing of the L1 striplet sensor.

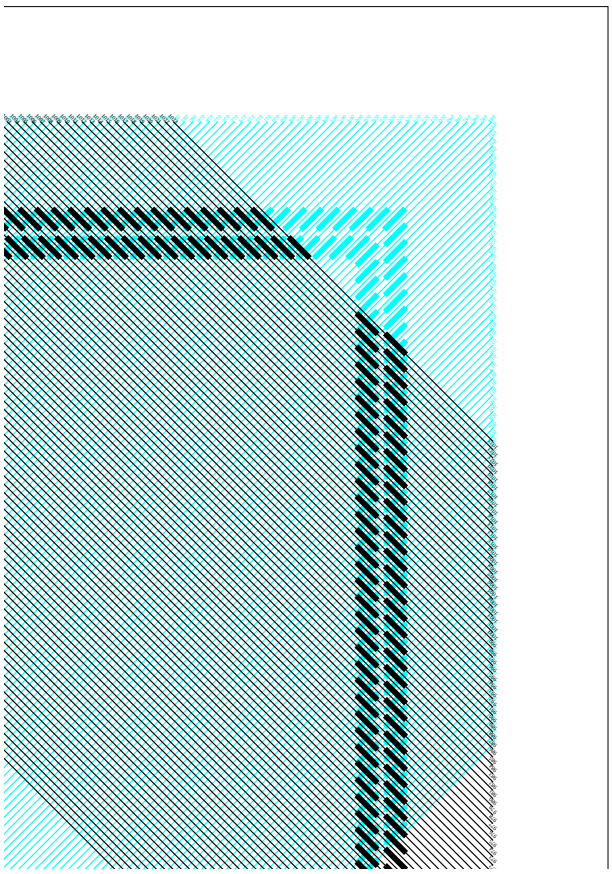

Figure 3.4: A magnified view of the L1 striplet sensor.

Layer	r (cm)	Effective Area (cm^2)	Number of DSSDs/ladder	Number of ladders
1	1.3	7.1×0.85	1	12
2	1.6	8.4×1.0	1	12
3	4.5	8.0×2.84	3	12
4	7.0	7.6×4.0	5	12
5a	10.0	8.0×2.84	5	12
5b	10.3	8.0×2.84	5	12
6a	13.7	7.6×4.0	6	12
6b	14.0	7.6×4.0	6	12
s5a	10.0/8.0	trapezoidal	1	12
s5b	10.3/8.3	trapezoidal	1	12
s6a	13.7/10.0	trapezoidal	2	12
s6b	14.0	trapezoidal	2	12

Table 3.1: Specification of DSSDs.

lower-left and upper-right corners. The strips on the opposite side are not shortened in the triangular region. In order to maintain the sensitivity to particle tracks, an implantation is made and a proper bias voltage is applied. Thus the particles entering this region will still have information from one side. There are other merits in the striplet configuration. 1) The P-side and N-side strips cover the same area and thus optimization to the occupancy can be done together. The hit positions are determined from both the P- and N- side hit positions. In order to treat single-side hit points, which have a different error matrix, the track fitting program will have to be modified. 2) The width and length of the sensor can be arbitrarily chosen.

By reducing the sensitive area of each channel, the total number of readout channels increases. In case of the L1 sensors, the signal density is about 6 times larger than that for the SVD2 sensors. The development of a high-density readout by using multi-layer kapton film will be necessary for the readout of the striplet sensors.

Flexible printed circuit (FLEX) is useful to readout the charge signal from the silicon strip sensor. FLEX consists of a thin Kapton film and a Cu printed circuit pattern. Using FLEX, we succeeded in building the Belle's SVD2 with good noise performance and a high yield of active channels.

We need a long FLEX to readout the signal from the outer silicon strip detector. The strip pitch should be around $50\mu m$ and the length longer than 30cm.

If we employ the striplet option for the innermost layer, we need a more precise pitch FLEX due to its aspect ratio. We need to develop a FLEX circuit, whose strip pitch is less than 40 μm and strip length is about 100mm. Figure 3.5 shows the design of the prototype FLEX for the striplet sensor.

For the hybrid Pixel option, we also need a feasible digital bus, made of FLEX, to implement the front-end LSI for the Pixel sensor.

Options for the 2nd Upgrade

As explained in the previous section, an occupancy below 10% could be achieved with the ordinary strip detector if the strip length is reduced to $\sim$ 8mm in both z and $R\phi$ directions and the sensor is readout with an analog pipeline. While this scenario provides a reasonable margin against unexpectedly large background levels, it is important to consider further reduction of the occupancy. The pixel sensors readout with very fast dedicated electronics can reduce the

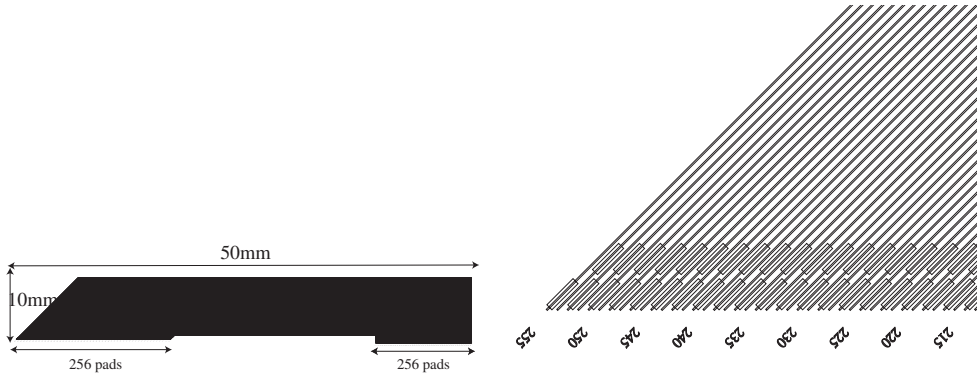

Figure 3.5: The design of the prototype FLEX for the striplet sensor.

occupancy by an order of magnitude. There are three available technologies for this purpose.

- Hybrid pixels.
  All the LHC experiments (ATLAS,CMS and ALICE) will use variants of hybrid pixels and thus it is quite a mature technique. The pixel size is constrained by the front-end electronics density factor and the interconnection technology, it ranges from 150×150 μm^2 to 50×450 μm^2. The detector and the readout are radiation hard up to MRads. The dissipated heat is typically $\sim 40\mu$W/pixel, therefore advanced cooling techniques are needed (not gas cooling), amounting to a thickness of each layer in excess of $1\%X_0$ (including the sensor thickness of 250μm and the front-end chip thickness of 150μm).

- CCD pixel detector.
  The success of the SLD experiment has proven that this technology is mature enough to be used in collider experiments. However, the readout speed and the radiation tolerance are the issues to be addressed, in order to adopt this technology at the high-luminosity B factory. There are some promising advances in R&D, but most probably this technology will not be mature enough before 2007.

- Monolithic Active Pixel Sensor (MAPS).
  The technology is potentially very suitable for low-energy high-luminosity colliders, however it is still in the R&D phase. The radiation damage resistance of the detector is not fully understood yet. Currently the maximum electromagnetic radiation dose is only 200kRad. It is difficult to foresee the advances that will achieve radiation hardness in the MRad region, but likely this will not happen before 2006. The obtained real size detector thickness is 100μm, R&D is continuing to thin the detector down to 30μm. The typical pixel size is 20×20, but the desired pixel size of 50 μm $\times$ 100 μm can be realized. The amplification and readout circuitry of the MAPS is integrated at the pixel, the signal transfer and processing electronics is on the chip edge. Currently, with no zero suppression, only 5k pixels can be readout in $\sim 100\mu$sec, therefore a massively parallel column readout is needed to readout the detector. Gas cooling should be adequate, if no intensive data processing is done on the chip.

3.2.3 Readout Electronics

We survey the DSSD readout VLSIs that are available now or will be available by 2006. The options are listed in Table 3.2.3. We choose APV25 as the best candidate for SuperKEKB.

Table 3.2: Pipeline chips for DSSD readout.

Experiment	chip	process	pipeline	principle
CMS	APV25	IBM 0.25 μm	192 cells	analogue
LHCb	BEETLE	0.25 μm	160 cells	analogue
ATLAS	ABCD		132 cells	binary
CDF/D0(run2)	SVX4	IBM 0.25 μm	47 cells	FE/BE architecture, double-correlated sampling, periodic reset, digital
Belle	VA1TA	AMS 0.35 μm	No	continuous shaping, analogue
BaBar	AtoM	Honeywell	Yes	time-over-threshold
CLEO III	FE/BE	Honeywell	No	on-hybrid ADC, digital
ZEUS	Helix	AMS (non-radhard)	128 cells	analogue

There are several reasons. First, the design is already finalized and mass production is on-going. It has sufficient radiation hardness up to 30 Mrad. The pipeline length is long enough to wait for the level-1 trigger; it is more than 3 μs for a clock frequency of 40 MHz. The continuous shaping scheme is also preferable at SuperKEKB where the bunch crossing interval is only 2 ns. Figure 3.6 shows the architecture of the APV25.

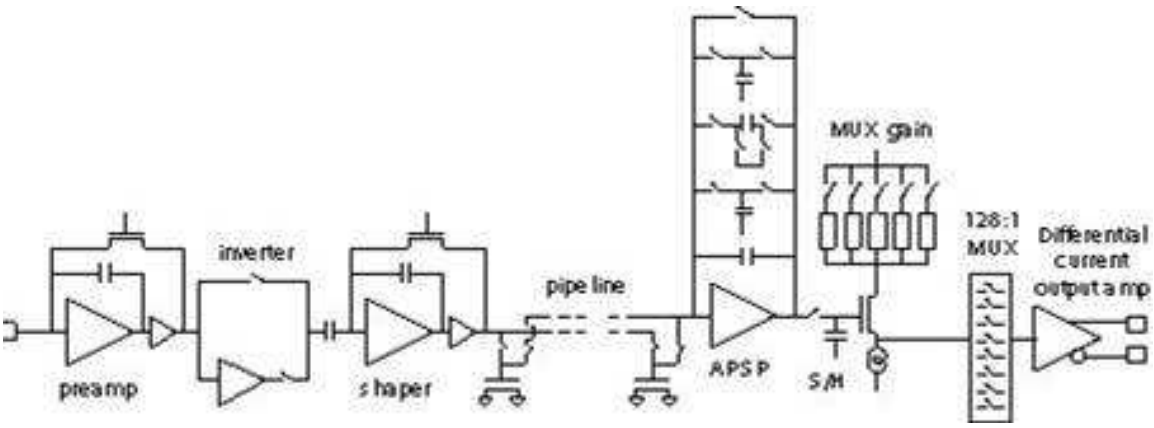

Figure 3.6: Architecture of the APV25.

Although the APV25 has many good features that are suitable for use at SuperKEKB, it is not trivial to know whether it can be used without any modification.

At CMS, a beam crossing occurs every 25 ns. With a 40MHz clock and with a peaking time (Tp) of 50 ns, pipelines can always be synchronous to the collisions. However, the time between beam crossings at SuperKEKB is 2 ns, which means that APV25 should be operational practically with DC beams. It is therefore unavoidable that the capture timing has some jitter with relative to the peak position. In order to reduce this effect, one solution is to use a longer peaking time. We have confirmed stable operation up to Tp = 240 ns without degradation in S/N, where the noise is measured without any capacitive load. As mentioned above, the total

S/N with DSSDs will be better for the longer peaking time. Figure 3.7 shows an example of the shaper output for Tp = 50 (left) and 100 ns (right). One drawback of the longer peaking time

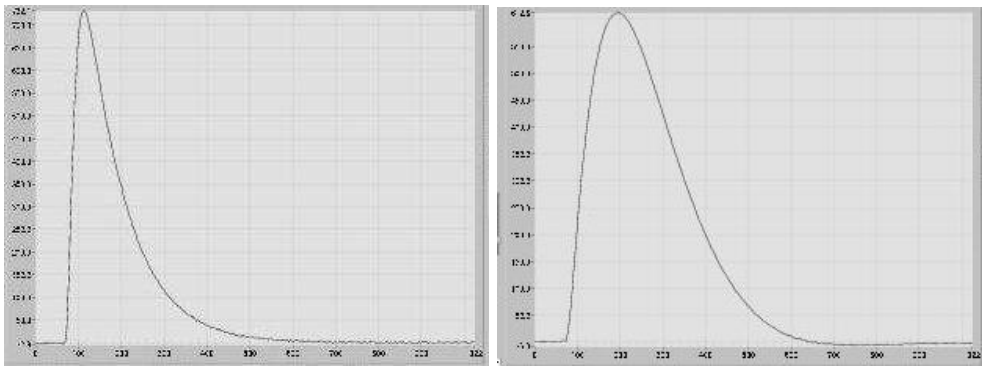

Figure 3.7: APV25 shaper output with Tp = 50 ns (left) and 100 ns (right).

is a larger occupancy. The best peaking time should therefore be chosen under the actual beam condition. At SuperKEKB, we will use a readout clock frequency of 42.33 MHz. We tested that this frequency does not cause any problem in the readout sequence.

Table 3.3 shows the expected signal-to-noise ratios for two types of DSSDs used in the barrel part. In the table, the performance of APV25 is assumed to be ENC = 270 + 38/pF, which was

Layer	Effective Area (cm^2)	Side	Capacitance (pF)	S/N (S=20000e-)
3, 5a, 5b	8.0×2.84	p (z)	4.5	45
		n ($r\phi$)	22.7	18
4, 6a, 6b	7.6×4.0	p (z)	6.0	40
		n ($r\phi$)	19.2	20

Table 3.3: Expected signal-to-noise ratios for DSSDs readout with the APV25.

measured by the CMS group with Tp = 50 ns. We conclude that we need to readout each DSSD with flex circuitry separately to ensure good (> 15) S/N. Note that the actual performance should be better when we use Tp = 100 ns. However, we do not take this improvement into account since we have no measurement yet. We also ignore the possible small degradation from the jitter effect mentioned above.

All these considerations indicate that APV25 can be used without modification at SuperKEKB. We have also had detailed discussions with the APV25 developers and found no obstacles.

As for the backend electronics, we consider the two options shown in Fig. 3.8. The first option (Fig. 3.8 left) is to use FINESSE as a simple relay to the COPPER event FIFOs. An alternative option (Fig. 3.8 right) is to use dedicated COPPER modules. An advantage of the first option is that technologies that have already been developed for the CMS readout can be maximally shared.

There is a strong demand for a fast trigger from the VTX that can be used either in the level-1 or level-2 trigger system. It is possible to generate such trigger information from APV25 data using programmable logic devices. Since the maximum latency for level-1 is constrained

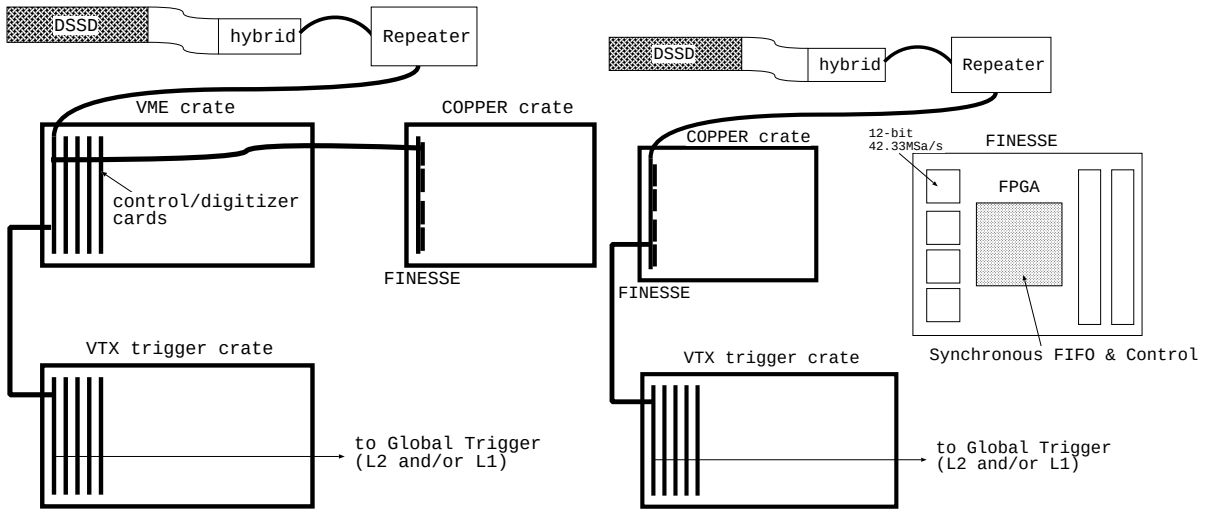

Figure 3.8: Schematic diagrams of two possible schemes for the VTX readout system.

by the pipeline length of the FINESSE/COPPER system, we need to estimate the VTX trigger latency to judge if it is suitable for the level-1 trigger system.

3.2.4 Performance

We analytically calculated impact parameter resolutions using TRACKERR for various configurations and detector options. In the calculations, we test two options for the innermost two layers; the striplet and the hybrid pixel options. The configuration of the outer detector is kept the same. Figure 3.9 shows the impact parameter resolutions with the striplet option, where the effective thickness for each layer is assumed to be equal to that of the SVD2 innermost layer. The resolutions are better than those for SVD2.

In the hybrid pixel option, the pixel size is usually limited by the bump bonding capability. We here consider two cases. The first option is square (150 μ m $\times$ 150 μ m) pixels as in the CMS pixel sensors. We find that the resolution in this case is not satisfactory. The other option is rectangular (50 μ m $\times$ 400 μ m) pixels like the Alice pixel sensors. To have good resolutions both in the z and $r\phi$ directions with the former pixel size, we consider the case of the innermost pixel layer located at r = 13 mm with 50 μm for the z coordinate, and the 2nd pixel layer located at r = 15 mm with 50 μm for the $r\phi$ coordinate. Figure 3.10 shows the resulting impact parameter resolutions. Here each pixel sensor is assumed to be thinned to 250μm. We also assume an LSI thickness of 150μm and an additional support structure equivalent to 300 μm Si, which is shared by two pixel layers. In this case, the resolutions are comparable to those obtained with SVD2.

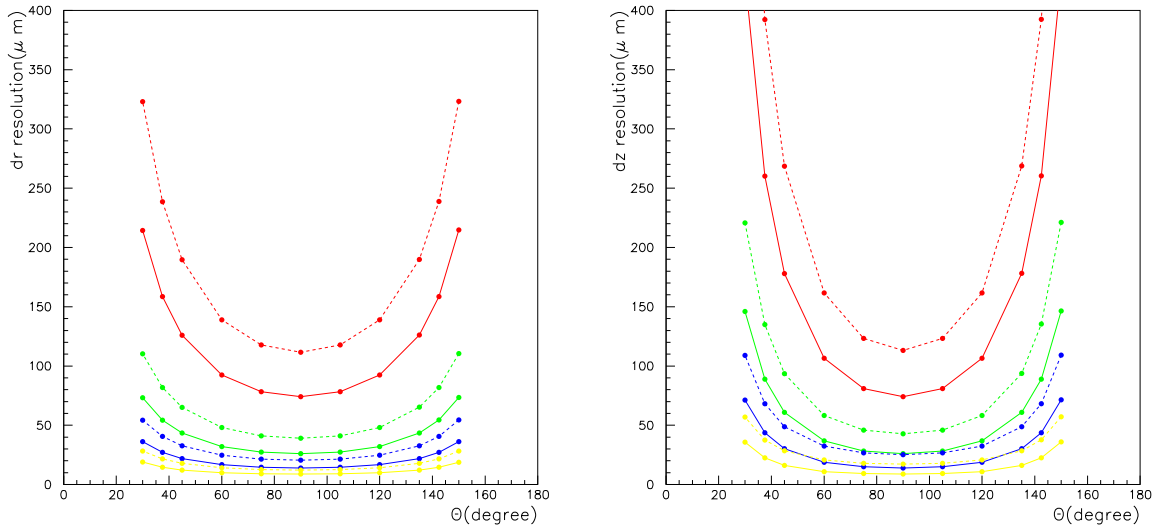

Figure 3.9: The impact parameter resolutions in the $r\phi$ and z directions with the striplet option. The dotted line shows the IP resolution of SVD2. Each color shows the particle momentum (Yellow:0.2, Blue:0.5, Green:1.0 and Red:2.0 GeV/c).

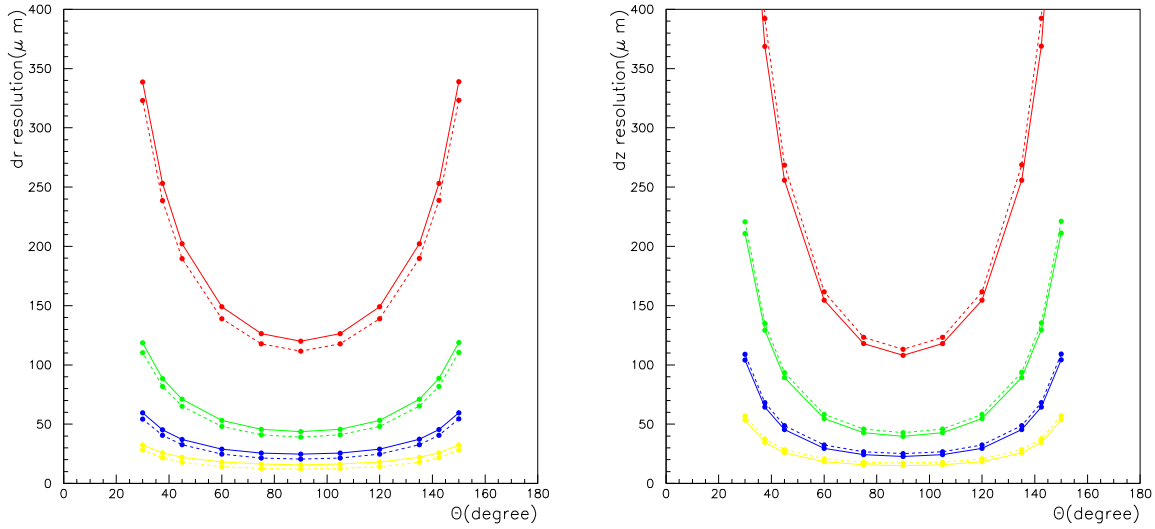

Figure 3.10: Impact parameter resolutions in the $r\phi$ and z directions with the thickness of 300 μm Si equivalent. The dotted line shows the IP resolution of SVD2 case. Color notation of momentum is same as Figure 3.9.

3.3 Cetral Tracker

The most critical issue in choosing the tracking device for the experiment at Super-KEKB is whether the normal gas wire chamber works as a central tracker, even in higher beam background condition. A larger wire chamber can be built with the established technology, which covers a large solid angle and provides good performance in both momentum and dE/dx measurements. The simulation result in higher background is described in the section**. In this section, a proposed gas wire chamber as a CDC is reported.

The basic design of a new CDC is same as the present CDC, which has been working well as described in the section**. The key parameters are shown in Table 3.4. The outer radius should be determined by a size of a new particle identification device. The inner radius can be selected in any radius. Considering the hit rate in the present CDC(Fig. 1.20) and a cost of the silicon vertex device, the boundary in 15 cm radius is tentatively selected. The new gas mixture with a fast drift velocity is preferable to reduce the maximum drift time. One candidate was a pure methane described in EoI, which has faster drift velocity without a magnetic field. Unfortunately, a recent simulation study indicates the maximum drift time is similar as the present gas due to a larger Lorentz angle under 1.5 Tesla magnetic filed. Also, higher voltage is required to obtain the same gas gain. So far, the present gas mixture is the best candidate for the new CDC. Then, there are no reasons to change material and radius for both sense and field wires.

The wire configuration is shown in Table 3.5. There are 6 layers in each super-layers. Larger number(6) of layers in the stereo super-layer helps to reconstruct three dimensional tracks as comparing the present one(4). Higher hit rate near walls is observed in the present CDC since background photons convert to electrons in the walls. Degradation of the performance may be expected for inner and outer most layers due to higher rate. Two more layers are added in inner and outer super-layers for a safety.

We could construct the chamber with 5 mm cell size as demonstrated in the present upgrade. It is not necessary to make cell size such small for outer layers. Because the hit rate decreases as a function of the radius as shown in Fig. 1.20. In order to reduce a number of wires, the cell size should be optimized, considering a hit rate. Table 3.5 shows just one example. In this case, the number of total wires reachs 60000. A deformation of the endplate becomes larger due to larger total tension. Two ideas are being considered to reduce the deformation. The first one is to change a shape of curved endplates. The new endplates shown in Fig. 3.11 can reduce the deformation by about 30 %. Another one is to string the filed wires with a lower wire tension. The tension in the present CDC was selected to keep a gravitational sag similar for both wires. This condition may be relaxed without a degradation of the special resolution.

There are no critical issues to construct a new larger CDC. But, several technical points should be re-considered. The first one is the arrangement of the pre-amps near the endplate. It is better to minimize a cable length between the pre-amp and the feedthrough in order to reduce a cross-talk. Also, an accessibility to the feedthrough after mounting pre-amps should be taken into account. The second one is an alignment of 6 endplates and all wire positions. In principle, the alignment can be done using cosmic ray events without the magnetic field after the installation. But, we are considering a calibration run before the installation using a laser system or reference chambers, in order to obtain alignment constants, easily.

The readout electronics should be upgraded to accommodate the higher hit rate. It is necessary to develop the pipeline readout system, which is described in the DAQ section. The pre-amp and receiver-amp themselves are still useful for the higher rate. Now, we are considering three options to upgrade the CDC electronics. The first option is just to replace FASTBUS TDC

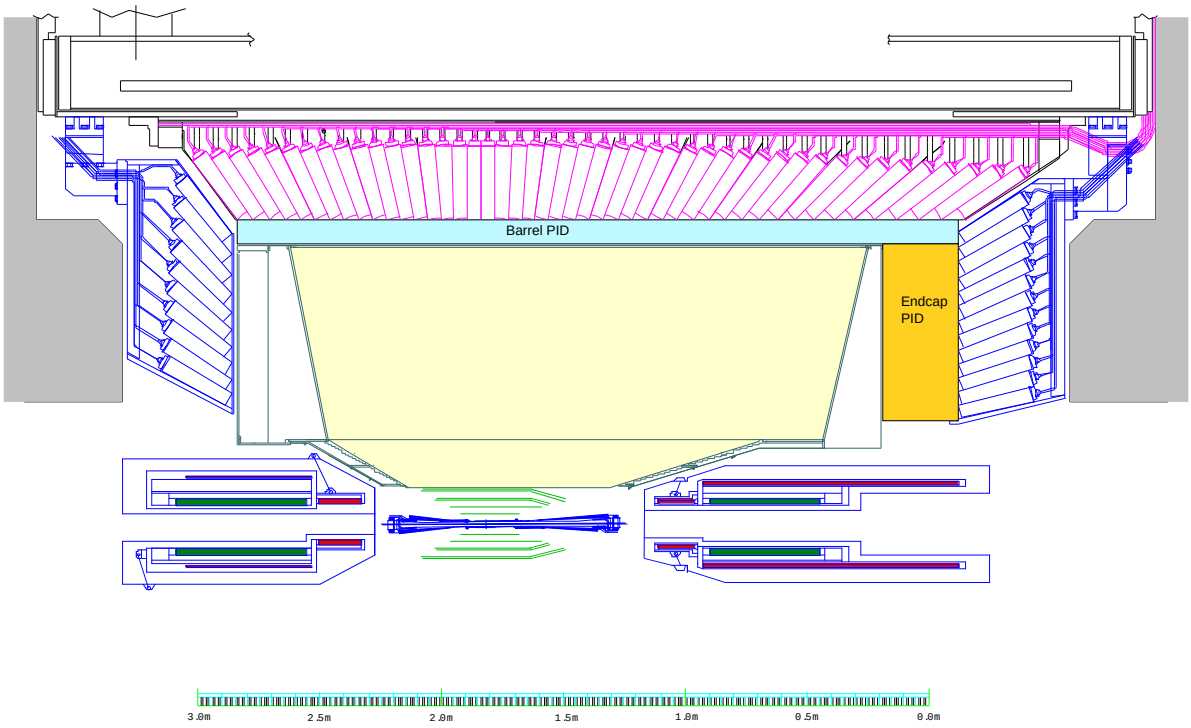

Figure 3.11: A concept for the upgraded CDC structure.

with a new pipelined TDC. This is cheapest option and requires the least additional manpower. The performance for both timing and dE/dx measurements was established for low hit rate up to at least 50 kHz in the present CDC. The second option is to use a pipelined TDC and A 20 MHz flash ADC. In this case, the number of the readout channels becomes doubles. The last option is to develop a 100 MHz flash ADC with at least the 9 bit dynamic range. In this case, the ADC data should be converted to timing and dE/dx on the board to reduce the amount of data transferred.

We have a plan to carry out a beam test in the near future in order to check the limitations of the current shaper/QT system and the performance of the new scheme with Flash ADCs.

Table 3.4: Main parameters of the new CDC

Radius of inner boundary(mm)	150
Radius of outer boundary(mm)	1150
Radius of the inner most sense wire(mm)	172
Radius of the outer most sense wire	1120
Number of layers	58
Total number of sense wires	15104
Effective radius of dE/dx measurement(mm)	978

Table 3.5: Wire configuration for the CDC in the Super KEKB upgrade

Super-layer	Radius(mm)	axial or stereo	number of layers	number of cells per layer
1	172 - 242	A	8	160
2	266 - 346	U	6	160
3	368 - 448	A	6	192
4	464 - 544	V	6	224
5	562 - 652	A	6	256
6	670 - 760	U	6	288
7	778 - 868	A	6	320
8	886 - 976	V	6	352
9	994 -1120	A	8	388

3.4 Particle Identifier

3.4.1 Overview

Particle identification (PID), especially K/π separation, plays a crucial role in B-factory experiments. This situation will remain unchanged at the Super-KEKB/Belle experiment, as discussed earlier.

We would like to upgrade the Belle PID system in order to improve the performance and meet the requirements of Super-KEKB/Belle. The upgraded system should remove the problems of the present system, described in Section 1.4.3, and improve our physics reach, as discussed in Section 2.5. The neccessity for improvement also arises from consideration of the increasing background. Radiation hardness of the detector components also has to be carefully examined.

To improve the particle identification performance, it is desirable to upgrade to a detector with ring imaging Cherenkov counters. We propose the following two types of new detectors for the upgrade of the Belle PID system;

- *Time Of Propagation (TOP) counter* for the barrel PID.
- *Proximity Focusing Aerogel RICH* for the endcap PID.

We have carried out R&D for these two detectors in the past few years. In this section, the concept, design, expected performance and R&D status of these proposed detectors are presented. If these detectors are realized, they will completely replace the present Belle PID detectors, the ACC and TOF.

While we propose these two detectors as the baseline upgrade options, we also consider options for the barrel part, based on the time-of-flight technique;

- *Tile TOF counter* aiming at $10 \sim 20$ps timing resolution, utilizing relatively small Cherenkov radiators.
- *50ps TOF counter* as upgrade of the present Belle-TOF with finer segmentation.

Idea for these backup options and the R&D status are also described in this section. For the TOF options, we have to consider their usage in combination with the present Belle-ACC system in order to cover the high momentum region.

3.4.2 TOP counter (barrel)

Introduction

The TOP counter [11] utilizes total internal reflection of Cherenkov photons produced in a quartz bar. Figure 3.12 shows the detector principle of the TOP counter. When a charged particle passes through the quartz radiator bar, Cherenkov photons are emitted in a conical direction defined by the emission angle θ_c, and transported to the end of the bar by means of total internal reflection. In the case of the DIRC counter, used in the BaBar experiment [12], a ring image of the transported Cherenkov photons is magnified and projected onto a PMT array in a large stand-off. The Cherenkov emission angle θ_c is then calculated from the two-dimensional hit coordinates (X-Y) of each photon. On the other hand, in the case of the TOP counter, the two-dimensional information of the ring image is represented by the TOP (time of propagation) and the horizontal emission angle (Φ) of the Cherenkov photons,

$$TOP(\Phi;\theta_C) = \left(\frac{L}{v_g(\lambda)}\right) \times \frac{1}{q_z(\Phi,\theta_c)}, \tag{3.1}$$

where L is the distance that the light travels along the bar, $v_g(\lambda)$ is the group velocity of light in the quartz medium, and q_z is z-component of unit velocity vector. Since the time-of-flight (TOF) difference between two particle species from the interaction point to the detector enhances their TOP difference in most cases, TOF is appended to TOP. For instance, when a 3 GeV/c K and π meson are incident on the quartz bar, $\Delta TOP \sim 75$ ps at $L = 1$ m, and $\Delta TOF \sim 50$ ps for a flight length of 1 m. Therefore, with enough photostatistics ($N_{pe} > 20$), the time measurement for each arriving photon with ~ 100 ps precision provides significant K/π separation.

In principle, the time measurement uncertainty for each detected photon (σ_{time}) arises from three major sources; 1) chromatic dispersion in photon propagation inside the quartz bar (σ_{chro}), 2) imperfectness in polishing the quartz bar (σ_{polish}), and 3) transit time spread (TTS) of the photodetector (σ_{TTS}). The chromatic dispersion arises from wavelength dependence of the group velocity of photons propagating inside the quartz bar ($v_g(\lambda)$), therefore, σ_{chro} depends on the bandwidth in the photodetection and on the propagation distance (L). For instance, when a typical bialkali photocathode ($\lambda = 300 \sim 400$ nm) is used, σ_{chro} is estimated to be about 100 ps at $L = 1$ m.

Therefore, as in the case of the DIRC counter, good polishing accuracy of the quartz bar is required so that σ_{polish} is small compared to σ_{chro}. The TOP counter also requires a position sensitive photodetector with superior TTS (< 100 ps) for single photons. These are the two big challenges in the development of the TOP counter. The details of the TOP counter principle and status of our earlier development can be found in [11].

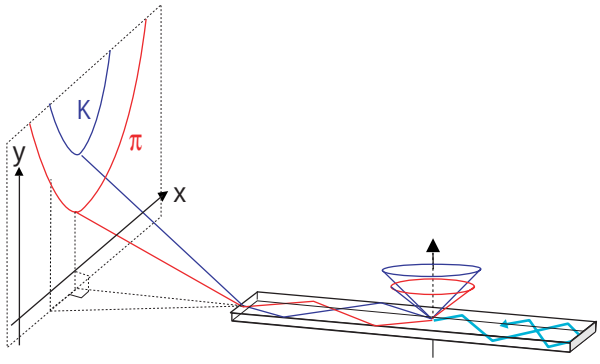

Figure 3.12: Principle of the TOP counter.

"Bar-TOP" counter

Figure 3.13 shows a schematic drawing of a TOP counter module, which is proposed for application to Super-KEKB/Belle. The TOP module presented here is referred to as "Bar-TOP", which is different and simplified from that in our earlier development described in [11]. It is composed of a quartz bar radiator and a photodetector array. The radiator is a well polished synthetic fused silica bar, as will be discussed later in Section 3.4.2. It is 2 cm thick and 255 cm long. The width is $20 \sim 40$ cm in our present consideration, and is a design parameter to be

optimized taking account of the PID performance, feasibility in production and background immunity. The photodetector array is attached at the end of the bar to measure the horizontal position (X) and time of each arriving Cherenkov photons. We presently consider attaching an array of multi-anode PMT's based on micro-channel-plates (MCP-PMT), each having 4 linear anodes with 5 mm pitch. More details of the photodetector will be described in Section 3.4.2.

Figure 3.14 shows the relation between the X position and TOP for each detected photon. Because the X-TOP image is flipped at the side edge for several times, their relation cannot be uniquely extracted for each hit. However, enlargement of the quartz-bar width to wider than 20 cm will solve this entangled relation, as illustrated in Figure 3.14.

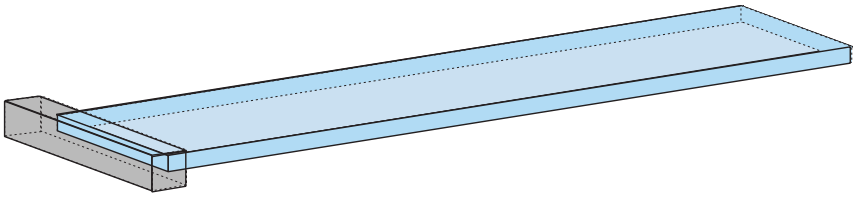

Figure 3.13: Schematic drawing of the Bar-TOP counter.

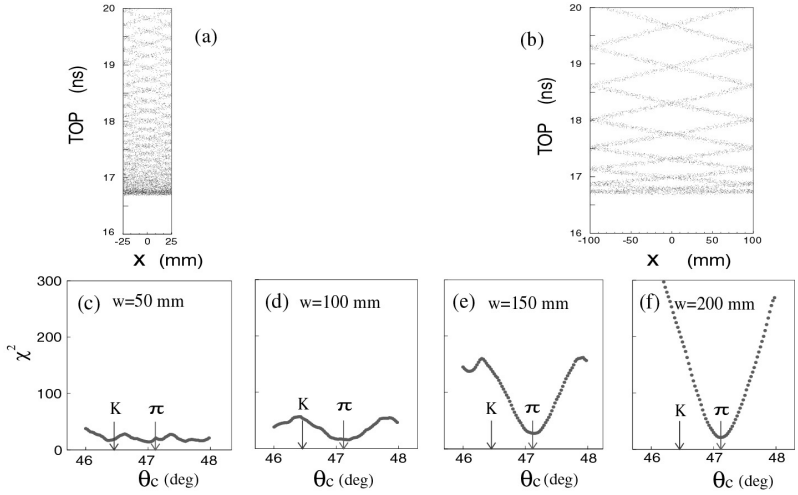

Figure 3.14: Principle of the Bar-TOP counter. X-position-vs-TOP relation and π/K separation in terms of χ^2 are shown at (a) and (c), respectively, for a 50 mm-wide bar and (b) and (d) for a 200 mm-wide bar. For illustration purposes, the effects of chromaticity and TTS are not included in (a) and (b), and that of TTS is not considered in (c) and (d).

Detector Configuration in Belle

In the Belle detector, the "Bar-TOP" counter modules would be arranged in a barrel-shape array. Such an array would easily fit into the barrel part of the Belle detector. Figure 3.15 shows our preliminary design for the array, where we assume that the bar width is 40 cm. In this case, the array is segmented into 18 modules, with the innermost surface located at a radial distance of 118 cm from IP. The gap between the two adjacent bars is about 1 cm, giving the dead space of approximately 3%. The required radial space is 10 cm, from r =115 to 125 cm,

including the bar thickness (2 cm), sagitta (1 cm), mechanical support structure and margin for installation. The quartz bar expands in the beam direction for 255 cm, from $z = -72.5$ to 182.5 cm, to cover the polar angular region from 33.3° to 148.9°. The number of readout channels will be 60 channels per module and 1080 channels in total, if a 40 cm wide bar is used. The 2cm thick quartz bar corresponds to 16% of a radiation length.

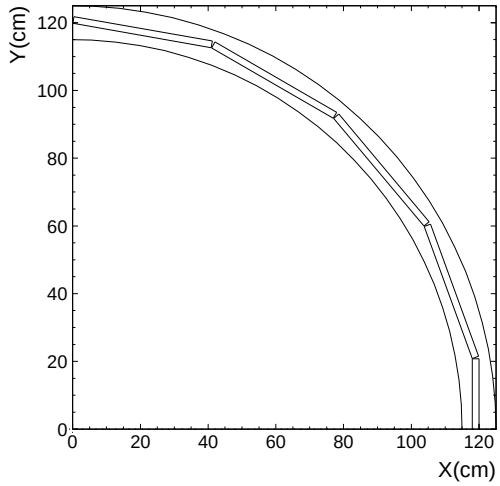

Figure 3.15: Configuration of the TOP module array in the barrel part of Belle.

Principle Confirmation with Prototype

In order to confirm the principle of the "Bar-TOP" counter, we have constructed a prototype module, as shown in Figure 3.16. The size of the quartz bar is 100 cm (length) × 20 cm (width) × 2 cm (thickness). Photodetection is made by an array of multi-anode PMT's, HPK R5900-00-L16, which has 16 channel linear anodes with 1 mm spacing. The PMT is single photon sensitive and its typical TTS is about 75 ps (σ). Figure 3.17 shows the ring image obtained with 3 GeV/c pion beams incident at the position of $L = 10$ cm. A clear X-TOP ring image is obtained.

Quartz radiator

For the quartz radiator material, synthetic fused silica would be the most appropriate choice because of the long transmission length, good polishability and radiation hardness. Synthetic fused silica is available, for example, from Shin-etsu Quartz Company; their product 'SUPRASIL-P30' has a refractive index of $n = 1.47$ at a wavelength (λ) of 390 nm and a bulk transmittance of 90% at $\lambda = 250$ nm. As in the case of the DIRC counter, its surface has to be polished with a great accuracy to preserve the X-TOP relation after several tens of internal reflections. We have tested quartz bars polished by different companies, and so far obtained satisfactory results with those polished by Okamoto Kogaku Co. in Yokohama, Japan. Table 3.6 compares the polishing accuracy by two companies (bar#2 is polished by Okamoto Kogaku Co.) and the TOP resolution at $L = 2$ m, measured in the beam test of our prototype counters [1]. Figure 3.18 shows the

[1] These measurements were carried out with prototype TOP counters with a focusing mirror, a so-called "Butterfly-TOP".

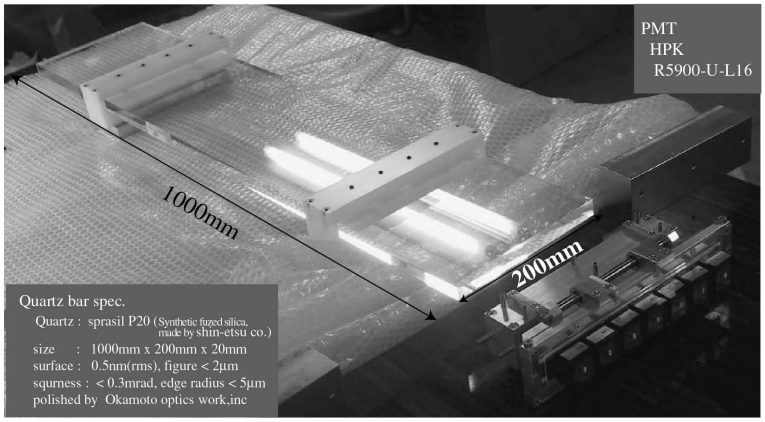

Figure 3.16: Photograph of the "Bar-TOP" prototype counter.

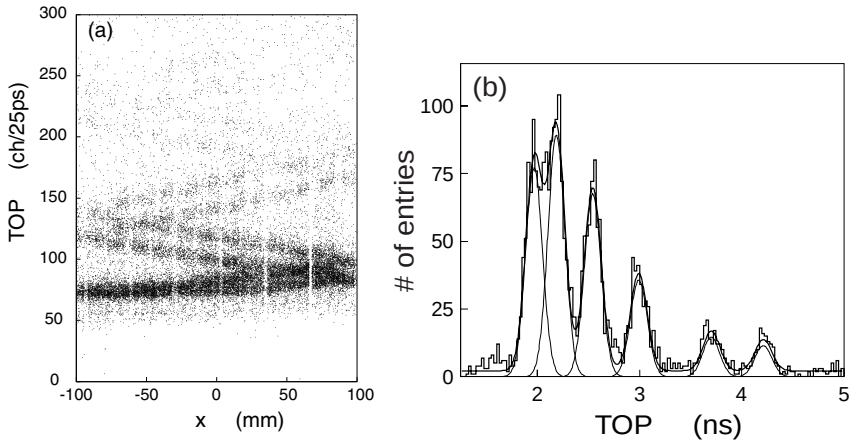

Figure 3.17: Beamtest result for the prototype counter.

measured timing resolution as a function of the propagation distance (L). The measured timing resolution for the quartz bar #2 is close to the limit due to the chromatic dispersion. Therefore, the contribution from the polishing accuracy to the TOP uncertainty is small enough.

Photodetection

The TOP counter requires photodetectors, which can detect a single photon with; 1) good timing resolution (< 100 ps), 2) position resolution (~ 5 mm in one direction), 3) high quantum efficiency ($> 20\%$ at peak), 4) large effective area ($> 70\%$ per package) and 5) magnetic field immunity (up to 1.5T). Since none of photodetectors on the market satisfy these requirements, it is necessary to develop new devices.

For this purpose, we have produced multi-anode PMT's with different dynode technologies in collaboration with Hamamatsu Photonics Co. [13]; 1) a metal-dynode PMT with 16 linear anodes (L16, R5900-00-L16), 2) a fine-mesh PMT with 24 linear anodes (L24, R6135MOD/A-L24X) and 3) a micro-channel-plate PMT (MCP-PMT) with 4 linear anodes (SL10), and investigated

Table 3.6: Comparison of polishing accuracy by two companies and the measured TOP resolution at $L = 2\,\mathrm{m}$.

	polish	figure	squareness	edge radius	time resolution
Bar #1 (old)	2 nm	5 μm	2 mrad	50 μm	300 ps
Bar #2 (new)	0.5 nm	0.6 μm	0.6 mrad	5 μm	150 ps

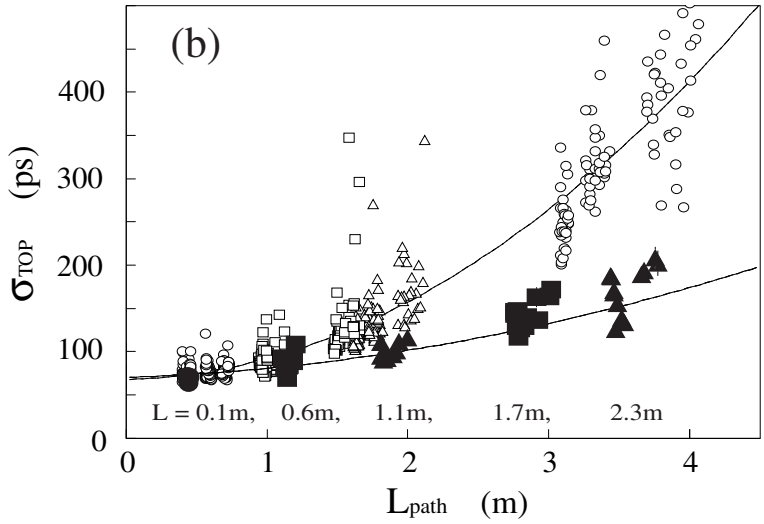

Figure 3.18: Single photon resolution as a function of the propagation distance L in beam tests of prototype counters.

their characteristics. Table 3.7 compares the basic performance of these devices. Among them, the MCP-PMT is found to be the best candidate for the TOP counter because of its superior timing resolution, about 35 ps, and immunity to magnetic fields.

Figure 3.19 shows a photograph and a schematic drawing of the 1st prototype of a 4-linear-anode MCP-PMT. The PMT has an effective area of 22 mm $\times$ 22 mm in 27 mm $\times$ 27 mm package, two stages of micro-channel-plates for electron amplification. Figure 3.20 shows the measured gain and TTS as a function of the magnetic field strength. We have confirmed that this MCP-PMT satisfies the critical performance requirements; the gain higher than 10^6 and TTS of about 35 ps (σ) even inside the magnetic field of 1.5T. At present, some remaining issues,

Table 3.7: Comparison of PMT's with different dynodes; G(0T) stands for gain without the magnetic field, G(1.5T)/G(0T) gain reduction at 1.5T, TTS(0T/1.5T) is the TTS (σ) with the 0T/1.5T magnetic field.

Type	Dynode	Anode (pitch)	G(0T)	G(1.5T)/G(0T)	TTS (0T/1.5T)
L16	metal dynode	16 (1mm)	$\sim 10^7$	—	75ps / —
L24	fine-mesh	24 (1mm)	$\sim 10^7$	10^{-2}	100ps / 150ps
SL10	MCP	4 (5mm)	$\sim 10^6$	0.5	35ps / 35ps

such as aging and high rate capability are being investigated. We are also trying modification of designs to reduce cross talk and to further improve the gain.

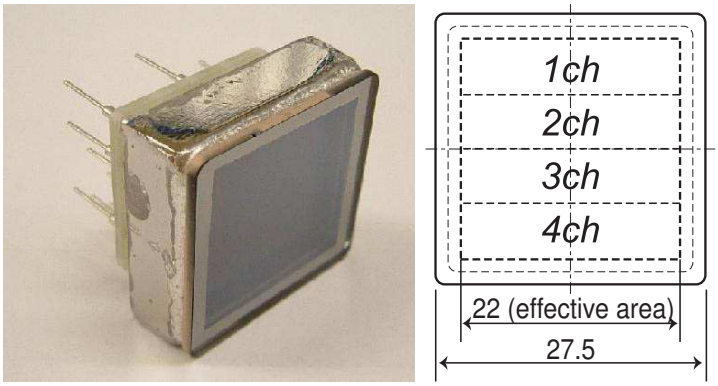

Figure 3.19: Photograph of the 1st prototype and structure of the 4-linear-anode MCP-PMT (SL10) under development.

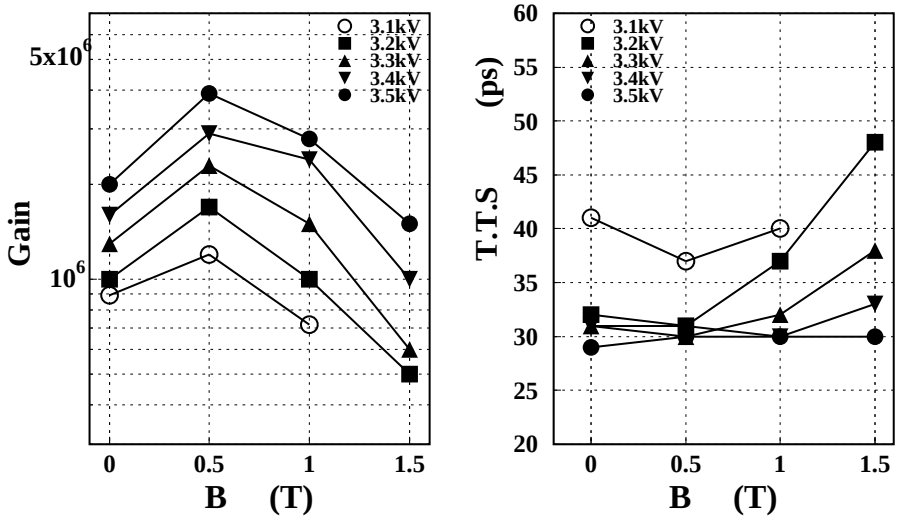

Figure 3.20: Performance of the 4-linear-anode MCP-PMT (SL10).

Expected Performance

In an approximate form, the separation power (S) between two particle species using the TOP counter is expressed as,

$$S = \frac{\Delta T}{\sigma_{time}} \times \sqrt{N_{pe}} = \frac{\Delta TOP + \Delta TOF}{\sigma_{time}} \times \sqrt{N_{pe}} \tag{3.2}$$

Here, ΔT denotes the difference between the two particle species for the sum of TOP and TOF, N_{pe} the average number of detected photons per track and σ_{time} the single photon resolution. All of these quantities are strongly correlated with the incident position and angle of incoming

particles. Therefore, PID performance depends on the polar angle of the track, when the TOP counter is installed in the barrel part of the Belle detector.

We have performed a detailed Monte Carlo simulation to predict the performance in the Belle experiment. For production and propagation of Cherenkov photons, it takes account of chromatic dispersion effects both in the emission and propagation, and loss due to bulk absorption in the quartz medium and loss at each bounce. For photodetection, it uses the measured performance of the 4-linear-anode MCP-PMT, including TTS, quantum efficiency and collection efficiency, as described earlier. It also takes account of the effects of background Cherenkov photons produced via interaction of primary incoming tracks with the quartz material, including δ-ray emission and hadronic interactions, using the GEANT framework.

Figure 3.21 shows the obtained K/π separation contour in the two-dimensional plane of the polar angle (horizontal axis) and the momentum (vertical axis) of incoming tracks. The line representing the kinematics of two-body B decays is also shown. Here the geometry of the TOP counter module is same as that shown in Figure 3.15, and the quartz bar width is taken to be 40 cm. The figure indicates that the TOP counter provides K/π separation of more than 5σ in the regime of flavor tagging below 2 GeV/c, and more than 3σ for two-body B decays.

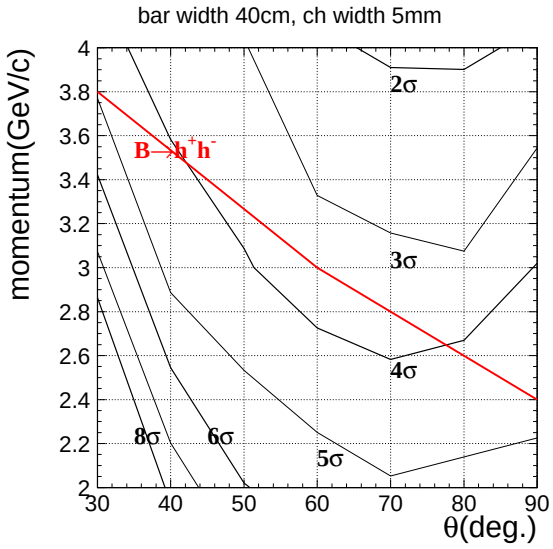

Figure 3.21: K/π separation contour in the two-dimensional plane of the polar angle (horizontal axis) and the momentum (vertical axis) of incoming tracks.

Beam Background Issue

In the high luminosity environment of Super-KEKB/Belle, beam-induced background is a potential problem. We have studied the rate of beam-induced background hits, using the spent beam generator in the Belle Geant framework. At the present KEKB luminosity, the generator gives spent e^+/e^- beams from Bremsstrahlung and Coulomb scattering at a total rate of 13 MHz. Background particles are then generated and their interactions with the TOP counter are simulated. According to the simulation, the rate of particles entering the TOP counter is 21 MHz (mainly photons and electrons) in the whole barrel array, and about 4% of them give

hits in the photodetector [2] This converts to 45 KHz particle hits per 40 cm wide module at the present luminosity, and 900 KHz assuming a background 20 times higher at the Super-KEKB. The simulation indicates that these particles leave hits in about 7 channels on the average among 60 channels in the module. Therefore, the overall detector dead time is about 1%, assuming 100 ns deadtime per hit for a single PMT channel. This dead time is in a tolerable range. However, estimation of the beam-induced background has large uncertainties, and we need further careful studies.

Possible Improvement

We think the above described performance is achievable with the technology at hand, and such a system would be ready for construction in time. We note here two possibilities to further improve the performance, although they require some new development.

- *Optimization of bandwidth in the photodetetion:* In the present design, the chromatic dispersion (σ_{chro}) makes a large contribution to the single photon resolution (σ_{time}). This can be reduced by utilizing photocathode, which is more sensitive for the longer wavelength region than the usual bialkali photocathode. For example, the GaAsP photocathode is known to be sensitive for the wavelength region of 450 $\sim$ 650 nm. It even has peak quantum efficiency as high as 40%, which compensates the decrease of emitted Cherenkov photons with the $1/\lambda^2$ dependence. We estimate that the $\sim 3.5\sigma K/\pi$ separation in the region around $(\theta, p) = (60^\circ, 3\mathrm{GeV}/c)$ can be improved to $\sim 6\sigma$ in this case. The critical issue for this option is the feasibility of producing a MCP-PMT, equipped with GaAsP photocathode.
- *3D imaging of Cherenkov photons:* If we measure each Cherenkov photon in three coordinates, i.e., measure the vertical emission angle in addition to (Φ, TOP), better K/π separation would be obtained. In this case, the chromatic dispersion can be corrected using the correlation between the emission angle and TOP. For instance, the vertical emission angle can be measured by introducing a mirror-based focusing optics, and a two-dimensional position measurement in the photodetection. Such possibilities are discussed in [14]. This will require space to accommodate the optical system. Another critical issue would be the development of a photodetector, which has both 2D position sensitivity and good timing resolution.

3.4.3 Aerogel Ring Imaging Čerenkov Counter (endcap)

Introduction

Identification of charged particles over the full kinematic range is one of the basic requirements for the upgraded Belle detector. The RICH, as described in this section, has been designed to separate kaons from pions over most of their momentum spectrum in the forward (endcap) part of the spectrometer,and to provide discriminaton between pions, muon and electrons below 1 GeV/c.

Detector Design Considerations

The elements of the proximity focusing RICH counter are (Fig. 3.22):

[2] For calibration, the same spent beam generator and Belle detector simulation predict 400 $\sim$ 500KHz hits for the present Belle-TOF at 0.1mips threshold. The observed rate is $\sim$ 200KHz, in a good agreement with the prediction.

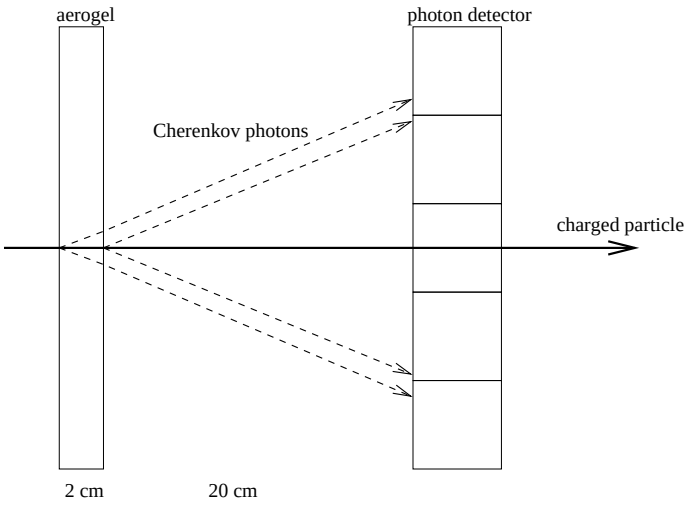

Figure 3.22: *Proximity focusing RICH - principle*

- a *radiator* where Čerenkov photons are produced by charged particles,
- an *expansion volume* to allow Čerenkov photons to form rings on the photon detector surface,
- an array of *vacuum based position sensitive photon detectors*, that is capable of detecting single photons in a high magnetic field with high efficiency and with good resolution in two dimensions, and
- a *photon detector read-out system*.

The design choices are governed by the following criteria and boundary conditions:

- To achieve the necessary performance, enough photons (about 10) have to be detected for each ring image, at least for one of the particle species. This requirement fixes the length of the aerogel radiator to a few centimeters.
- The space allocated to the device in the endcap area is 28 cm in depth.
- The required resolution in the measurement of the Čerenkov angle with such a photon detector is only achievable if the expansion gap is about 20 cm, and the radiator thickness does not exceed a few centimeters, while the photon detector granularity is at about a few milimeters.

Radiator

The Čerenkov radiator is aerogel, a material which is already used in the present Belle ACC (Aerogel Cherenkov Counter). A plane with 2 cm thick radiator tiles is mounted perpendicularly to the beam direction. This radiator was chosen since it combines low mass, a low Čerenkov threshold, and a low dispersion. For aerogel with refractive index $n = 1.05$ the Čerenkov threshold momenta for pions is at 0.63 GeV/c, and the Čerenkov angle corresponding to $\beta = 1$ particles amounts to $\theta_c = 310\,\text{mrad}$. At 4 GeV/$c$, pions and kaons are separated by 23 mrad.

In Fig. 3.23 the transmission curve is shown for a typical 2 cm thick radiator sample. Since

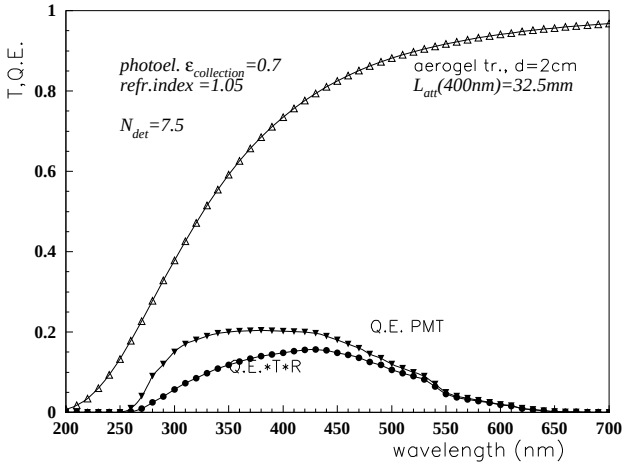

Figure 3.23: *Transmission curve for the aerogel radiator (2 cm) [28] and the quantum efficiency of a typical multi-alkali PMT (H8500 [27]).*

the losses of photons are dominated by Rayleigh scattering with a strong wavelength dependence (λ^{-4}) of the attenuation length Λ, the transmission varies considerably over the sensitive interval of a typical bi-alkali photocathode.

The optimal radiator thickness was determined by plotting in Fig. 3.24 the figure of merit, resolution in Cherenkov angle measurement per track,

$$\sigma_\theta^{\text{track}} = \frac{\sigma_\theta}{\sqrt{N_{pe}}},$$

which depends both on the resolution in Cherenkov angle measurement by a single photon σ_θ and on the number of detected photons N_{pe} (c.f. the R&D subsection, Fig. 3.32). The position of the minimum depends slightly on the transmission length. For a typical value of $\Lambda(400\text{ nm}) = 30$ mm, the best performance is achieved if the radiator thickness is around 20 mm.

Two possible tiling schemes of the aerogel radiator are shown in Fig. 3.25. One of the advantages of the hexagonal scheme is that the fraction of surface where the photon yield gets reduced due to tile edge effects is smaller (see Fig. 3.33). The hexagonal tiling needs three different tiles (full hexagon with 125 mm sides and two half-hexagons). The tiling with distorted squares needs three different tiles (one for each annulus), with a maximal side of about 220 mm.

Photon Detector

The position sensitive photon detector covers a surface of rougly 3.5 m^2, and is an essential component of the counter. The requirements for the photon detector are summarized as follows:

- Should be immune to the 1.5 T magnetic field,
- Should have single-photon sensitivity with a good single photon peak-to-valley ratio and high detection efficiency,

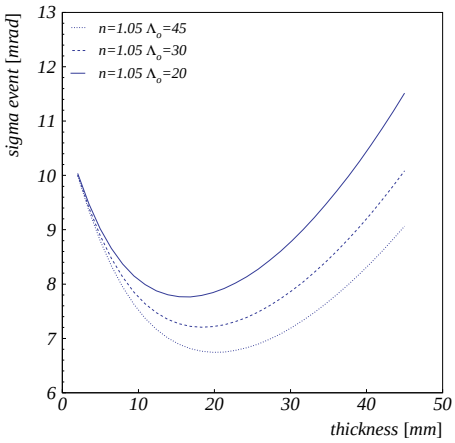

Figure 3.24: *Čerenkov angle resolution per track* $\sigma_\theta^{\text{track}}$ *as a function of the radiator thickness for three different attenuation lengths.*

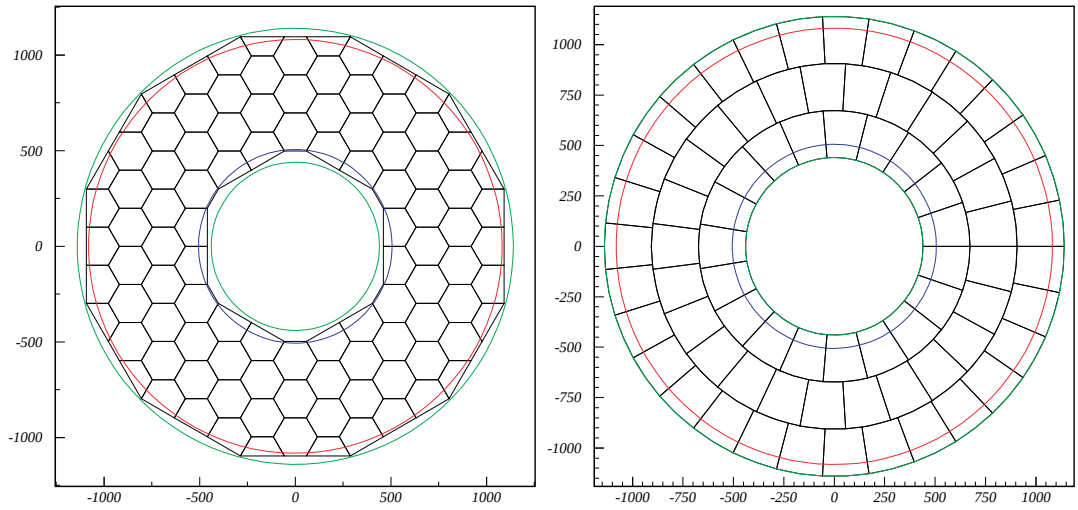

Figure 3.25: *Two aerogel radiator tiling schemes.*

- Should have position resolution (RMS) of less than 2 mm,
- Should have high sensitivity for photons of $\lambda \approx 400$ nm (c.f. Fig. 3.23).

Currently we consider a proximity-focusing-type Hybrid Photo-Diode (HPD) or a Hybrid-Avalanche-Photo-Diode (HAPD) as the best candidate, since they have both excellent single-photon resolution and high detection efficiency even in high magnetic field. Some kinds of HPD's are already commercially available [24]. However, we cannot use a focusing type HPD in a high magnetic field, and the effective area of the currently available proximity focusing type HPD is less than 50%. In order to enlarge the detection area of an HPD, we decided to develop with Hamamatsu Photonics K.K. (HPK) a new proximity focusing type HPD with a 5 mm square pixel size. Fig. 3.26 shows a schematic drawing of the H(A)PD, which has a housing of 72x72 mm^2 and 59x59 mm^2 sensitive area. This means 67% of the total area is covered by photo-diodes (PD) or avalanche PDs (APD). Four PD's or APD's, each with a 6x6 pixel array, are installed in a ceramic vessel as shown in Fig. 3.26, which leads to 12x12 pixels in total. The window is made of quartz and the photocathode material is multi-alkali.

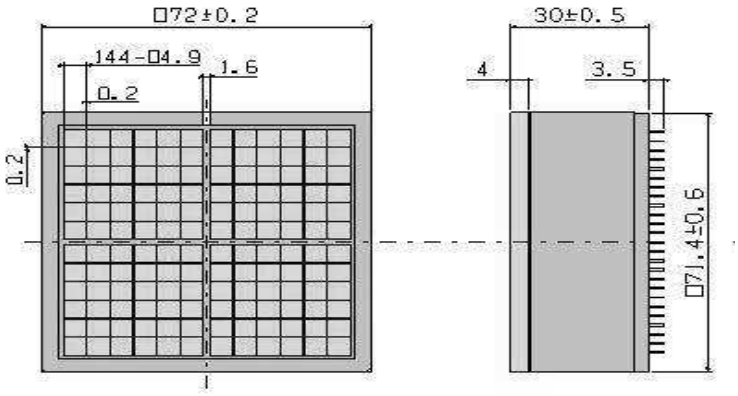

Figure 3.26: *Schematics of the proximity focusing hybrid photon detector (HPD) under development.*

A possible tiling scheme of the photon detector surface is shown in Fig. 3.27. The detector surface is covered with 600 HPD PMTs, with a 92% coverage.

Read-Out System

In parallel to the development of the photon detector, we are developing the readout electronics. Since the number of readout channels amounts in total to 86400, we need a special read-out scheme to treat them. We have therefore developed an ASIC that has the following properties:

a) High gain with short shaping times, 5V/pC and 150 ns,

b) Variable gain amp to adjust the threshold, x 1-16,

c) Pipeline readout scheme with a shift register,

d) Low power consumption, 5 mW/ch.

A schematic of the ASIC and a photo through a microscope are shown in Fig. 3.28. Only the on/off information after the comparator are registered in the shift register. When a trigger signal is accepted, the last 4 bits of the shift register are duplicated in a 4-bit register, which is read out serially.

As a fall-back solution we could employ a low noise read-out system based on the type used in the Belle silicon vertex detector (SVD), but adapted to the special needs of a single photon detector with pads. The system, an upgrade of the integrated circuit used in the CleoIII RICH [33], employs two chips, VA64tap with preamplifiers, amplifiers and discriminators for 64 channels, and LS64 with a 64 channel logic level adaptor stage [34]. The full read-out chain of the chip could be designed in a very similar way as for the read-out for the SVD2 counter.

Expected performance

Number of photons The expected number of Čerenkov photons was calculated by combining the measured values for quantum efficiency $\epsilon_q(\lambda)$ [27] and aerogel transmission $T(\lambda)$ (Fig. 3.23),

$$N_{phot} = 370\text{cm}^{-1}\; d\; \epsilon_e\; \epsilon_a\; \epsilon_t\; \sin^2\theta_c \int \epsilon_q(\lambda)\; T(\lambda)\; \lambda^{-2}\; d\lambda, \tag{3.3}$$

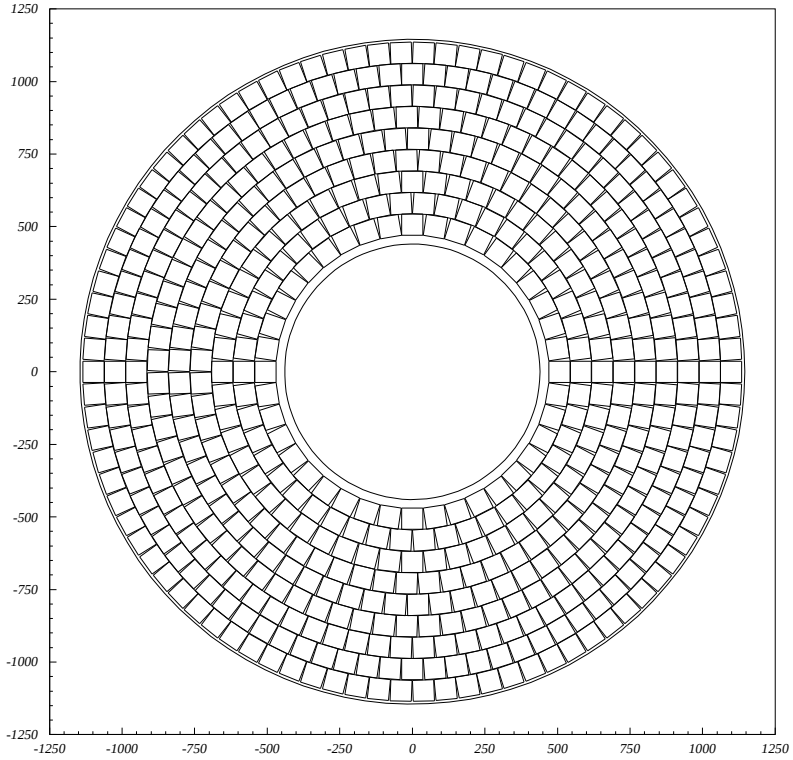

Figure 3.27: *Photon detector tiling scheme.*

where d is the radiator thickness (2 cm), ϵ_e is the single photo-electron pulse detection efficiency (estimated to be 0.70 for the HPD), and ϵ_a is the active surface fraction of the photon detector surface (0.67 in the case of HPD); $\epsilon_t = 0.92$ is the fraction of the surface covered with photon detector modules in a particular tiling scheme (Fig. 3.27). The resulting expected number of detected Čerenkov photons is 7.5.

Resolution of the RICH From the photon hit coordinate as measured by the photon detector and from the particle trajectory as given by the tracking chamber, the photon direction is reconstructed to obtain the Čerenkov angle and thus the velocity βc of the particle. Sources of error in the measurement by a single photon are as follows. The finite radiator thickness, $d = 2$ cm, contributes $\sigma_\theta^{emp} = d/(\ell\sqrt{12}) \sin\theta_c \cos\theta_c = 8.4$ mrad. The second contribution comes from the finite coordinate resolution of the photon detector $\sigma_\theta^{pix} = a/(\ell\sqrt{12}) \cos^2\theta_c = 6.4$ mrad, with a pad size of $a = 4.9$ mm and the radiator to photon detector distance of $\ell = 20$ cm. The chromatic error, a consequence of dispersion, the variation of the refractive index over the energy range of those Čerenkov photons that are detected by the photon detector, is determined from the measured variation of refractive index with wavelength, the transmission of aerogel and the photo-detector quantum efficiency (Fig. 3.23). From the resulting R.M.S. spread σ_n in refractive index we calculate $\sigma_\theta^{dis} = \sigma_n/(n \tan\theta_c) = 2$ mrad . From the experience with the HERMES RICH [21] we conclude that the contribution due to the imperfections and inhomogenuity of the

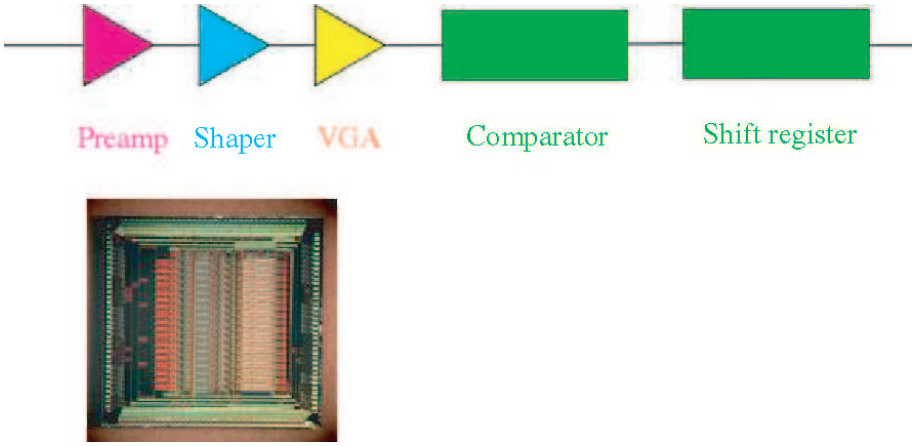

Figure 3.28: *Schematic and photo of the ASIC (4.9x4.9 mm^2).*

radiator can be estimated at 2 mrad. Finally, the contribution arising from the error in track parameters as determined by the tracking system and extrapolated to the radiator is expected to amount to $\sigma_\theta^{tr} = 5$ mrad$/(p/\mathrm{GeV}/c)$.

The combined single photon error is finally obtained by summing the above errors in quadrature. For 4 GeV/c momentum tracks it amounts to $\sigma_\theta = 11$ mrad. Assuming 7.5 detected photons for a $\beta = 1$ particle, the measurement precision is

$$\sigma_\theta^{(N)} = \frac{\sigma_\theta}{\sqrt{N}} = 4 \text{ mrad}. \tag{3.4}$$

In absence of backgrounds, the proposed counter would thus give a 5σ pion-kaon separation at the kinematic limit of 4 GeV/c. Pions would be separated at the 4σ level from electrons up to about 1 GeV/c.

Background Since the number of photons per ring is rather low, backgrounds could degrade the performance as discussed above. The following sources of background expected in the RICH photon detector were considered:

1. Rayleigh scattered Čerenkov photons from the same track.

2. Čerenkov photons emitted by the same track in the photon detector window.

3. Čerenkov photons emitted by other charged tracks in the event.

4. Čerenkov photons emitted by products of primary photon conversion in the material in front of the RICH radiator and in the radiator itself.

5. Beam related background hits.

6. Electronic noise.

The levels of backgrounds (1) and (2) were estimated from the test beam data (c.f. the R&D subsection, Fig. 3.31a), and turned out to be the dominant source.

The levels of backgrounds (3) and (4) were studied by simulation. Because of a rather small diameter of Čerenkov rings (12 cm) as compared to the typical distance between track impact points on the aerogel radiator, background (3) does not contribute significantly.

The level of source (5) was estimated from the current background rate in the endcap ACC, and scaled by a factor of 20 as expected from the luminosity increase. This rough estimate yields values from 60 Hz/cm^2 to 140 Hz/cm^2 for modules at the maximum and minimum radial distance from the beam. Finally, the electronic noise is estimated by assuming a conservative value of 10^{-3} for the probability of a noise hit.

In total, we expect 0.7 smoothly distributed background hits within the annulus of $\pm 3\sigma_\theta$ of the 4 GeV/c pion ring.

Particle identification capabilities The particle identification capabilities of the counter were evaluated by using simulated data. The backgrounds that are not included in simulation (sources 1,2,5,6) were generated according to observed or expected rates.

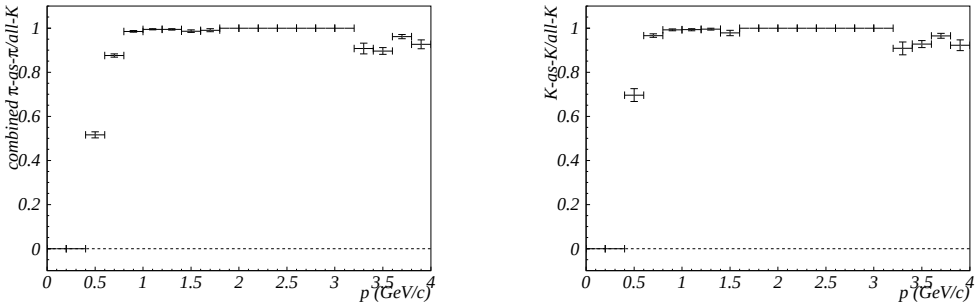

Figure 3.29: *Particle identification capabilities of the aerogel RICH counter: pion identification efficiencies at 5% kaon misidentification probability (left); kaon efficiency at 5% pion misidentification probability (right).*

R&D Results

Aerogel radiator The hydrophobic aerogel with a low refractive index ($n = 1.01 \sim 1.03$), developed for the Belle-ACC, is characterized by a high transmission length (~ 40 mm at a wave length of 400 nm). However, the transmission length of aerogel with a higher refractive index of $n = 1.05$ was less than one half the value of the aerogel with $n = 1.03$. Keeping in mind that for a collider experiment a hydrophobic aerogel is preferred to a hydrophilic one, we reexamined the hydrophobic aerogel production technique in a joint development with Matsushita Electric Works Ltd.

As a result, we found that the important factors determining the transmission length are the solvent and selection of the precursor to be used for its production. Originally, we used methyl-alcohol for the solvent, and methyl-silicate as a precursor [19]. When we applied dimethyl-formamide (DMF) [30], and changed the supplier of the precursor, we could improve considerably the transmission length of the aerogel. Fig. 3.30 shows the refractive indices of aerogel and the relation to transmission length for samples that were used in the beam test. The Matsushita(DMF) samples are clearly superior to other hydrophobic aerogels.

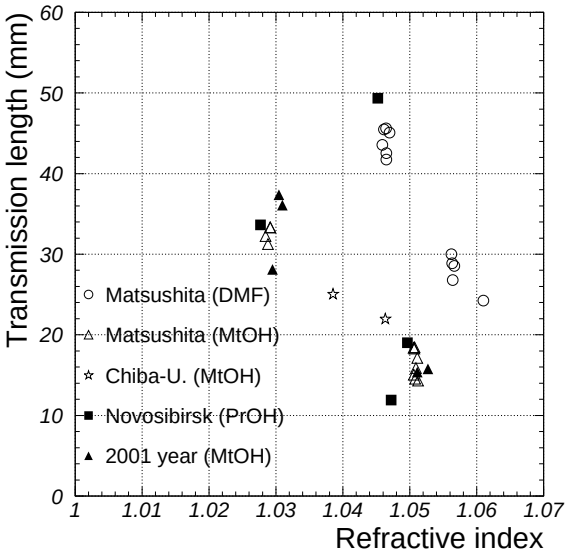

Figure 3.30: *Transmission length at 400 nm and refractive index at 405 nm for the aerogel samples used in the test.*

System test In a series of beam tests we have checked the performance of a complete system. While in the first test [25] at the KEK-PS $\pi 2$ beam line an array of multi-anode PMTs (Hamamatsu R5900-M16) was used for photo-detection, the recently developed flat-panel PMTs, Hamamatsu H8500, were employed in the second one [26]. 16 PMTs were used in a 4×4 array and aligned with a 52.5 mm pitch, with an effective photon detection area of 84%. At the back of each PMT, an analog memory board is attached to read out multi-channel PMT signals.

Most of the test measurements were performed with a π^- beam at 3 GeV/c. To systematically evaluate the detector performance, data were taken with different aerogel samples with various transmission lengths and thicknesses. Data were also taken by varying the π^- momentum in the range from 0.5 GeV/c to 4.0 GeV/c.

Fig. 3.31a shows a typical distribution of the Cherenkov-angle for single photons. Cherenkov photons from the aerogel radiator are clearly seen with a low background level. The flat background hit distribution on the photon detector is consistent with the assumption that it originates from Cherenkov photons that were Rayleigh scattered in the radiator. The peak at small Cherenkov angles is due to Cherenkov radiation generated by the beam particle in the PMT window.

Cherenkov-angle resolution for single photons The angular resolution was obtained from a fit of the Cherenkov angle distribution (Fig.3.31a) with a Gaussian signal and a linear function for the background. The resolution was typically around 14 mrad, independent of the refractive index. The main contributions to the resolution of the Cherenkov angle come from the uncertainty in the emission point and from the pixel size of the PMT. The measured variation of the resolution with the thickness of aerogel is shown in Fig. 3.32 together with the expectations. The measured resolution matches the expected values reasonably well, apart from a discrepancy between the two, which could be accounted for by a constant additional

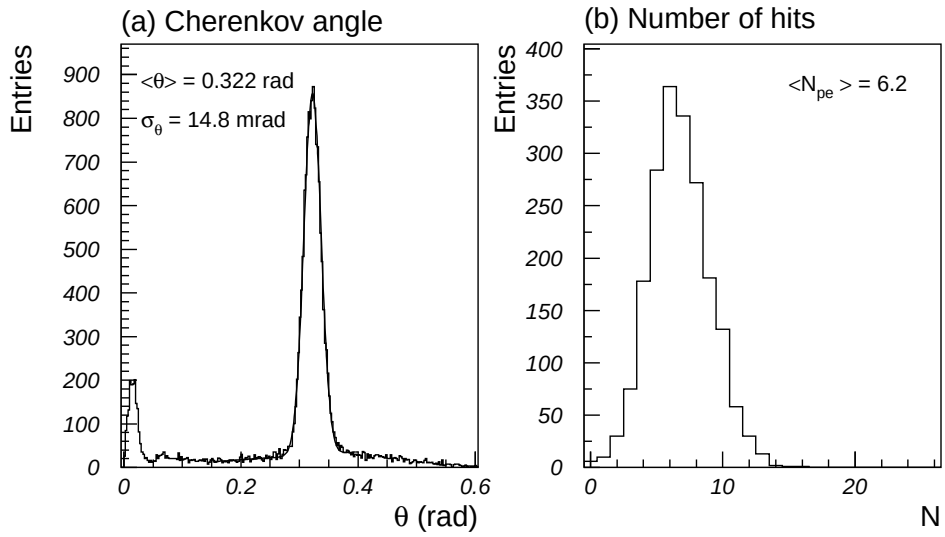

Figure 3.31: *Distribution over the Cherenkov angle for single photons (a), and the number of detected photons per ring (b), for a* 20 *mm thick aerogel radiator sample with* $n = 1.056$ *and a transmission length of* 30 *mm.*

contribution of about 6 mrad. The discrepancy could arise from the effect of aerogel (non-flat aerogel surface and possible non-uniformities in the refractive index due to position variation and chromatic dispersion), which are the subject of further investigation.

Photoelectron yield Fig. 3.31b shows a typical distribution of the number of hits within $\pm 3\sigma$ from the average Cherenkov angle. The number of hits for the signal region was estimated by subtracting the background from the fits to the Cherenkov-angle distribution. Fig. 3.32 shows the dependence of the number of detected photons on the aerogel thickness. As expected, the number of photons does not linearly increase with the aerogel thickness, but saturates due to the scattering effect in aerogel. For pions with momenta above 1 GeV/c, the number of detected Cherenkov photons was typically around 6 for aerogel samples with $n = 1.05$. The deviation from the expected value (about 9) can be accounted for by the rather early stage of development of the employed PMT tubes. In fact, if normalized to the best tubes in the second delivery batch, the yield per ring is very close to the expected value.

It has been already noted by the HERMES group [21] that a loss of Cherenkov photons occurs at the side wall boundaries between adjacent aerogel tiles. We have confirmed this finding by measuring the number of photons on the Cherenkov ring as a function of the distance of the charged particle impact point from the boundary between two tiles. The measurement is shown in Fig. 3.33, where a dip is seen at the tile boundaries for two different tiling schemes. In order to eliminate other geometrical factors, for example, the acceptance of the photon detector, the measured yield was normalized to the yield obtained with one tile covering the entire range. The result clearly indicates a reduction of yield when the charged particle is closer than about 5 mm to the boundary of a 2 cm thick aerogel tile. It is worth noting that a simple model, where all photons hitting the boundary between the two tiles are lost, accounts for most of the observed

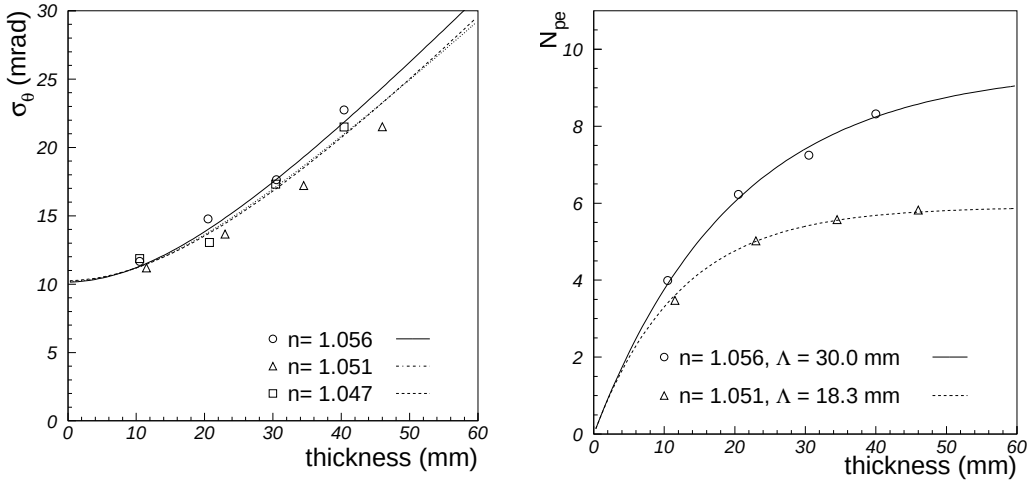

Figure 3.32: *Angular resolution (left) and the number of detected photons per Cherenkov ring as a function of the aerogel thickness. The symbols correspond to the data recorded with different aerogel samples.*

dependence. From this result it is clear that the tile size should be as large as possible to reduce the impact of the loss.

Particle Identification Finally, we estimate the performance of pion/kaon separation in the momentum range around 4 GeV/c. If we take into account a typical measured value for the single-photon angular resolution, $\sigma_c \sim 14$ mrad, and the number of detected photons $N_{pe} \sim 6$, typical for 20 mm thick aerogel samples with $n = 1.05$, we can estimate the Cherenkov angle resolution per track to be $\sigma_c/\sqrt{N_{pe}} =$ 5.7 mrad. This naive estimate is also confirmed by the direct measurement shown in Fig. 3.34. Here, the track-by-track Cherenkov angle is calculated by taking the average of the angles measured for hits around the predicted position of the Cherenkov ring. From this we can deduce that at 4 GeV/c, where the difference of Cherenkov angles for pions and kaons is 23 mrad, a 4σ separation between the two is possible. As an

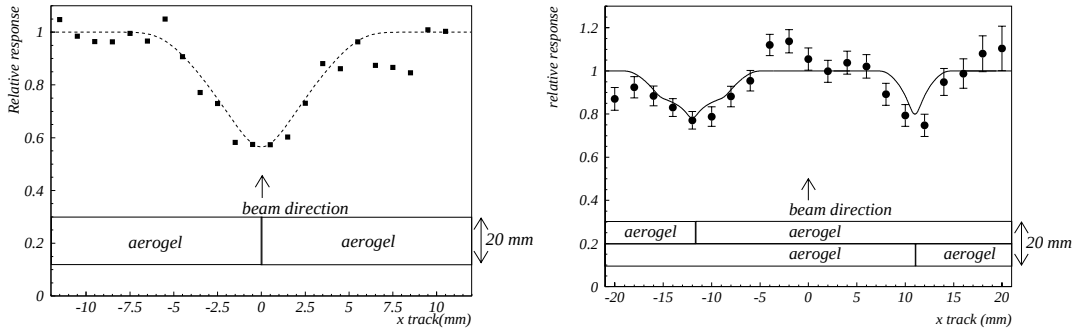

Figure 3.33: *The number of Cherenkov photons detected on the ring, as a function of the charged particle impact point position on the aerogel tile. The values shown are normalized to the measured values in case of a single tile covering the full range. Also shown is the estimate of a simple model.*

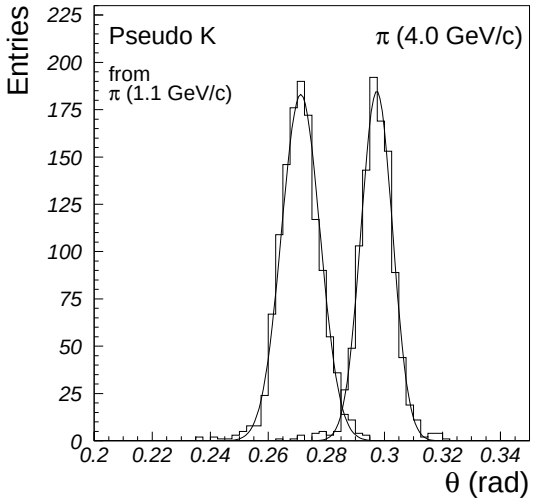

Figure 3.34: *Cherenkov angle per track for pions of* 4.0 GeV/c *and* 1.1 GeV/c. *Pions at* 1.1 GeV/c *are used to represent the kaon beam of* 4 GeV/c. *The angular resolutions for* 4.0 GeV/c *and* 1.1 GeV/c *are* 5.4 *mrad and* 6.7 *mrad and two peaks are separated by* 4.2σ.

additional cross check, we have also collected data with a 1.1 GeV/c pion beam of , which can be used to represent a 4 GeV/c kaon beam (apart from a slightly larger sigma due to multiple scattering). As can be seen from Fig. 3.34, the two peaks are well separated.

HPD development Although the system test was very successful, there are still several issues that have to be solved for implementation in the Belle spectrometer. The most important item is the development of a PMT that can be operated in a high magnetic field (1.5 T). In order to confirm the ability of candidate photon detectors HPD and HAPD to efficiently detect single photons over a large active area, a single channel HPD and a 3x3 multi-channel HAPD were tested by using a laser diode light pulser ($\lambda = 850$ nm). Fig. 3.35 shows a multi-photon spectrum obtained by a HPD, which was operated at 8 kV for electron bombardment (EB) (typical EB gain was 1500) and 80 V for bias. The leakage current was 4 nA and the detector capacitance was 20 pF.

Multi-photon spectrum was also obtained by the HAPD prototype (Fig. 3.36). The gain was higher ($2.6 \cdot 10^4$) in the case of the HAPD due to the avalanche gain of about 15. However, the detector capacitance was 73 pF and the leakage current amounted to 14 nA, resulting in a worse signal to noise ratio than in the case of the HPD. Although both the HPD and the HAPD have demonstrated an excellent performance, the HPD has a slightly better resolution.

Prototype production of APD's and PD's is going on at HPK, and evaluation of the samples is being carried out. While so far there are no serious problems for the PD's except for a slightly worse timing response, a large leakage current was observed in APD's after the activation of photocathode. Futhermore, larger noise than expected is seen in APD's. Hamamatsu Photonics is investigating the HAPD's to solve this problem in the next batch. A delivery of prototype 12x12 channel HAPD's is expected in January 2004, and a beam test is planned for February.

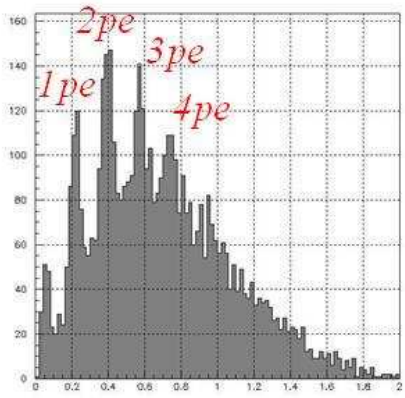

Figure 3.35: *Multi-photon spectrum obtained by the single-channel HPD.*

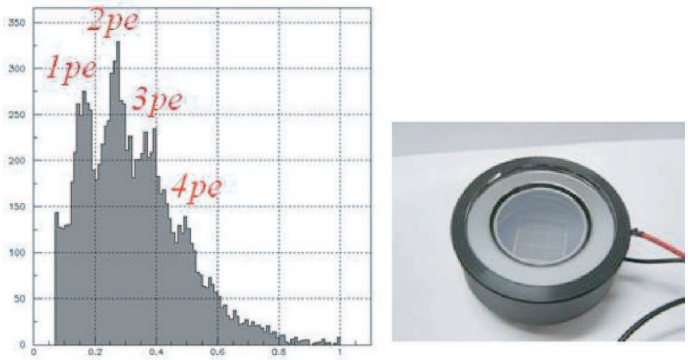

Figure 3.36: *Multi-photon spectrum obtained by the 3x3 multi-channel HAPD and a photo of the HAPD.*

3.4.4 Other possibilities

10ps TOF

In order to obtain better PID power, we are studying a very-high-resolution time-of-flight (TOF) counter. This TOF counter uses Cerenkov lights radiated in a small crystal block. For practical use, these counters are setup as tiles in the current TOF region.

Test counter

We have studied a simple test-counter, whose design is shown in Fig. 3.37. Charged particles go through the quartz block and the photo-detector. To improve the time resolution, we implement the following features: (1) Instead of scintillation light, Cerenkov light is used because the emission time is negligibly small. (2) A small size radiator is used in order to reduce the time spread of the internal reflecting photons, which is due to the propagation length spread and the chromatic dispersion of the light velocity. (3) A high-resolution phototube whose transit-time-spread (TTS) is $\sigma_{\rm TTS} = 50 \sim 100$ ps for a single photo-electron is used. Such a phototube gives good performance, even though the number of Cerenkov photons is much smaller ($100 \sim 200$ photo-electrons) compared to scintillation light. In a simulation study, the expected time resolution is less than 10 ps.

We carried out a beam-test at the π2-line of the KEK-PS in December 2002. The two types

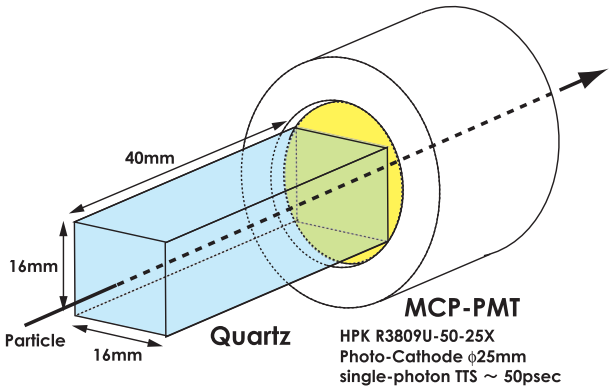

Figure 3.37: Test counter with a MCP phototube.

of photo-multiplier-tubes, L16-PMT(HPK R5900U-00-L16) and MCP-PMT (HPK R3809U-50-25X), are tested. The purpose of the beam-test is to confirm the performance. To evaluate the time resolution, we put two identical counters along the beam direction and measured the residual of detected time between the up-stream and down-stream counters.

The L16-PMT is a metal-packaged line-focus-type PMT with 16 channel anode. The TTS for each channel is $\sigma_{\rm TTS} \sim 75$ ps for a single photoelectron. One advantage of the L16 is that the required time resolution for each channel is not so severe because we can use 16 measured-times. For the L16-PMT, the number of detected photo-electrons is ~ 120 in total and the obtained time-resolution is ~ 30 ps for each channel. By averaging over 16 channels, a time-resolution of $\sigma_{\rm L16} = 12.1$ ps is obtained.

The MCP-PMT is a single-anode PMT equipped with two micro-channel-plates, whose TTS is $\sigma_{\rm TTS} \sim 50$ ps for a single photo-electron. For the MCP-PMT, the number of detected photo-electrons is 150 - 200 and the resolution is $\sigma_{\rm MCP} = 10.6$ ps, as shown in Fig. 3.42.

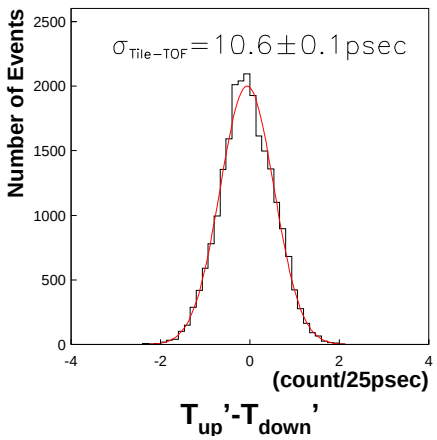

Figure 3.38: TDC residual distribution between up-stream and down-stream counters of the MCP type.

In this beam-test, we have obtained a 10.6 ps resolution and confirmed that our idea is correct in principle. For both types, we obtain the expected number of detected photo-electrons. However, the time resolution is somewhat worse than the expectation, which is due to time fluctuation in the readout electronics. The error of the readout system is measured to be

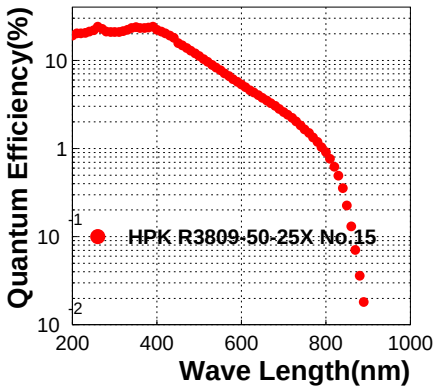

Figure 3.39: Quantum efficiency depending on the light wavelength for the MCP (HPK R3809U-50-25X) measured by HPK.

$\sigma_{\mathrm{elec}} \sim 9$ ps.

Simulation

Based on the beam-test result and the pulse-laser test result, we have developed some reliable simulation programs to make a design with a larger radiator and different incidence situations. The following conditions are implemented into the simulation:

- The number of generated photons is ~ 1900 for a 20 mm path-length and depends on the wavelength λ of the Cerenkov light.
- The generated position and direction follows the Cerenkov cone. The Cerenkov angle depends on λ.
- The time offset due to the time-of-flight of the incident charged particle and the propagation time of the Cerenkov light in the radiator is considered.
- Chromatic dispersion is included. (Light velocity in the radiator depends on λ.)
- The quantum efficiency (QE) is ~ 18 %, which is modeled by the measurement shown in Fig. 3.39. The correction efficiency (CE) is 36%.
- The TTS is 50 ps. The time fluctuation follows a Gaussian distribution.
- The pulse shape for single photons and ADC fluctuation are modeled by the pulse-laser measurement. The implementation of pulse response generates the time-walk effect.

An example of an event display is shown in Fig. 3.40. Here, the incident angle and distance from the PMT are 45° and 100 mm, respectively. The radiated Cerenkov photons indicated by blue lines propagate in the radiator ($200 \times 100 \times 20$ mm) and reach the PMT. The time distribution of the Cerenkov photons are shown in Fig. 3.41. In this case, the number of detected photons is ~ 116 per event, and the time resolution is ~ 18 ps.

Conceptual layout

The time resolution is approximately determined by the number of photons in the wavefront and it largely depends on the incident angle and incident position (distance from photo-detector). Fig. 3.42 shows a contour plot of the time resolution, which depends on the incident angle and distance for $\pi^{\pm}$ particles with $p = 3.0$ GeV/c. The definition of the incident angle and distance is indicated in Fig. 3.43. In the MC studies, there is no significant difference between the time resolution for momenta in the range of $1.0 \sim 4.0$ GeV/c at least. The contour plot shows the

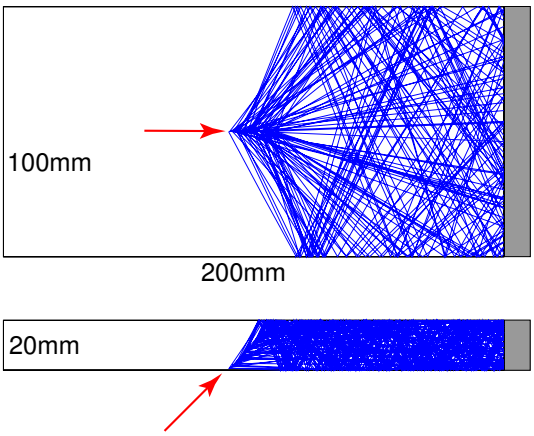

Figure 3.40: One event display. The incident position and direction is indicated by red arrow. Blue lines show the trajectory of Cerenkov photons and gray box shows the PMT.

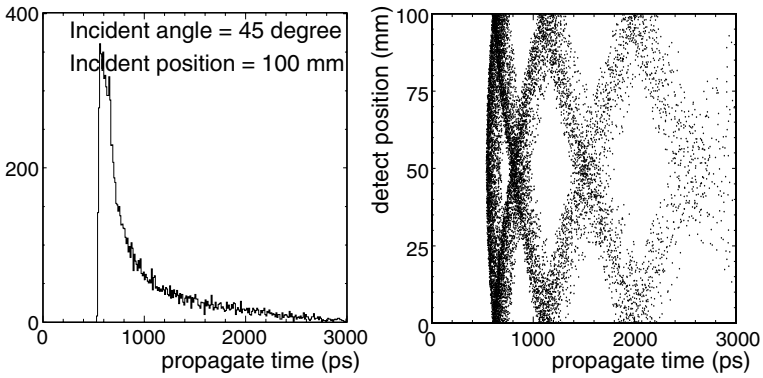

Figure 3.41: Propagation-time distribution (left) and its dependence on the detected position on the PMT (right).

good time-resolution when the incident angle is small and the distance is short. However, it is hard to reach a 10 ps resolution for wide acceptance using this radiator shape.

If we decide that the time resolution must be less than 20 ps, the length of the radiator l can be expressed as a linear function of incident angle α by $l(\mathrm{mm}) = 4 \times (90^\circ - \alpha(\mathrm{degree})) + 20$. Because the incident angle directly depends on the polar angle θ of a incident particle, the relation between θ and l is expressed by $\theta(\mathrm{degree}) = 90^\circ + \tan^{-1}\left(\frac{20}{l}\right) - \frac{l-20}{4}$, where l is in mm and the thickness of the radiator is 20 mm. Following this relation, we can draw the conceptual layout shown in Fig. 3.44. In order to keep the 20 ps resolution for all regions, the radiator length changes gradually depending on the z-position.

The point of this detector is summarized in the following:

- A small Cerenkov radiator and high resolution PMT is used.
- There is robustness for a high hit-rate (background-rate) because of the small acceptance per counter.
- Existing technologies (Quartz and MCP-PMT) are used.
- Many trigger topologies can be formed.
- There is room for optimization of the radiator shape because the incident angle is limited

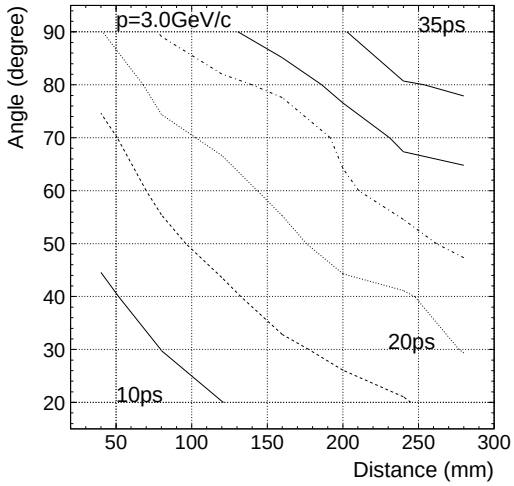

Figure 3.42: Contour plot of the time resolution versus the incident angle and distance for $\pi^{\pm}$ of $p = 3.0$ GeV/c.

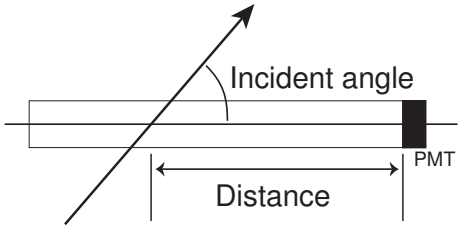

Figure 3.43: Definition of incident angle and distance.

due to the small acceptance.

The next R&D items are 1) to make a test counter with the larger radiator in order to confirm the simulation result, 2) to design a optimized shape and 3) to develop a very-high-resolution readout system. A PMT with a large effective acceptance is also one of the next R&D items, which is also part of the TOP R&D program.

50ps TOF

Conceptual design of 50 ps TOF counter

The design of a 50 ps TOF is based on the performance of the present TOF system for Belle detector, which has achieved a 100 ps time resolution, and provides 3σ π/K separation up to 1.2 GeV/c.

The present Belle TOF system consists of 128 scintillation (BC408) counters of 6cm width, 4 cm thickness and 255cm length arranged in a barrel with a radius of 1.2m. Each TOF counter is viewed at both ends by R6680 PMTs. This system works at a luminosity of $10^{34}/\mathrm{cm}^2/\mathrm{s}$ with an efficiency of better than 90%.

It also provides a fast event timing signal in online with a precision of 2 ns, that helps the T0 determination for the tracking chamber and other subdetectors. In offline analysis, the TOF hit timings are used to determine the event timing with a precision of 0.5 ns for track reconstruction.

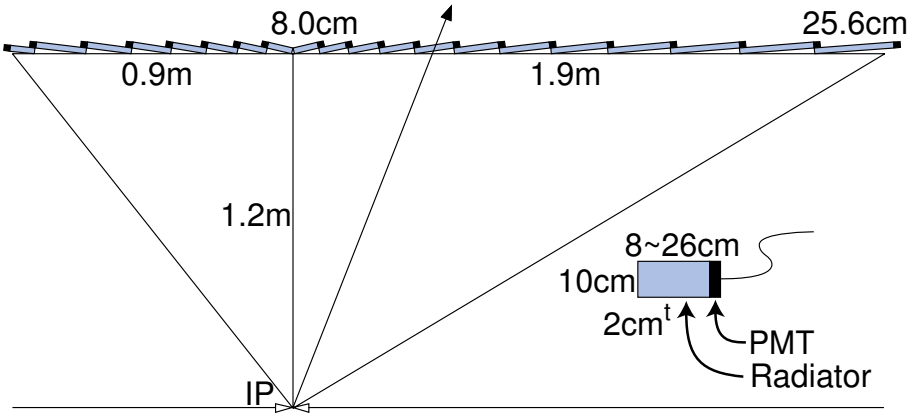

Figure 3.44: Conceptual layout of tile TOF.

Figure 3.45 shows the time resolution as a function of z position for a prototype Belle TOF counter, which was measured in the beam test in 1996. An intrinsic time resolution of 80ps was obtained at the center of a typical counter.

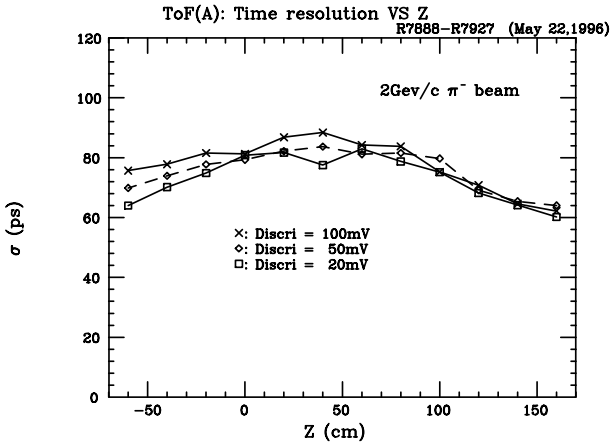

Figure 3.45: Time resolution of the present Belle TOF.

From this test result, we can design a 50ps TOF system with a fine segmentation along the z-direction. Figure 3.46 shows the conceptual design. One TOF counter of 255 cm length is divided into three counters of 100 cm length. We expect an intrinsic time resolution of 50 ps by assuming that it is scaled with square root of the counter length. Beam tests of BC408 and BC404 should be done to confirm this design.

The dominant background in the TOF counters is caused by spent electrons and positrons in the ring, which hit the beam pipe and masks in the interaction region and generate electromagnetic showers. Photons interacting inside a TOF counter give a high rate of small signals. In the present TOF system, we have 12 cm wide and 5 mm thick scintillation counters (TSC) 15mm in front of a TOF counter. The coincidence between the TOF and TSC can eliminate fake signals due to photon interactions in TOF counters. The rate reduction is about a factor of 3.

The short counter can reduce the signal rate, proportionally to the counter length. In the 50 ps TOF design, we have two layers of 6 cm wide and 2.5 mm thick TSC at inner and outer sides

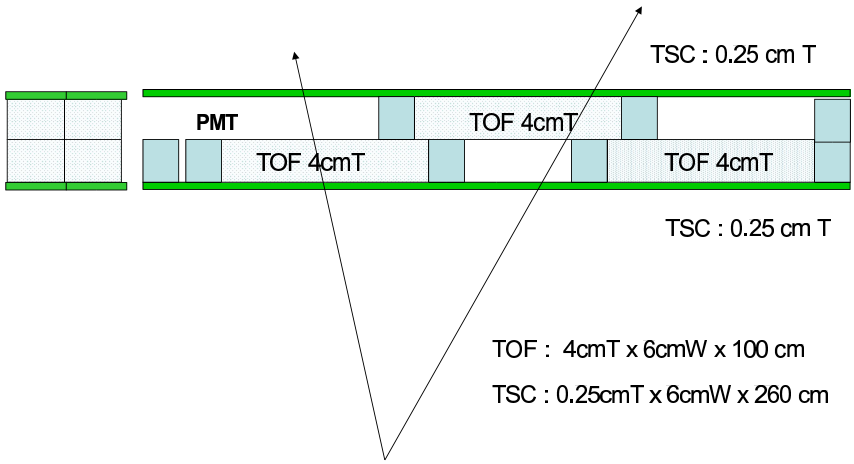

Figure 3.46: Conceptual design of a 50 ps TOF

of the TOF counters. As the separation gap is about 4 cm, we expect a larger reduction of the photon background rate. Table 3.8 indicates the counter dimensions. The material thickness of TOF and TSC counters is the same as the present TOF system, which is 11% of a radiation length. This design requires 110 mm in radial space, which is larger than 80 mm for the present TOF system.

Table 3.8: 50 ps TOF configuration.

Counter	Scini.	W × T × L (cm)	Seg.($\phi \times Z$)	PMTs
TOF	BC408/BC404	$6 \times 4 \times 100$	128×3	×2
TSC(inner)	BC412	$6 \times 0.25 \times 260$	128×1	×1
TSC(outer)	BC412	$6 \times 0.25 \times 260$	128×1	×1

PID capability

Figure 3.47 shows the π/K separation capability in σ's with TOF and CDC dE/dx measurement. It is stressed that 25ps TOF and 4% dE/dx can cover the entire momentum region with more than 3σ separation. A 50 ps TOF with 6% dE/dx only provides 2σ separation at momenta above 2 GeV/c. If a 50ps TOF system could coexist with the present ACC, this design is a good backup option.

System error for precise TOF measurement

In the present TOF system, we have a systematic error of 50ps in the readout, which has the following components;

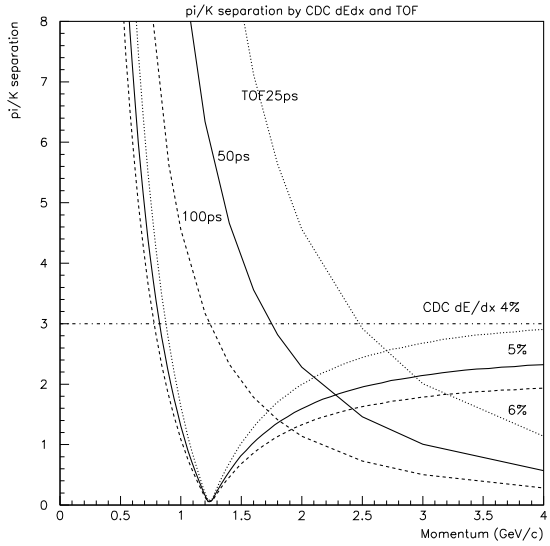

Figure 3.47: π/K separation with TOF and CDC dE/dx.

1. *Time jitter in beam collision;* A beam size of 7 mm corresponds to 20 ps. There may be an additional jitter of a few ps due to the variation of the beam phase with respect to RF clock for each bunch.

2. *Readout errors in the time stretcher;* We found an error of 20 ps in a bench test of the time stretcher.

3. *Discriminator and ground level noise;* As we are using preamp of 5 times, the time jitter in the discriminator is less than the ground level noise. We observed 5 mV ground level noise and set the discrimination level at 50 mV. We guess the error to be 10 to 20 ps.

4. *Error in time walk calibration;* We have an error in the time walk calibration, which matches the measured TOF timing to that expected from tracking. The calibration also includes tracking systematics. A path length error of 6 mm in tracking corresponds to 20 ps. Assumption of the TWC calibration function also gives some systematics. From the maximum deviation between the data and expected TOF after calibration, we estimate a total error of 30ps for the time walk correction, including the errors due to tracking.

5. *Particle and momentum dependence;* We are making an empirical correction to match the data to the predicted one using a large data sample. It is dependent on tracking code itself, in particular at low momenta, while it is not essential to separate π/K at higher momenta.

To achieve 50 ps, we need to reduce the above systematic errors to a total of less than 20 ps.

Estimation of TOF rate and requirement of fast readout system

Table 3.9 shows the TOF rates and hit efficiencies for various cases, which are estimated using the recent Belle data. The nominal threshold is set at 0.2-0.25 mips, which corresponds to about 2 MeV of energy loss in a TOF scitillator. The energy loss in a 4 cm thick TOF is

8 MeV and varies with the incident angle. The inefficiency of TOF hits is found to be 3% in data at a luminosity of 10^{34}. The present readout uses a MQT for Q and a time stretcher for T measurements with 600 ns dead time, which was developed ten years ago. However, this scheme is not fast enough for the higher background.

With 1m TOF counters (3TOF opt.) and a fast readout, we can keep the TOF hit inefficiency less than a few %. It is essential to develop fast readout for T and Q measurements with 100 ns or shorter dead time.

Table 3.9: TOF hit efficiency at a luminosity of 10^{35} for various assumptions.

L $(cm^{-2}s^{-1})$	$I_{HER}(A)$ $\times I_{LER}(A)$	Background assumption	Rate(KHz)/Ineff(%) w/ 1-TOF opt.	Ineff(%) w/ 3-TOF opt.	Ineff(%) w/ 100ns elec.
10^{34}	1×1.5	exp27	44/3		
10^{35}	4×6	$\propto (I_{HER} + I_{LER})$	174/12	58/4	
10^{35}		$10 \times L$	440/30	147/10	2-3
10^{35}		$20 \times L$	880/60	293/20	3-4

3.5 Calorimeter

3.5.1 Upgrade plan

Endcap

For the endcap calorimeter we propose using pure CsI crystals of the same shapes and sizes as the CsI(Tl) crystals of the Belle endcap calorimeter. The light readout will be performed with 2" vacuum phototetrodes R2185UV attached to the crystals with optical contact. Voltage dividers and preamplifiers are mounted on crystals. High voltage for the dividers is supplied by one power supply for 1/16 of the endcap and distributed inside the segment. Modified Belle calorimeter preamplifiers will be used. The modification includes changing the output cascade to a differential transmitter. The signal from the preamplifier is sent to the intermediate electronics via the same twisted pair cable that is used now.

The intermediate electronics is implemented on TKO boards. The TKO board contains 16 channels (Fig. 3.5.1). Each channel includes a differential receiver, CR-$(RC)^4$ shaper with shaping time $\tau = 30ns$ and three 12-bits flash ADCs. Usage of three ADCs allows us to have an effective 18-bit digitization for a full dynamical range. Digitization of the signals from the

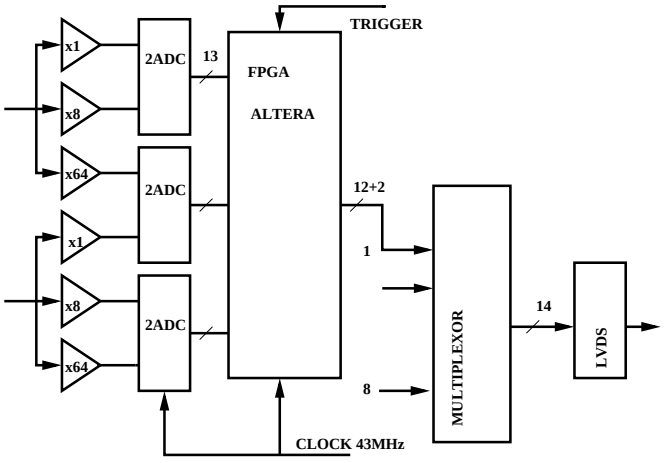

Figure 3.48: Electronics of the TKO board for the endcap calorimeter.

shaper outputs will be performed under the control of a 43MHz common clock. The logic will select a range according to the measured amplitude. The data are continuously recorded in a buffer of 256 words (it takes about $6\mu s$). After the trigger signal comes, the data are sent to the COPPER module where they are processed. The digital processing of the data provides the amplitude and the time of the signal.

The TKO modules also produce analog sum signals corresponding to 4x4 clusters that are used for the neutral trigger. The neutral trigger will be made in the same frame as the current one.

In total, the endcap electronics will include 144 TKO boards located in 16 crates and 36 VME COPPER modules located in 2 crates.

Barrel upgrade

For the barrel part of the ECL our approach is to improve background performance of the calorimeter minimizing the modifications of the hardware. In the barrel the background condi-

tions are not so severe, so we try to keep present crystals and photodetectors and modify only the electronics.

In the upgraded electronics the present preamplifiers and cables from the preamplifiers to shapers will be kept. The shaper and digitization part will be upgraded.

The shapers will be made on a TKO board keeping the current density of 16 channels per board. Each channel consists of a shaping amplifier CR-$(RC)^4$($\tau_s = 0.5\mu s$) with self controlled gain(x1/x16) and a 14 bit ADC. The scheme lay out is shown in Fig. 3.49.

The digitization of signals from the shaper output will be performed under the control of the common clock 43/20=2.15MHz. 16 channels of amplitudes plus 2 control sums will be multiplexed to one line and transmitted to a COPPER module at 43 MHz using 18 twisted pair cables (the same cables that are used now for TKO-TDC connection will be used). The COPPER VME module will contain 4 FINESSE boards (Fig. 3.50). In total, one COPPER module serves 64 channels. In the FINESSE board the data are continuously recorded to a buffer of 256 words. After a trigger signal comes, the data are recorded to the FIFO of COPPER where digital processing of the data will be performed to obtain the signal amplitude and timing.

In total, the system contains 432 TKO modules arranged in 36 TKO crates, and 108 COPPER modules located in 9U 6 VME crates.

A prototype module for the electronics described above has been developed and is being produced in BINP. It will be ready at the beginning of 2004.

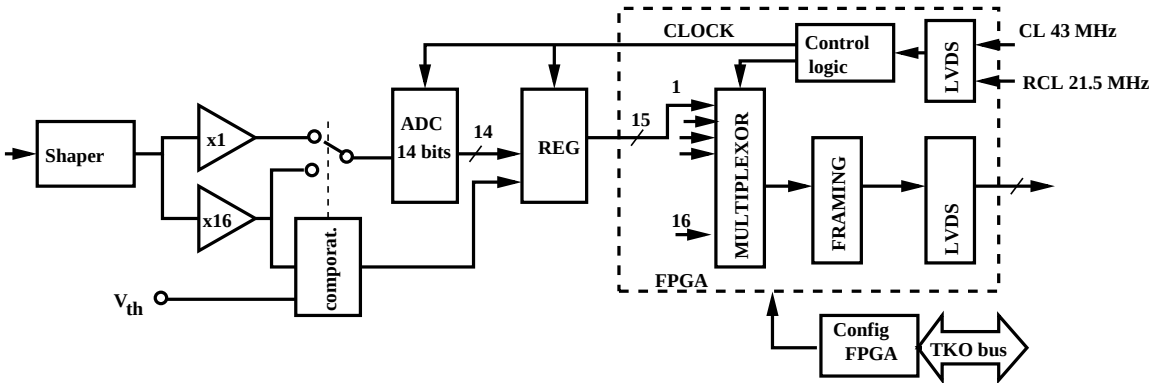

Figure 3.49: Layout of the scheme for digitizing part of the TKO module.

3.5.2 Study of the Belle CsI calorimeter prototype with BINP tagged photon beam

A test of the calorimeter prototype based on pure CsI crystals was carried out using the photon beam produced at the ROKK-1M facility of BINP. Fig. 3.51 shows the layout of the ROKK-1M facility [37]. A neodym (Nd:YAG) laser with second harmonic of energy 2.34 eV is used as the source of the photons. The resulting Compton photon spectrum is roughly uniform with a sharp edge corresponding to the maximum energy $\omega = 4\gamma^2\omega_0 \ / \ (1 + 4\gamma\omega_0/m_e)$, where γ is a relativistic factor for electrons in the initial beam, ω_0 is the energy of the laser photon and m_e is the electron mass. The energy resolution can be studied both by analyzing the smearing of the Compton edge in the measured spectrum or using tagging system(TS) information. The TS measures the energy of the scattered electrons and provides photon energy resolution better than 1%.

The CsI setup layout is shown in Fig. 3.52.

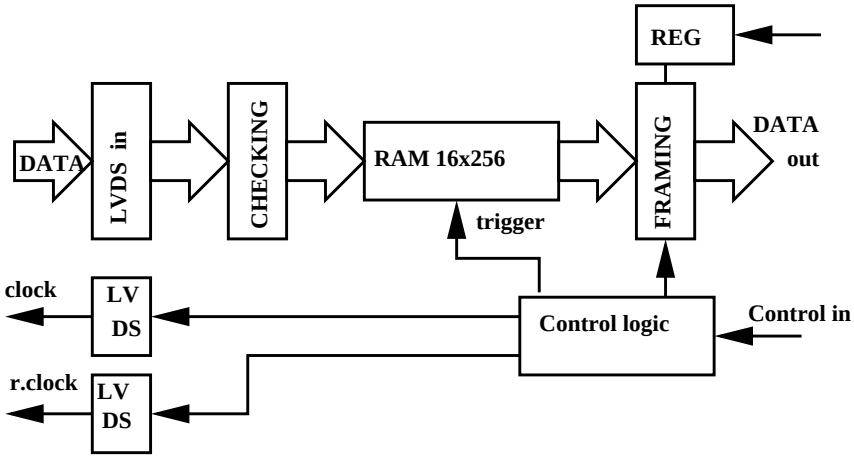

Figure 3.50: Schematic layout of the FINESSE board.

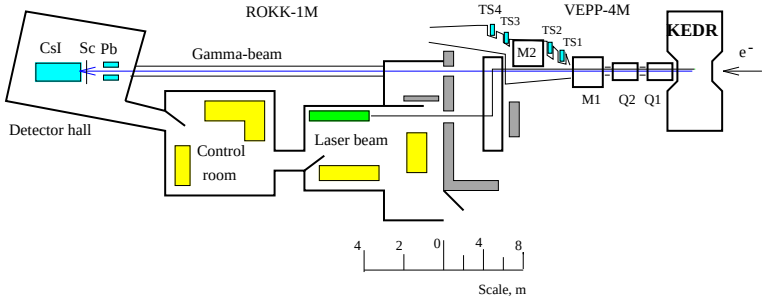

Figure 3.51: Layout of the VEPP–4M experimental region with the KEDR tagging system. Q_1, Q_2 are quadrupoles, M_1, M_2 are bending magnets

The prototype consists of 20 pure CsI crystals mounted in a 4x5 matrix. The crystals are the same shape and size as the Belle forward endcap calorimeter elements of types 12-19. Their length, 30 cm, corresponds to 16.1 X_0. Each crystal is wrapped with one layer of white 200 μm Gore-Tex film reflector and placed in a 50 μm aluminized mylar envelope. The light of each crystal is detected by a 2" phototetrode R2185UV that is coupled to the large end face of the crystal with optical grease. The phototetrode is connected to a preamplifier that is mounted on the crystal. Before mounting tetrodes the light output and the light output nonuniformity of the crystals were measured with collimated Cs^{137} of 662 keV γ source using 2 inch PM-tube.

In the low energy region (i.e. below 100 MeV) the energy resolution of the CsI calorimeter is dominated by electronic and pile-up noise. To suppress the contribution of pile-up noise, a short shaping time of 30 ns has been chosen.

The modified charge sensitive preamplifier designed for the Belle CsI calorimeter Ref. [36] is used. The first stages are the same as the standard one while the last stage was changed to a differential transmitter.

The signal from the preamplifier is sent to a CAMAC module via the twisted pair cables that are used now in the Belle calorimeter. The CAMAC module contains 4 channels. Each channel includes a differential receiver, shaper containing a differential stage and two stages of integration by active Bessel shapers with shaping time $\tau = 30$ns and two 12-bit flash ADCs. The sensitivity of the high range ADC is 8 times lower than the low range one.

The shaper output pulse is digitized under the control of the 40MHz common clock. The

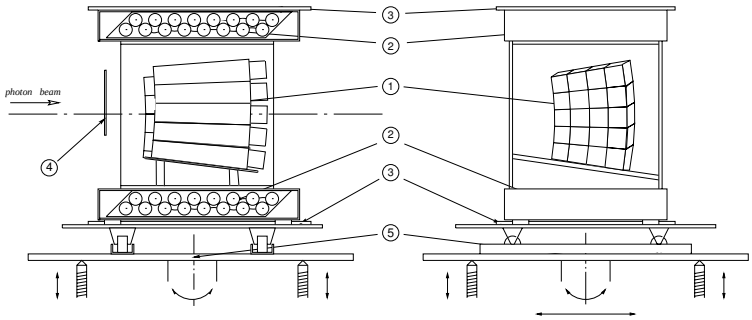

Figure 3.52: Layout of the CsI matrix at VEPP-4M.

data are continuously recorded in a buffer of 256 words depth. After the trigger signal comes, the data are readout.

Since electronic noise is the crucial point for calorimeter resolution at low energy, this characteristic was carefully measured. By comparing the RMS of pedestals for single channels and for sum of 20 ADC(Fig. 3.53 the average values of incoherent and coherent noise were obtained to be about 980 and 150 photoelectrons. The measured sensitivity of the counter is about 9800 photoelectrons/MeV. For such a sensitivity the energy noise equivalent is 100 keV for incoherent noise and 16 keV for coherent noise.

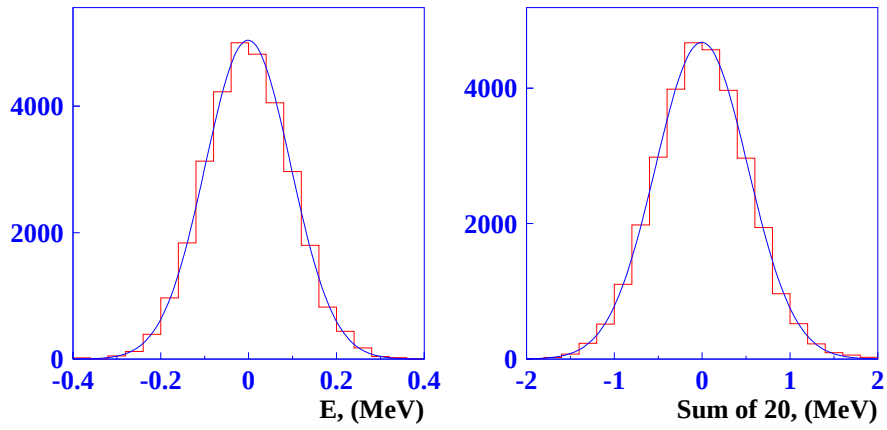

Figure 3.53: Pedestal width.

A trigger causes record of 2×256 words per each channel. Most of the measurements correspond to pedestal values except for cases where an energy deposition in the counter occured we observe the signal(Fig. 3.54). The measurements in the signal region after subtraction of the pedestal value are fitted by the function:

$$F(t) = A(t/\tau)^8 e^{-(t-t_0)/\tau}(e/8)^8 \tag{3.5}$$

with two free parameters A - amplitude of the signal and t_0 – time of the signal, $\tau \approx 30$ns – is the shaping time. The amplitude A characterizes the energy deposition in the counter.

The energy calibration is based on the energy deposition of cosmic muons crossing the CsI counters. Figure 3.55 shows the cosmic spectrum of counter when the signal of amplitude greater than the threshold level (about 10 MeV) for crystals over and under the crystal to be calibrated.

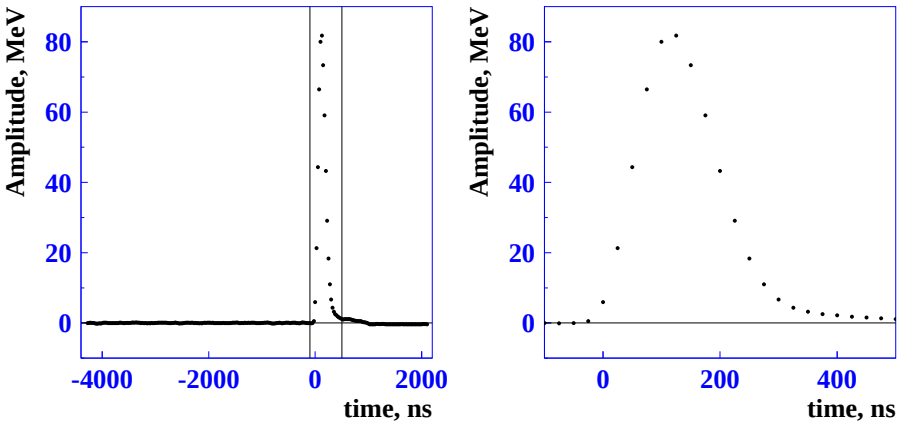

Figure 3.54: Signal time dependence in test beam studies of pure CsI crystals at BINP

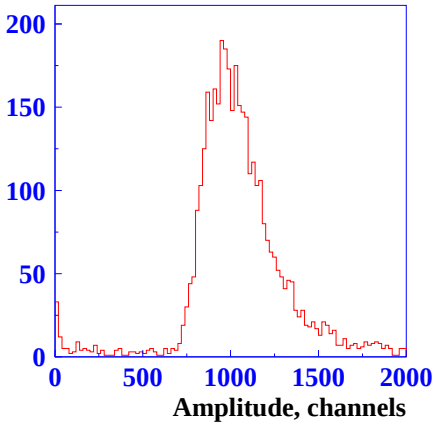

Figure 3.55: Amplitude spectrum from cosmic muons in test beam studies of pure CsI crystals at BINP.

From the peak position and the value calculated by MC we obtain the calibration coefficients c_i for energy reconstruction:

$$E_i = c_i A_i$$

where A_i is the amplitude reconstructed in the i-th crystal and E_i – is the energy deposition in this crystal.

The measurement at the test beam started at the end of December 2003 and will be finished at the beginning of February 2004. Measurements of the Compton spectrum with electron beam energies of 1.5, 1.85, 2.0,2.1,2.2 GeV have been performed. These energies correspond to the Compton edges of 76.5, 115, 134, 147 and 161 MeV, respectively. The trigger was the coincidence of the laser pulse, beam phase and plastic counter located behind the tagging system.

The Compton spectrum is shown in the Fig 3.56. The left edge is determined by the trigger acceptance while the right one corresponds to the maximum Compton spectrum energy. The CsI energy distribution is fitted by the convolution of the logarithmic-Gaussian function with

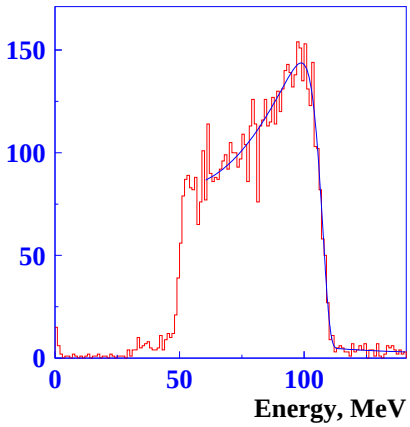

Figure 3.56: Spectrum of the backward scattered photons for E_{beam}=1.850 GeV measured in the 4x5 matrix.

free parameters

$$f(E) = N \exp(-\frac{1}{2\sigma_0^2} \ln^2(1 - \frac{E - E_p}{\sigma_E}\eta) - \frac{\sigma_0^2}{2}) \tag{3.6}$$

and Compton distribution that was approximated by the function:

$$f(E) = N\{(E - \frac{E_C}{2})^2 + \frac{E_C^2}{4}\},$$

were E_C is the energy of Compton spectrum edge.

The energy resolution obtained is shown in Fig. 3.57 together with the MC expectation. The MC was performed with electronics noise of 0.1 MeV/channel without taking into account

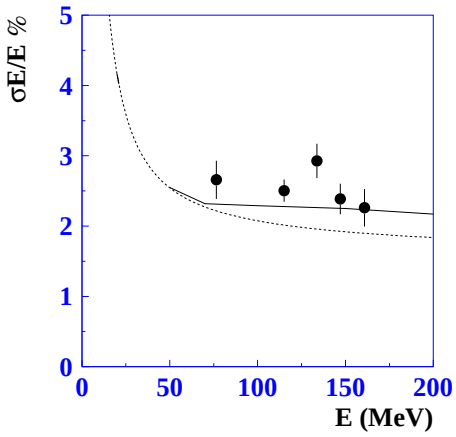

Figure 3.57: Energy resolution of a 4x5 matrix. Points are the measured value, the solid line is the MC expectation, the dashed line is the energy resolution approximation obtained with 5x5 CsI(Tl) crystals.

nonuniformity of the crystals. The obtained energy resolution is close to MC expectation. In the

same plot we also show the energy resolution obtained at test beam with 5×5 CsI(Tl) crystals. The slight difference in the energy resolution is due to the staggered geometry of the pure CsI crystal array.

Fig. 3.58(a) shows the difference between the time reconstructed in the crystal with the highest energy deposition and the trigger time from the beam phase. The dependence of the time resolution on the energy of the cluster is presented in Fig. 3.58(b). As one can see a time resolution better than 1 ns is obtained for the clusters with energy larger than 20 MeV.

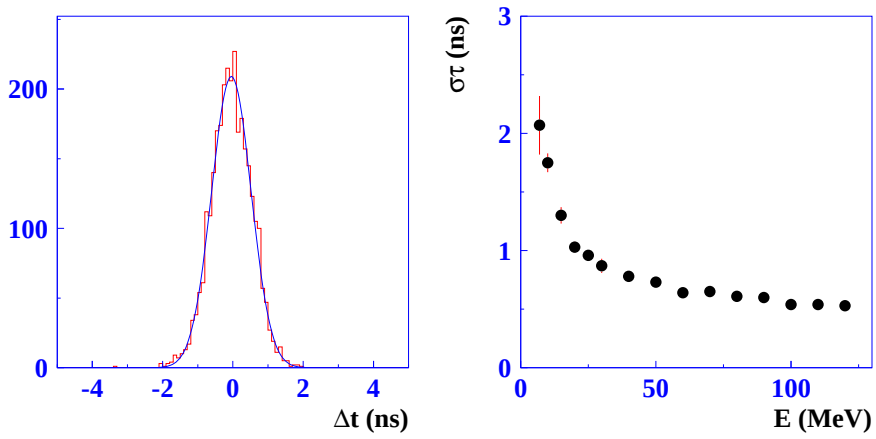

Figure 3.58: a)Distribution of the difference of the trigger and reconstructed time for E_γ=100 MeV. b)Dependence of the time resolution on the cluster energy.

The electronic noise will increase by a factor of 3 in the magnetic field due to the gain factor reduction, However an electronic noise level of 300 keV per channel is still acceptable if it is combined with pile-up supression. The test beam is still in progress. We plan to carry out measurements of the bremsstrahlung edge to check the linearity of the electronics for 1.5 GeV energy deposition and simulate pileup noise with ^{60}Co and ^{137}Cs sources. The recorded data will be used to develop and optimize the energy reconstruction algorithm for the case of a pipe-lined readout.

3.6 KLM

3.6.1 RPC option for the KLM endcap

Although it would appear that RPCs in the KLM endcap are not viable in a high luminosity environment, we explore the possibility that steps can be taken to reduce their exposure to background neutrons and thereby maintain their high efficiency operation.

Monte Carlo simulation shows that soft neutrons can be shielded effectively with a low-Z material. For example, a factor of four (or 100) reduction is achievable with 15 (or 50) cm of paraffin. Given the scaling with currents and luminosity, it is conceivable that the endcap RPCs could continue to operate with this additional shielding. The difficulty with this approach is the limited real estate where such shielding could be installed. One possibility is to replace the unused layers #12 and #13 RPC superlayers with paraffin sheets (8.6 cm total), and then place additional paraffin outside the yoke (and inside the concrete shield). This approach could be tried in a phased manner (e.g., replacing the RPCs in layers 12 and 13 of forward endcap quadrant 3 with paraffin) during a lengthy shutdown, e.g., in summer 2004 and/or summer 2005.

Another approach under study at Osaka City University is the use of a new gas mixture that itself quenches the streamer so that the glass plates are not completely discharged in the vicinity of the ionizing particle that forms from a neutron scattering event. This leads to a shorter effective recovery time for the existing RPCs and, thereby, a much shallower efficiency drop with increased hit rate. One promising combination is Argon, butane, HFC134A, SF6, and Helium in the proportions 28 : 18 : 20 : 2 : 32. The signals are somewhat smaller (by a factor of 4) and require an operating electric field of $\sim 4.5\,\mathrm{kV/mm}$, but can still be digitized with the existing electronics.

3.6.2 Scintillator option for the KLM endcap

An alternative approach for the endcap KLM, where the rate effects are most deleterious, is the replacement of the RPCs with a new and faster scintillator-based detector that would provide comparable—or better—information for muon tracking and K_L meson detection.

In the proposed system, all existing 14 gaps in the magnet yoke are used. Each superlayer in every gap is formed by two independent scintillator planes. We consider two options for scintillator geometry in each plane: strip or tile shapes. The independent operation of two planes that form one superlayer should reduce considerably the combinatorial background in comparison with the present RPC design where every background hit produces signals on both readout planes. In the tile option, the backgrounds are further suppressed as the occupancies per scintillator tile are much smaller—at the expense of a significant increase in the number of channels. Further background reduction can be achieved by using faster electronics, taking advantage of the short resolution time of the scintillator detectors. We assume the integration time to be 50 nsec.

Photons from the scintillator are collected by a WLS fiber and can be detected with the novel avalanche photodiodes in the Geiger mode (GPD) recently developed in Russia or with the more conservative option of multichannel photomultipliers (PM). Extensive experience on scintillator strips with the WLS fibers and PMs has been obtained by the MINOS collaboration [38]. The Number of photoelectrons (*p.e.*) permits efficient ($> 99\%$) MIP detection for 3 m long strips. Thus the scintillator strip with WLS fiber technique can be considered as established in case of PM photon detection. However, because of significant residual magnetic field in the iron gaps, this option requires substantial effort to transport the light to the field-free region outside the KLM, where the light can be detected by PMs. Both photodetector options have much smaller

dead time in comparison to RPC and thus no significant drop of efficiency due to the high background rate anticipated at SuperKEKB.

Scintillator strip geometry

In the present endcap RPC design, an r–ϕ geometry is used for the readout of the cathode strips. For the innermost layers, this geometry has the advantage of distributing the background hits more uniformly across the strips, since the r-measuring strips at smaller radius—where the occupancy is highest—are also shortest. In contrast, scintillator production technology limits us to straight strips. Therefore, we propose an x–y geometry, with the strips in the two scintillator planes of a superlayer aligned perpendicular to each other.

The system consists of 17,250 scintillator strips with the WLS fiber readout. One KLM module represents one quadrant placed in a gap between the iron absorbers. It consists of two scintillator strip planes as shown in figure 3.59, separated by an aluminium sheet and aligned along the x and y axes. The strips have a cross section of $1.2 \times 4\,\mathrm{cm}^2$ and a length of up to

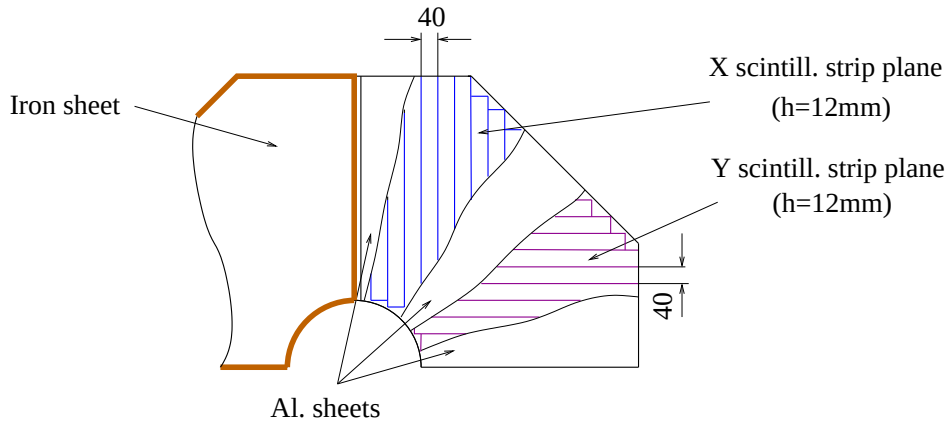

Figure 3.59: *Layout of the scintillator strip module.*

280 cm. (See Fig. 3.60.) Individual strips have a reflective cover (made by the 3M Corporation). The strip has a groove in the center to accommodate a WLS fiber. The fiber can be glued to the groove with optical cement: this increases the light collection by about 30%. However, the long term stability of glue transparency has yet to be established.

Several types of scintillator have been tested. Bicron BC-408 scintillator gives almost double the light yield of SCSN-81 and Russian scintillators made in Vladimir and Protvino, but is an order of magnitude more expensive; we reject it for this reason. The Russian scintillators provide enough light for efficient detection of MIPs, as will be shown below. Granulated polystyrene can be used as a base material with two dyes (1.5% of PTP and 0.01% POPOP). The strips can be produced by extrusion or injection moulding. In the latter case, the strip length is limited by the mould to about 50 cm; longer strips are made by gluing these end to end. Measurements show that the drop in light yield across the joint is only 10% or so.

Two types of WLS fibers have been tested at ITEP: Kuraray multicladded Y11 and Bicron BCF-91A,92. The former is a better match to our application, since it provides 40% more light and has a longer attenuation length ($\lambda > 3\,\mathrm{m}$), which is critical for long strips.

The radiation load at SuperKEKB is expected to be too small to cause any damage to scintillator or WLS fibers. Nevertheless, long term aging tests for the components of the chosen strip technology will be undertaken in the nearest future. We are encouraged by the observation

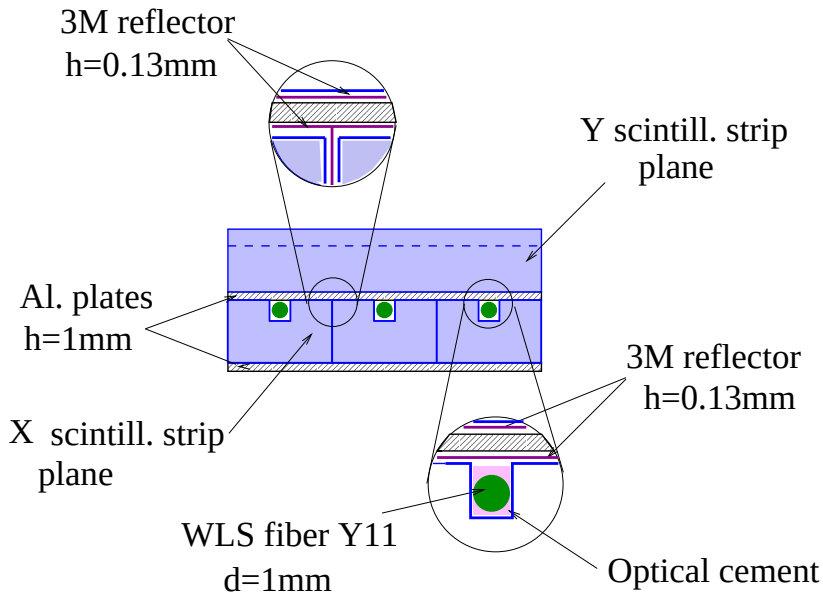

Figure 3.60: *Cross section of a scintillator strip superlayer.*

of no ageing effects over a three year period in the Vladimir scintillator and Kuraray WLS in the HERA-B shashlyk type electromagnetic calorimeter [40] (containing 91,000 Kuraray multi-cladded Y11 1.2 mm diameter WLS fibers bent in the middle to a radius of 14 mm).

Scintillator tile geometry

Two scintillator planes in a superlayer can be also made out of scintillator tiles, with those in the first plane shifted in both directions by half the tile size relative to those in the second plane. (See Fig. 3.61). The effective granularity in this case is one quarter of the tile size. One possible WLS fiber and photodetector arrangement is shown in figure 3.62.

This geometry has two advantages over the strip geometry. First, the random coincidence rate between overlapping elements in the two scintillators planes of a superlayer is reduced drastically by the smaller overlap area. Second, the light collection efficiency is increased, allowing for a better separation of signal from the abundant intrinsic noise in a GPD-like photodetector.

Different WLS fiber shapes have been investigated: a straight fiber at a tile side and in the center, diagonal and quarter of a circle fibers. The last two provide an acceptable light yield and uniformity. However, the circular fiber provides the highest light yield and the best uniformity. Figure 3.63 shows the light yield uniformity in a $16 \times 16\,\mathrm{cm}^2$ tile with a circular WLS fiber. It is flat within $\pm 5\%$ except in the region where the WLS fiber exits the tile. If necessary, the efficiency increase in this region can be reduced by shortening the fiber length.

As for the strip option, the Vladimir scintillator can be used to produce tiles. Also, the Kuraray Y11 MC WLS fibers are a better match to our application than the Bicron BCF-92 fibers, because of the 40% greater light collection efficiency and the better immunity to loss of light yield upon bending of the fibers into a 22 mm-radius circle (6% vs 25% for Y11 vs BCF-92, respectively). The bent Y11 fibers do not show any ageing after three months. (To repeat, no deterioration was observed in the bent fibers of the HERA-B calorimeter over a three year period.) In contrast, some samples of the bent Bicron BCF-91A WLS fiber demonstrated rapid ageing over the course of a few days.

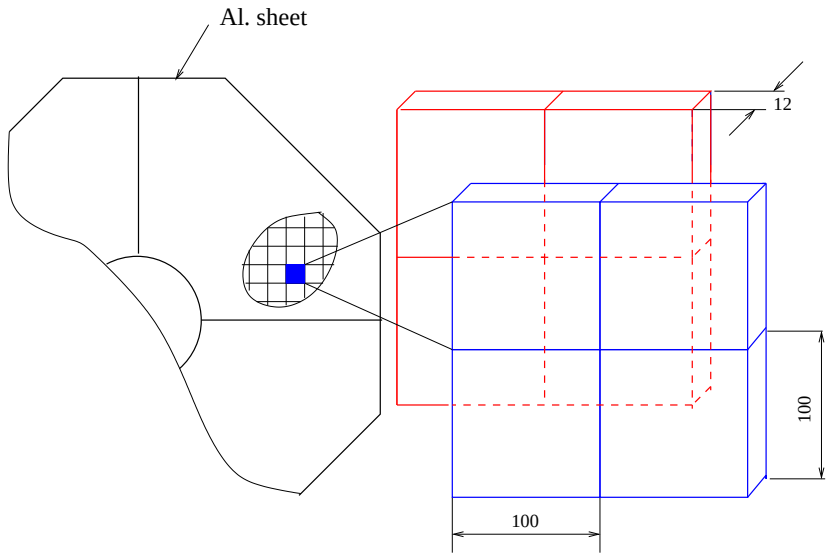

Figure 3.61: *Layout of the scintillator tile module.*

We conclude that the tile option is also feasible. It provides a larger photoelectron yield and better random background suppression than the strip option but requires larger number of channels. This number can be controlled at the expense of a slight decrease in the granularity.

Photodetectors

Several photodetectors can be used for the WLS fiber readout. In this proposal, we discuss only two examples: a silicon photodiode working in Geiger mode (GPD)—a novel detector that is being developed in Russia [41, 42] and the more conservative option of a multichannel PM.

A GPD is a matrix of 576 $42 \times 42\,\mu m^2$ silicon photodiode pixels working in the Geiger mode (see figure 3.64). There exist several variants with different number of pixels and/or depletion region thicknesses. The signals from all pixels are summed up to produce the GPD response. Each hit pixel produces a standard signal with an amplitude that depends on the diode capacity and bias voltage. A typical amplification is about 10^6. The output signal is proportional to the number of photoelectrons as long as this number is small in comparison with the number of pixels in GPD. Signals with n photoelectrons are well separated from those with one more or less. The spectral sensitivity of the GPD matches well a typical WLS fiber spectrum. The geometrical efficiency of the GPD is presently about 25%, and can be increased to about 40% in the future. The product of quantum and geometrical efficiency is 10–15% for wavelengths near the WLS fiber's spectral maximum [42]. This is comparable to the quantum efficiency of a typical PM, and will be further improved. Finally, the GPD can work at much higher rates than the required 10^4 Hz.

The GPD has several advantages over the multichannel PM. The GPD is tiny and can work in a strong magnetic field. Therefore it can be placed at the WLS fiber end, avoiding the complication of light transport to the outside via clear fibers. The GPD is expected to be cheaper than one channel of a multichannel PM. There is no cross talk problem and no large variation in response from channel to channel. Twenty GPDs have operated successfully during 1500 h each without failure, which sets the lower limit on GPD operating time of about three years. This test is ongoing.

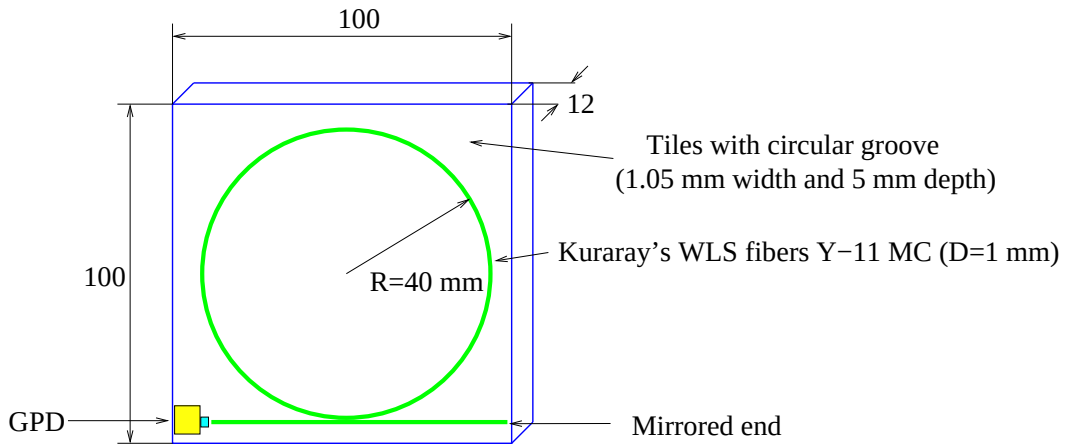

Figure 3.62: *Scintillator tile.*

However, the GPD has some disadvantages. It has quite a high single photoelectron noise rate, about 1 MHz at room temperature. In order to reduce this to an acceptable level, one must set the threshold at a few photoelectrons. The consequence for the strip geometry is that one long strip must be read out by two GPDs placed at the two ends, or that the strip must be segmented into shorter lengths with one GPD per segment. The few-photoelectron threshold has no impact on the tile option because of the high photoelectron yield.

We can conclude that GPD is a very attractive choice for photodetection. This device is still in the R&D stage and several tests still have to be performed. Even so, the mass production of suitable GPDs can be started within a short time scale.

The multichannel PM is a well proven device that is completely adequate for our application. Hamamatsu's R5900 64-channel PM is the most cost effective solution [43]. Each individual channel of this PM can work at a rate of 3×10^7 Hz of single photoelectron pulses with a gain of 5×10^5. This is three orders of magnitude larger than the expected background rate of about 10^4 Hz per strip. It is expected that the background is dominated by few-photoelectron signals. The lifetime of PM at the background rates of 10^4 *p.e.*/sec is above 200 years. The quantum efficiency is about 13% at the peak output wavelength of the WLS fiber. It is practically identical to the quantum efficiency of R5900 M16 PMs, which are used by the MINOS Collaboration and provide a sufficient number of photoelectrons.

There are, however, several drawbacks. First, these PMs cannot work in Belle's strong magnetic field, so the scintillator light has to be transported via clear fibers to a field-free region. Second, there is considerable cross talk between neighboring PM channels. The cross talk to all neighbor channels is about 8%, even if the fiber is positioned at the center of a $2 \times 2\,\mathrm{mm}^2$ cell, resulting in apparent ghost hits in the scintillator strips mapped to those neighboring PM pixels—which may correspond to either adjacent or faraway scintillator strips. If a ghost hit appears in an adjacent strip, the position resolution is degraded; if it appears in a faraway hit, a ghost coincidence with the orthogonal strip in the other plane of the superlayer results. Finally, there is a large difference in gain (up to a factor of 3) among individual channels. Of course, this difference can be compensated by preamplifiers with adjustable gain. In spite of these drawbacks, R5900 M64 PMs are adequate and ready for use in this application.

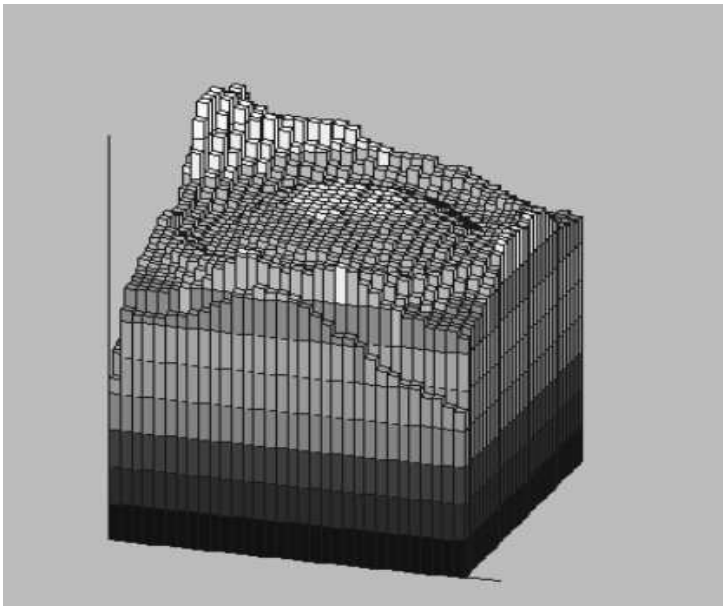

Figure 3.63: *Spatial uniformity of the light collection efficiency in a* $16 \times 16\, cm^2$ *tile.*

Results of R&D tests

The signals from a GPD obtained with a random trigger are shown in figure 3.65*a*. The pedestal position is around 60 *ADC* channels, smeared by the preamplifier noise. Peaks near 75 and 90 *ADC* channels correspond to one and two photoelectrons. Each photoelectron produces an additional primary electron in the GPD with a probability of about 20%, which we call internal GPD cross-talk. The noise spectrum has been measured in detail for different operating voltages. The GPD noise rate *v*s. threshold is shown in figure 3.66. The plateaus correspond to the thresholds of one, two, three, or more primary electrons. Events with more than one primary electron are due mainly to internal GPD cross-talk. The threshold value required to suppress noise to an acceptable level depends upon the operating voltage. The optimization of GPD cross-talk, operating voltage and light collection efficiency is a subject of ongoing R&D.

The GPD outputs were calibrated using photons produced by a light emitting diode (LED). The signals from one GPD–LED setup is shown in Fig. 3.65*b*. The *ADC* distribution is fit by a sum of eight equidistant Gaussians (each describing the contribution for a particular number of photoelectrons) and an one more Gaussian for the pedestal: $\sum_{i=1}^{8} f_i G_i + f_0 G_{ped}$. The width (standard deviation) of the i^{th} Gaussian is set to be proportional to $\sqrt{i}$. The fitted areas f_i of the photoelectron Gaussians are found to follow a Poisson distribution convoluted with a 20% smearing due to cross-talk.

Finally, a $1.0 \times 2.5 \times 200\,\text{cm}^3$ strip equipped with two GPDs, one at each end of the WLS fiber, was tested at ITEP. We used a cosmic ray trigger based on two small external scintillator counters in coincidence. The strip was scanned along its length by varying the distance between the trigger counters and each of the strip ends from 5 to 195 cm. The signals from one GPD, with the trigger counters placed in the middle of the strip, are shown in Fig. 3.65*c* as an example. The sharp peak on the left side of the figure corresponds to the pedestal, recorded during random coincidences in the trigger counters.

The mean of the Poisson distribution from a throughgoing minimum ionizing particle (MIP) at normal incidence varies from 10 to 5 photoelectrons per GPD when the trigger counters are

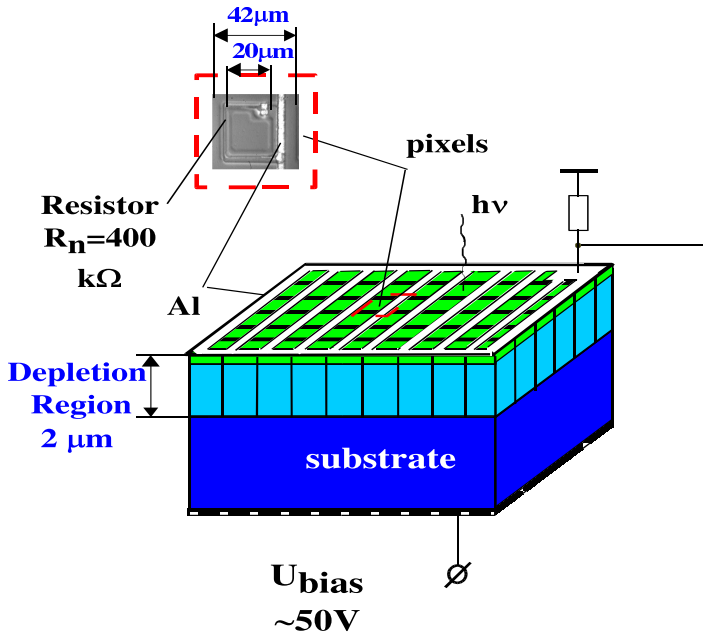

Figure 3.64: *A schematic view of a GPD.*

placed at the near and far end, respectively, of the scintillator strip, as shown in Fig. 3.67. The mean of the two-GPD Poisson distribution is shown in the same figure with open circles; it is quite flat and exceeds 12 photoelectrons at every position. A Monte Carlo study shows that amount of light collected for a $1.0 \times 4.0\,\mathrm{cm}^2$ strip will be about 25% smaller, corresponding to a two-GPD signal mean above 9 photoelectrons. From the above study we conclude that a threshold of 4.5 photoelectrons will reduce the noise rate to under 10 kHz per strip while keeping the efficiency for a MIP, averaged over the strip length, above 98%. Another new type of GPD which we are testing now, has considerably smaller intrinsic cross-talk with comparable efficiency. With this device, it will be possible to decrease the threshold to 3.5 photoelectrons with a noise rate below 2 kHz and thereby raise the efficiency to above 99.5%.

The tile option was also tested in the framework of the calorimeter ECFA/DESY R&D study. About one hundred scintillator tiles with WLS fibers and GPD photon detectors have been produced and tested by an ITEP-MEPhI team. The tile size was $0.5 \times 5.0 \times 5.0\,\mathrm{cm}^3$ and the fiber had a circular shape with a radius of 2.2 cm. The two large faces were covered with 3M reflector, and the four small faces were treated chemically to provide a diffuse reflection and optical separation between tiles. The average number of photoelectrons was above 20 with a triggered ^{90}Sr source, which emits electrons that are similar to MIPs. (See Fig. 3.68). The system demonstrated stable performance during several months of tests in an electron beam at DESY.

3.6.3 Performance

The scintillator KLM can work efficiently at background rates 100 times larger than the present one. It has much lower sensitivity to background than RPC. A background neutron (or soft photon) is absorbed in one scintillator strip or tile, so there are no two dimensional hits from single background particles. This is in contrast to RPC, where a single neutron (or soft photon)

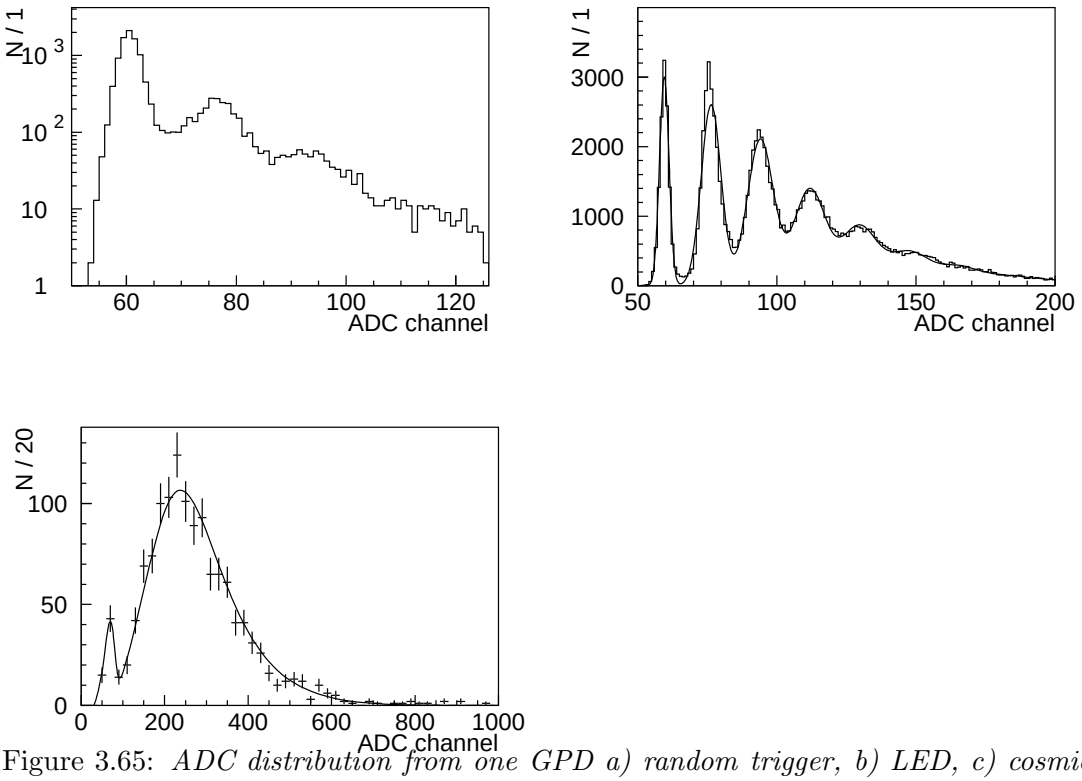

Figure 3.65: *ADC distribution from one GPD a) random trigger, b) LED, c) cosmic run with the trigger counters placed in the middle of the strip.*

produces a two dimensional hit.

Scintillator counters are typically more sensitive to neutrons than RPCs, although the ratio of sensitivities depends strongly on the neutron energy spectrum. Gaseous detectors without hydrogen in the active volume are mainly sensitive to photons produced by neutrons [44]. This results in a cathode strip chamber sensitivity of about 0.5% for a neutron spectrum typical for hadron colliders. In our RPCs, the sensitivity must be higher because of the large fraction of butane in the gas mixture. Scintillator efficiency for such neutrons is in the few percent range. To be conservative, we assume that the scintillators will be ten times more sensitive to background neutrons than RPCs. Direct measurements at Belle of background using scintillator counters with WLS fibers and GPD photodetectors are in preparation now.

The rates of K_L candidates originating from random coincidences of background hits in independent planes of a superlayer are presented in table 3.10. The numbers are given for the

Table 3.10: *The numbers of KLM clusters per event originating from random coincidence of background hits in independent planes of a superlayer. The assumed flux of background particles is* 10^5 *Hz/m*^{2} *and time resolution is* 50 *nsec. Correlated background is not taken into account.*

	#layers ≥ 1	#layers ≥ 2
scintillator strip option	0.3	10^{-4}
scintillator tile option	0.01	10^{-8}

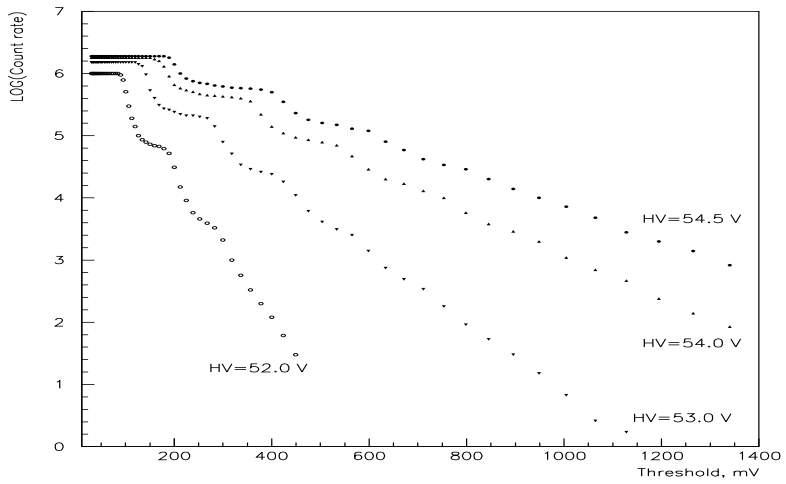

Figure 3.66: *GPD noise rate versus threshold.*

background hit rate of $2 \cdot 10^5\,\mathrm{Hz/m^2}$ (20 times higher neutron flux than the present one and 10 times higher sensitivity to neutrons of scintillator than of RPC) and for time resolution of 50 nsec. The KLM cluster is defined in a usual way. The random background rate is negligible, therefore we expect that the background will be dominated by consecutive scattering of the same neutron in adjacent counters. The corresponding rate has yet to be estimated.

Even at the present background level, the fraction of K_L candidates originating from background in the RPC KLM is considerable. Table 3.11 presents the rates of K_L candidates obtained from a Monte Carlo simulation of three event types: $B\bar{B}$, $B\bar{B}$ with background added and background only. The presence of background increases the rate of K_L candidates by 30% (last column in table 3.11), the main contribution coming from random coincidences of ECL clusters and KLM background clusters. The distribution of fake K_L candidates peaks in the highest occupancy region at large $\cos\theta$ as seen in figure 3.69.

Table 3.11: *The number of neutral KLM clusters per event obtained from Monte-Carlo simulation for $B\bar{B}$ events, $B\bar{B}$ events with background added and background events only. Background from experiment 13 is used.*

	matching ECL cluster	no ECL, #layers = 1	no ECL, #layers ≥ 2	matching ECL or #layers ≥ 2
$B\bar{B}$	0.18	0.73	0.19	0.37
$B\bar{B}$ + bg	0.34	2.4	0.23	0.56
only bg	0.003	1.8	0.03	0.03

In the present reconstruction algorithm, a neutral KLM cluster is considered as a K_L candidate if its number of layers is at least two or if there is a matching ECL cluster. Low background rate in the scintillator KLM suggests that one can consider also 1-layer clusters as K_L candidates (in case of the strip option the random rate can be further reduced by a requirement of more than one strip in a plane). The resulting increase in efficiency is about 20% for $P_{K_L} = 1\,\mathrm{GeV}$ and is even more pronounced at low momenta. The use of 1-layer clusters will add 0.7 fake K_L

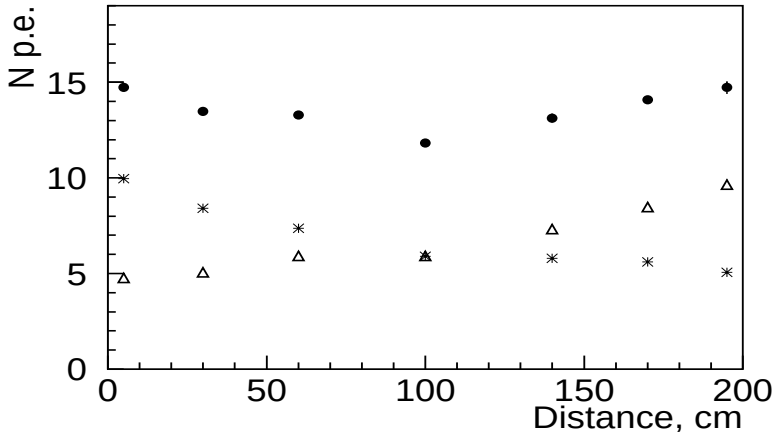

Figure 3.67: *The means of the one-GPD Poisson distributions (triangles and stars) and of the summed two-GPD Poisson distribution (circles) for a normally incident MIP as a function of position along the scintillator strip.*

candidate/event due to large angle tracks from hadron showers. This number can be reduced by reoptimization of the K_L reconstruction procedure.

As the proposed granularity is identical to the present one, while the efficiency of a superlayer is expected to be even higher than now, the muon identification is expected to be comparable to the existing one.

3.6.4 Conclusions

The present RPC technology can be used in the barrel part of the KLM detector. The background rate is projected to be 20 times greater in the innermost layer for a SuperKEKB luminosity of 5.0×10^{34} cm^{-2}s^{-1}, yet the efficiency will remain at or above 90%. (The better shielded outer layers of the barrel KLM are practically immune to the projected increases in currents and luminosity.)

A KLM detector based on scintillator counters with WLS fiber light collection can work efficiently at the background rates 100 times larger than the present one. This appears to be the best solution for the endcap KLM. This is a well established experimental technique in the case of multichannel PM readout. It is even more attractive and elegant with the GPD readout. However in this case some R&D is still required. A considerable amount of optimization and tests should be done for both strip and tile options.

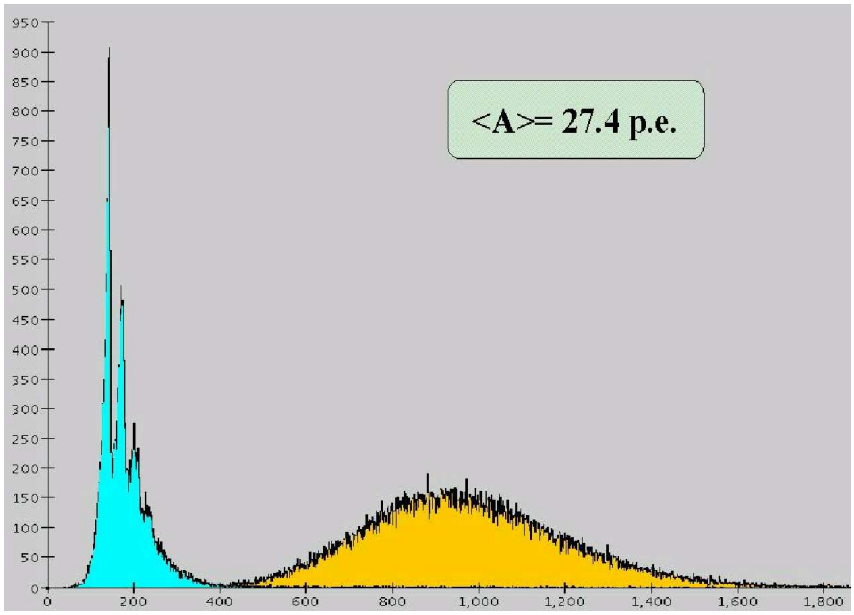

Figure 3.68: *Amplitude distribution for LED (open histogram) and triggered* ^{90}Sr *signals (hatched histogram) in* $0.5 \times 5.0 \times 5.0\, cm^3$ *tile.*

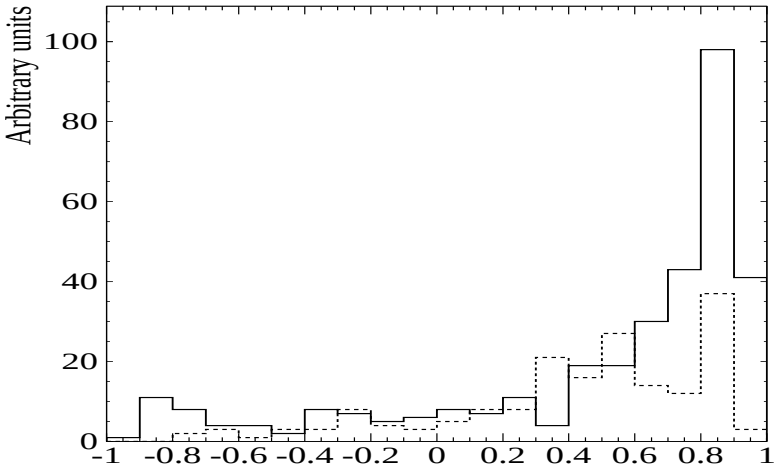

Figure 3.69: *The azimuthal angle distribution of the* K_L *candidates.*

3.7 Trigger/DAQ system

3.7.1 Overview

The trigger and data acquisition systems are designed so that the know-how in the current system at Belle can be utilized as much as possible. The design of the trigger system is basically unchanged from the current system. In contrast, the design of the data acquisition system is modified based on a pipelined readout scheme in order to cope with the high trigger rate more than 10KHz, with a low dead time. To reduce the manpower and cost for the system development, the usage of a common readout module is planned to handle the pipeline readout in a consistent way.

The scalability of the system is also an important issue in the design. It will take some time before the accelerator achieves design luminosity. We need a large processing power for the data reduction in the event building and level 3 trigger farms to obtain the required reduction rate, however, the full processing power for the maximum luminosity is not necessary at the beginning of the experiment. A DAQ design that can easily increase its processing power just by adding common units to the system is preferable.

Fig. 3.70 shows a global design of the data acquisition system. The details are discussed in the following subsections.

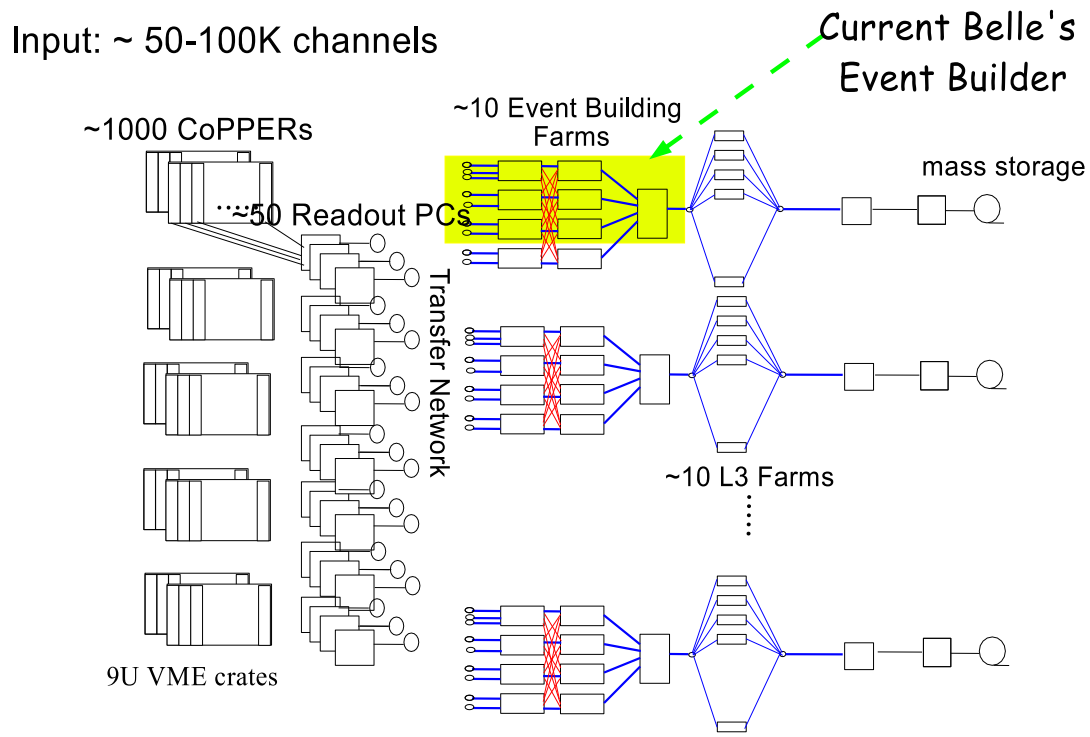

Figure 3.70: Global design of the data acquisition system for the Super KEKB experiment.

Figure 3.71: Schematic view of Global Decision Logic(GDL) stages. The final output from GDL is sent to SEQ.

3.7.2 Trigger

We keep the present scheme with minor modifications for the super KEKB experiment because of the successful operation of the present Belle trigger system. The sub-trigger systems are discussed in each detector section. Here we discuss the Global Decision Logic (GDL) that receives trigger information from sub-trigger systems and makes the final trigger decision. In Fig. 3.71, a schematic view of GDL is shown. All the stages are pipelined, and therefore it works without any dead-time. Inputs from the sub-triggers are fed into the input delay stage, in which the timing of all the signals from the sub-triggers are adjusted. The trigger decisions are made using the adjusted signals in next stage. The conditions for the trigger decision are programmable and will be discussed elsewhere. At the next stage, the pre-scaling will be made according to the type of the trigger decision to suppress the triggers for monitoring and calibration purposes. Bhabha events, for example, will be pre-scaled at this stage. The final stage in GDL is the timing decision. The timing of output signal of GDL is synchronized to the best timing source, which is selected event by event. The output signal is sent to the timing distribution logic.

3.7.3 Trigger Timing Distribution

The L1 trigger signal is distributed to every COPPER module and the *busy* signal is collected from them by the *Trigger Timing Distribution* (TTD) system, to synchronize the readout timing and order of the event fragments that are sent to the event-building farm. In order to coordinate more than a thousand COPPER modules, we designed a four-step cascaded distribution system using one-to-eight Trigger Timing Switch (TT-SW) modules, as shown in Fig. 3.72. The trigger signal is received by a master Trigger Timing Input/Output (TT-IO) module, and eventually distributed to the Trigger Timing Receiver (TT-RX) cards. The trigger signal is provided as an LVDS signal; other signals, including the event tag and abort flag to downstream and the busy and other errors to upstream, are encoded in a 10-bit serial-bus when transmitted and decoded when received. The serial bus is synchronized with a system clock of 42.33 MHz (1/12 of the RF clock). Since the serial bus is driven with a clock 12 times faster (including start and stop bits) of 508 MHz, the module has to be carefully designed; still it is possible to use a standard CAT5 unshielded twisted pair (UTP) cable up to about 10 m. The TT-SW and TT-IO modules are VME 6U modules. The TT-RX module is a PMC daughter card to be attached onto the COPPER.

3.7.4 Readout Subsystem

A readout subsystem consists of a set of modularized common readout platforms called COPPER. One COPPER module is a single VME 9U board with digitizers, a trigger timing receiver(TT-RX) and a CPU module used for the on-board data processing. These components are also modularized and implemented as daughter cards on a COPPER module. The digitizer modules are called FINESSE modules and various types of FINESSE modules can be implemented according to the requirements of each detector. The modules are equipped with a L1 pipeline

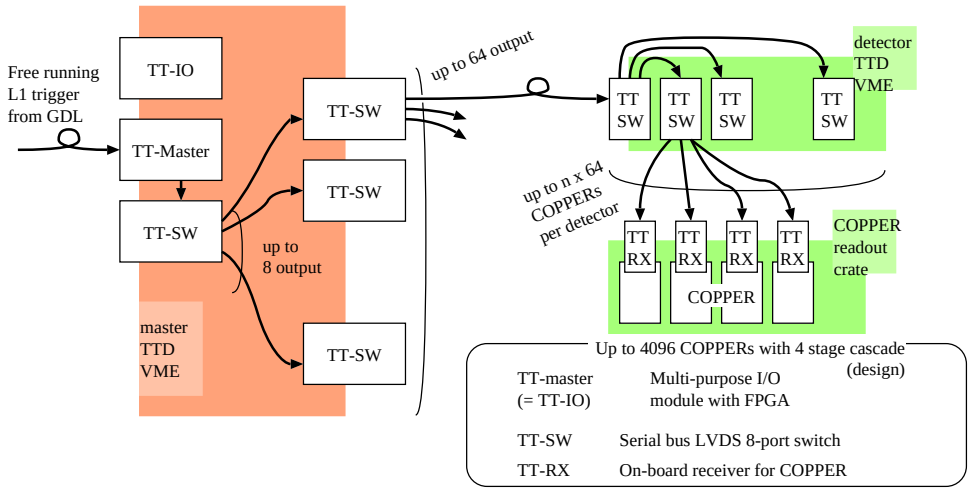

Figure 3.72: Cascaded trigger timing distribution.

FIFO so as to record the digitized signal without readout dead time. The CPU module is a commercially available PMC module and can be easily upgraded to use an up-to-date CPU to increase the processing power. Detailed descriptions of FINESSE and COPPER are given in the following subsections.

Front-end Interfacing Module: FINESSE

The signal digitization is performed by FINESSE modules which are implemented as daughter cards on a COPPER.

Fig. 3.73 shows a block diagram of one FINESSE card. A FINESSE is a card with a size of $186.0 \times 72.5\text{mm}^2$. A FINESSE receives detector signals and performs digitization with an accuracy of up to 32 bits at the timing of the divided RF-clock rate. The digitized signals are continuously stored in the L1 pipeline. The pipeline consists of four groups of FIFO buffers that work as a ring buffer. Once the FINESSE receives an L1 trigger signal from the trigger timing logic(TT-RX) on the COPPER, the write pointer to a L1 FIFO buffer is switched to the next buffer to freeze the contents of the digitized data in the buffer. The data in the buffer are then transfered to a readout FIFO on the COPPER module. Upon receipt of the L1 trigger, each FINESSE asserts a *busy* signal to acknowledge the trigger whose duration is as short as the time to switch the pointer.

Common Readout Platform: COPPER

Figure 3.74 shows a block diagram of a COPPER module. A COPPER is a 9U-VME board equipped with four slots for FINESSE cards, event buffering FIFOs, and three mezzanine-PCI(PMC) slots.

Four readout FIFOs on a COPPER contain digitized signals of triggered events transferred from FINESSE modules. Each readout FIFO has a size of 1 MByte and is connected to a 32-bit local bus. Four local buses are merged into a 32-bit PCI bus via a bridge whose transfer rate is up to 133 MB/s.

Once the total amount of data in a FIFO exceeds a tunable threshold, a data transfer is initiated to the main memory of the CPU module by a DMA through the PCI bus . The

data processing on the CPU is performed utilizing the same software framework as that used in the offline analysis. The transfered data are first formatted so that they can be handled by the framework and then various data processing are performed in the framework such as pedestal subtraction, zero suppression, feature extraction from wave-form sampled data, and data compaction. The level 2 trigger processing is also performed. The event data which are vetoed by the external trigger signal received through TT-RX are discarded in the processing. The data are finally transferred to the event building farms through an on-board FastEthernet device.

Performance of Prototype Modules

We have studied the performance of the readout system using a prototype COPPER setup. A FINESSE card we used generates 0.2 kB fixed data upon every L1 trigger. In this study, the received data were discarded just after the DMA without any data suppression. The readout system kept up with the input trigger rate up to 28 kHz, which is close to the required performance. VME a We consider it is possible to gain the performance by replacing the CPU with much faster one and by tuning the threshold level of data amount in the FIFO to start the DMA.

3.7.5 Event Building and Level 3 Trigger Farms

The event building is done in three steps utilizing the switchless event building technology developed for Belle [59]. The digitized data in up to 20 COPPER modules contained 9U crate are first transferred to a readout PC via the socket connections on the 100Base-TX network. A network switch is used to share network interface ports on the PC, although the connection between a COPPER module and the PC is a port-to-port basis and the switch is transparent. The same event building software currently being used at Belle runs on a PC and combine the data fragments from the COPPER modules.

The remaining steps of the event building are done on multiple units of the event building farm one of which is basically the same as that used at Belle. To distribute event fragments from a readout PC to multiple units of event building farms, a network matrix is used as shown in Fig. 3.75. Another network interface on a readout PC is connected to a network switch equipped with a number of ports corresponding to event builder units, and event fragments from a readout PC are sent to multiple event building units sequentially in turn. The fragments are received through a receiver-side network switch connected to a network interface on a layer 1 server of each event building farm.

After event building is completed on the event building farms, the events are fed into the level 3 trigger farms. One unit farm consists of 30 to 50 processing servers and servers to distribute and collect events. A unit of an event building farm and a level 3 trigger farm is designed that they can process the event data flow for a luminosity of $10^{34}\mathrm{cm}^{-2}\mathrm{sec}^{-1}$ and the number of units is increased to keep up with the accelerator luminosity at the moment. A full event reconstruction is performed on the farm and the level 3 event selection is made. The selected events are sent to the offline computing facility via a couple of 10 Gigabit Ethernet network optics and recorded onto multiple disks in parallel.

3.7.6 Event Reduction

Event reduction is one of the key issues in the design of the data acquisition system. To achieve as large a reduction factor as possible in an efficient way, event reduction is done at each step

of the event building. The first reduction is the level 2 trigger, which is done on COPPER modules. The level 2 trigger information is received through the timing distribution logic and the vetoed events are discarded by the software running on the COPPER module. By using the SVD z trigger signal as the level 2 trigger, the trigger rate at the COPPER output is expected to be less than 10kHz. On the COPPER modules, further event size reduction is also performed by feature extraction and software compaction of the data. The additional processing for the event reduction is also performed on the readout PC. The total event size after this processing is expected to be less than 100KB/event.

The level 2.5 trigger processing is done on the event building farm utilizing partially-built event data. An algorithm similar to that used at Belle will be employed. Very fast tracking software can reject the beam-gas events where the vertex is displaced from the interaction point. The trigger rate after the level 2.5 trigger is expected to be less than 5KHz.

The final reduction is based on full event reconstruction on the level 3 trigger farm. The same event selection that is used in the offline analysis is used as the level 3 trigger software. Hadronic events and $\tau\overline{\tau}$ events are selected. About 25% of level 2.5 triggered events are selected and therefore the event rate after level 3 is expected to be less than 1.5KHz. By the multi-step event reduction discussed above, the final data flow at storage is expected to be kept less than 250MB/sec.

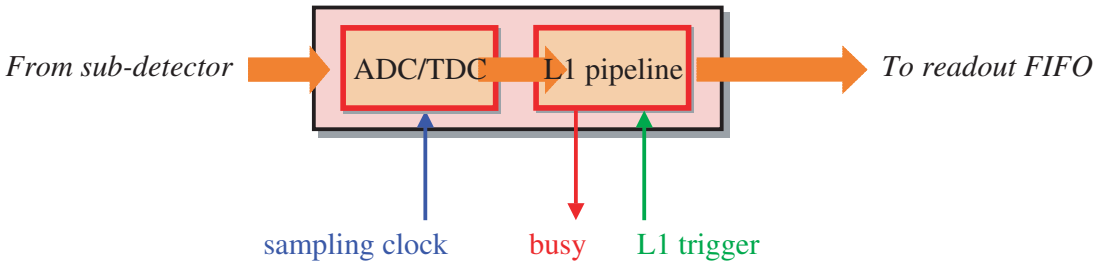

Figure 3.73: The typical block diagram of one FINESSE card. The digitized signals from the ADC or TDC are stored in the L1 pipeline to minimize deadtime due to trigger latency.

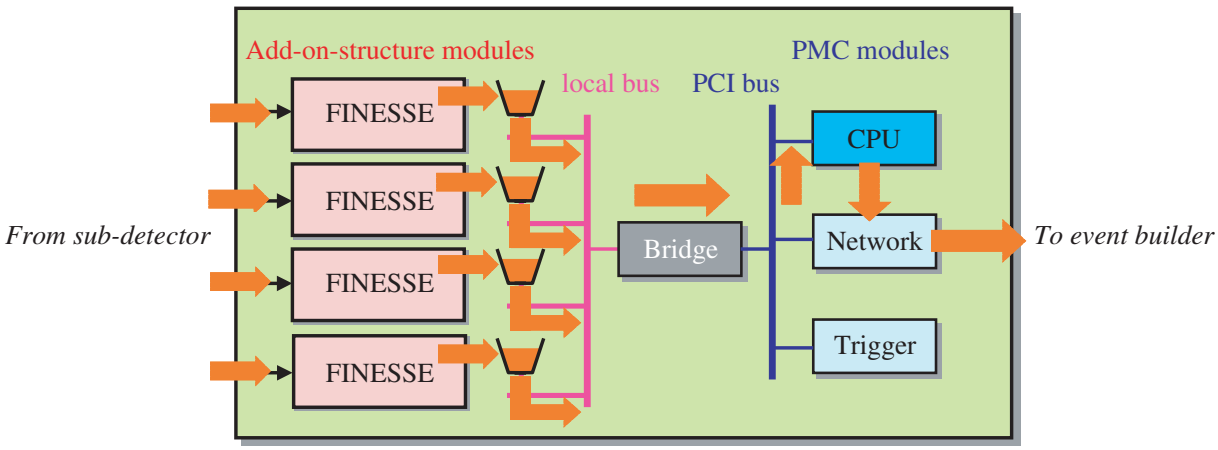

Figure 3.74: The block diagram of the COPPER board. Red arrows indicate the data flow on the COPPER.

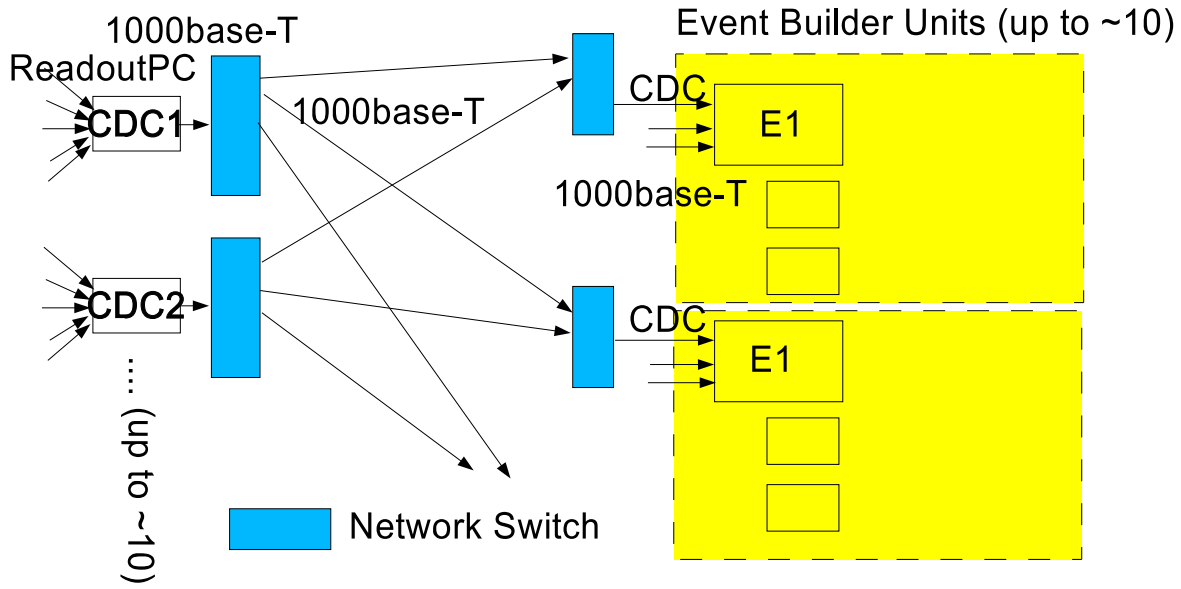

Figure 3.75: The event building network matrix.

data type	data size(TB/year)
hadronic events	100
τ-pair events	25
two photon events	30
calibration skims(μ-pair/Bhabha/hadronic)	1000

Table 3.12: Expected data sizes for typical event samples. Here 1 year corresponds to 200 days and 10 fb^{-1} of beam data is accumulated in a day at a luminosity of 10^{35}.

3.8 Computing

3.8.1 Requirements for computing at Super KEKB

With a luminosity of 10^{35} $cm^{-2}s^{-1}$, online data have to be recorded at a speed of 250 MB/sec after online reconstruction and reduction. Assuming that we take data for 2×10^7 seconds per year, this corresponds to the data size of 5 PB/year. After event reconstruction, we would like to keep skims, each of which is a starting point for detector calibration and physics analyses. Extrapolating from the present conditions, we need 1 PB/year capacity to keep skims for detector calibrations such as μ-pairs and clean hadronic events. For physics analyses, the data size of compressed hadronic events is estimated to be 100 TB/year. In addition to this, MC event samples have to be kept on disk and MC statistics should be at least 3 times larger than that of beam events, suggesting that at least 700 TB/year should be provided. Note that MC events are larger than beam data events as they contain generator information.

Table 3.12 summarizes the data sizes for typical skims. Here calibration skims will be kept only for 6 months. In total, we need about a 10$\sim$20 PB storage system at the beginning of the Super B experiment, and it should be expandable up to several tens of PB as we take data.

For CPU power and other resources, we would like to satisfy the following requirements:

- Beam data must to be reprocessed, if necessary, in a couple of months. From our experience, this is very important because we can obtain new and better physics results when a break-through in software is made. Any major improvement in software should be applied onto all data to produce a consistent data set and physics analyses must be repeated as soon as possible. We have given this condition the first priority in the Belle computing so far and it has allowed us to obtain important new physics results in a timely fashion.

- A MC sample at least 3 times larger than the beam data has to be generated. This is also essential to control systematic errors in the experiment and estimate backgrounds precisely in many analyses because user analyses have already matured at the present level of statistics, and further beam data will push us to reduce systematic error. To make this possible, a huge MC sample is indispensable.

In the next couple of years, it is expected that LCG will deploy the GRID technology for the LHC experiments [56] and could standardize it for other High Energy Physics experiments in the world. The vendor's trends should also be carefully observed when selecting our computing technologies. In particular, long range support for the chosen technologies by vendors is very important.

In what follows, computing components to realize the above requirements will be discussed.

vendor	drive technology	transfer rate(MB/s)	tape volume(GB)
IBM	LTO	35	200
StorageTek	T9940B	30	200
SONY	SAIT	30	500

Table 3.13: Possible options at present for the mass storage system.

3.8.2 Storage system

SONY has decided to stop development of the DTF tape technology. Thus we have to switch to a new tape format to keep the data. For the mass storage system of PB scale, three tape based options available in the market are listed in Table 3.13. Three vendors have given us their roadmaps for the coming several years showing a data transfer speed of 240 MB/s is possible in 2008. The PowderHorn from StorageTek has been installed and operated in several laboratories in High Energy Physics. The SONY SAIT tape, on the other hand, is relatively new and SAIT tape volume capacity of 500 GB allows us to reduce space needed for a robotic tape device. The choice has to be made by considering several aspects in hardware and software as well as cost and expandability.

We need a disk storage system with a capacity of at least several PB to keep data for users easily accessible. One key issue is how to configure disk system from hard disks that are commercially available. One possibility is to construct a large disk device using a SAN (Storage Area Network). In the future, SAN technology may be used to form a PB-scale disk system connecting a bunch of one TB disks with fiber channel technology. Users can access any data located in this SAN system without knowing the actual location.

The other is to construct compute-storage PC farms from 10 K PC's where each PC is equipped with 500 GB $\sim$ 2 TB local disk space. The advantage of this option is that the data are naturally distributed over 10 K PC's and this decentralization can avoid heavy traffic when accessing the data. In this system, it is easy to expand the system and it can be cost-effective.

Details of the storage device configuration will be given in the computing model section.

3.8.3 CPU

In our experience, we can process 1 fb^{-1} of beam events per day with 60 PC hosts equipped with 0.7 GHz quad Pentium III CPU's. This processing performance is limited only by CPU power. At a luminosity of 10^{35}, 10 fb^{-1} of data can be accumulated daily and to process those data, we need 10 times more CPU power, compared to the present system. In case we must reprocess 5 ab^{-1} of data in 3 months, 200 fb^{-1} of data have to be processed in one day, suggesting that we need 200 times CPU power than in the current system. Here we assume Moore's law will be valid in the coming several years and the CPU clock speed implemented in PC's available on the market with reasonable cost can reach 5 GHz in 2006. If we use PC's with 5 GHz dual CPU's, the number of PC's is estimated to be 3400. In addition, to produce MC events with 3 times more statistics of than beam data, we simply triple them. In total, we require about 14,000 PC's. If we can deploy faster CPU's, the number of CPU's can be reduced.

The CPU power for user analyses must also be increased because analysis techniques will become more complicated, and before arriving at final physics results, the user will have to perform more steps in her/his analysis procedure than current analysis to reduce systematic errors. We assume that a PC farm 50$\sim$100 times larger than the present one is necessary.

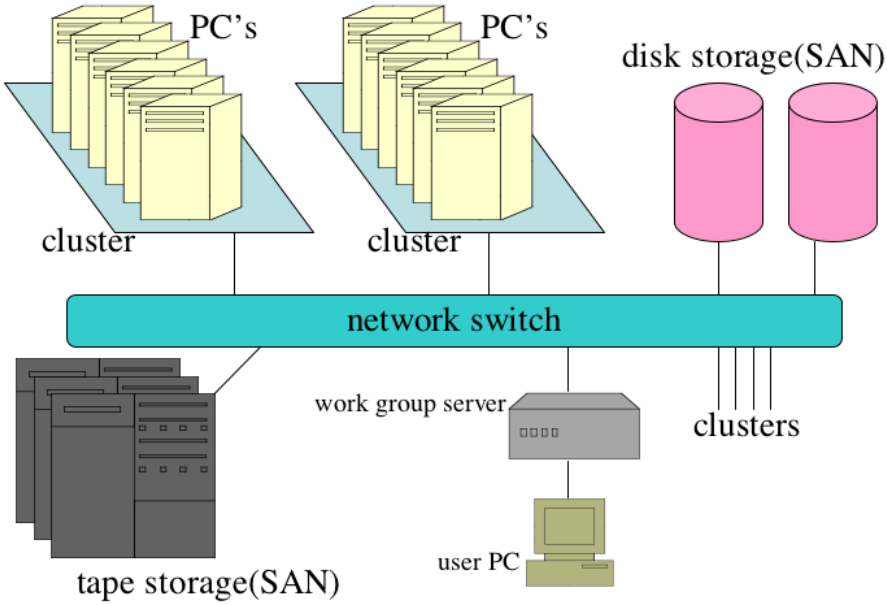

Figure 3.76: Conceptual drawing of computing model 1 for Super KEKB.

The arrangement of this number of PC's has to carefully be considered to avoid bottlenecks in network connections for data access, which may deteriorate computing performance.

3.8.4 Computing model

Here we describe two computing models as possible solutions to our computing demands.

One candidate is a natural extension of the current KEK B-computing system mentioned in the previous section. Figure 3.76 shows a conceptual sketch of this model. Large disk servers and tape library for storage may be connected to a principal network and PC's are configured as a bunch of clusters.

The other possbility is to equippe each PC with a larger capacity of local disk like 1 TB and then cofigure these PC's in a group of clusters as shown in Figure 3.77. In this case, 14,000 PC's are equivalent to a storage system with 14 PB of disk space. The capacity of the tape library system can be smaller; at least the number of tape drives can be smaller than in option 1 as the main purpose of the tape library is to archive the data.

For the second option, possible network traffic may not be so heavy since the data are a priori de-centralized. It will be easy for us to extend the system by adding CPU's and storage disks.

A configuration in the middle of the above two options can also be a solution and it may be necessary to optimize the configuration for price and performance.

3.8.5 Data bookkeeping and management

The data bookkeeping is very important especially for an experimental environment with a large amount of data. It should be made automatic as beam and MC data become available and excellent interface, preferably based upon a web style, should be provided. This database for the data bookkeeping must be managed as a core component in any software utilities that access

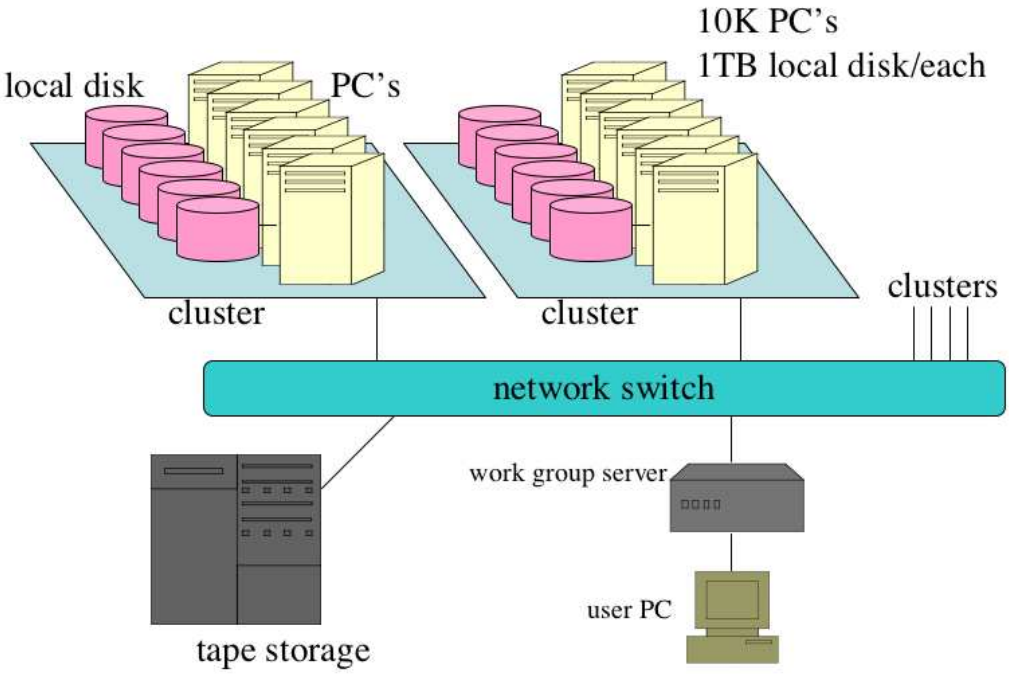

Figure 3.77: Conceptual drawing of computing model 2.

available data. Currently we store data file attributes in a postgreSQL database, and this is used as "metadata" in user analyses. This method could be extended by adding functionalities. The gfarm software which is being developed at AIST can be used to manage data on more than ten thousand PC's, making each "dataset" completely parallel [57].

3.8.6 Regional centers

The computing resources outside KEK should be effectively utilized, and creating regional centers is one of the most important issues. KEK can be a tier-0 site and we like to have several tier-1 centers outside KEK. In each regional center, a replica of the datasets will be available and data processing such as MC production can be performed in a coherent manner. Users at remote sites then do not need login to the KEK computers to analyze event data.

The network between KEK and centers should be at least 10 Gbps. Inside Japan, the extension of Super-SINET between universities can play an essential role in network connectivity. The network speed between Japan and foreign countries is also important and should be improved.

GRID technology can be used for data exchange among centers. For example, the data distribution among centers could be managed by the Storage Resource Broker (SRB) [58], which is now being used in several experimental groups. The user job transfer among regional centers could be possible by combining GRID middleware with the present utilities. The global security issue should be settled, and we have to discuss certificate authoriy signing policies when the GRID technology is employed.

GRID computing is being tested at the KEK Computing Research Center and other institutes. The collaborative work with them should be made for effective progress in this field. Moreover, computing technology in other fields such as biology and astrophysics could be applicable to our experimental data processing and user physics analyses.

3.8.7 Skims for physics analysis

The physics skims, which are the starting datasets for user analyses, have to be created in a more organized way because it is not realistic for all users to go through the entire dataset for their analyses when more than 1 ab^{-1} of beam data are accumulated. This is also true for the MC data sample. To control this, physics skims should be coordinated and be implemented into the event processing stream. Furthermore, turn-around in producing physics skims should be quick and flexible as we like to easily add more skim streams and we like to change skim conditions coded in the program.

At present, physics skims are stored in an "index" format, which contains only the information pointing to a mother event data file. This scheme siginificantly reduced the size of skim data. However, access to the mother event data can become a bottleneck when a large number of users try to read their skims at the same time. To avoid this, mother data sets have to be distributed appropriately, or we need another solution to solve this problem. In a distributed data system, a job control system based upon the data location that is accessed in a user job will be necessary to find the best host to run a job, which can avoid unnecessary network traffic.

3.8.8 Facilities

To accommodate the above described system, a facility with 3 MW of electricity and cooling power and at least 400 square meters of space is required. 200 racks for compute nodes only requires about 200 square meters of space and 2.4 MW of electricity. The area for the robotic tape machine should also be considered. One 150 TB capacity device typically occupies 1 m^2 area with some additional space for maintenance work.

The facility should have enough space for future extension of the computing system as more data are accumulated.

3.8.9 Software

The baseline software for the new system is what we are using at Belle; the B.A.S.F. framework and PANTHER data format. Possible improvements have been discussed in Belle software taskforce meetings. The implementation of ROOT in the current framework, for instance, is one of the important items. Other software utilities such as a bug tracking mechanism should be installed.

The biggest issue in software is deciding when we should move from GEANT3 to GEANT4 for simulation packages. We have been using GEANT3 since the beginning of the experiment. However, according to recent studies around the world, it is preferable to switch to GEANT4. This requires a huge amount of work and a careful check has to be performed. Once we decide to switch, the working group should be organized and an extensive effort has to be made.

3.8.10 Plan

The contract for the present KEK B-computing system will expire in Jan. 2006, and the specification of the next system has to be finalized by spring 2005 to allow enough time for bidding. Technology choices have to be made by this time. Note that the next contract will be for 5 years until Jan. 2010 for budgetary reasons. This is apparently far long considering the rapid speed of developments and/or changes in the computing industries. Therefore, we must first select the computing model we will have and then seriously take into account possible extensions, in particular for CPU and disk storage.

Tests of key software components such as the GRID middleware, for example, SRB and gfarm have to be carried out in 2004 and the results should be reflected in the design of the next computing system.

References

[1] E. Nygård *et al. Nucl. Instr. and Meth.* **A301** (1991) 506. O. Toker *et al.*, *Nucl. Instr. and Meth.* **A340** (1994) 572.

[2] M. Hazumi, Nucl. Instrum. Methods Phys. Res. A **473**, 1 (2001); Belle Collaboration, A. Abashian *et al.*, Nucl. Instrum. Methods Phys. Res. A **479**, 117 (2002); Y. Ushiroda, Nucl. Instrum. Methods Phys. Res. A **511**, 6 (2003).

[3] A. Abashian *et al.* (Belle Collaboration), Nucl. Inst. Meth. A **479**, 117 (2002).

[4] T.Iijima *et al.*, *Nucl. Instrum. Methods* A **379**, 457 (1996); T.Iijima *et al.*, *Nucl. Instrum. Methods* A **387**, 64 (1997); R.Suda *et al.*, *Nucl. Instrum. Methods* A **406**, 213 (1998), M.H.R.Khan *et al.*, *Nucl. Instrum. Methods* A **413**, 201 (1998); T.Sumiyoshi *et al.*, *Nucl. Instrum. Methods* A **433**, 385 (1999).

[5] H.Kichimi *et al.*, Proceedings of the 7th International Conference on Instrumentation for Colliding Beam Physics, Hamamatsu, Japan, November 15-19, 1999, submitted to *Nucl. Instrum. Methods* A; H.Kichimi *et al.*, *Nucl. Instrum. Methods* A **325**, 451 (1993).

[6] S.Uno, *Nucl. Instrum. Methods* A **379**, 421 (1996); K.Emi *et al.*, *Nucl. Instrum. Methods* A **379**, 225 (1996); S.Uno *et al.*, *Nucl. Instrum. Methods* A **330**, 55 (1993).

[7] B. Aubert *et al.* (BaBar Collaboration), Nucl. Inst. Meth. A **479**, 54 (2002); J. Schwiening, Nucl. Inst. Meth. A **502**, 67 (2003); See the following URL for more recent information, http://www.slac.stanford.edu/BFROOT/www/Detector/DIRC.

[8] A. Ali and A. Y. Parkhomenko, Eur. Phys. J. **C23**, 89 (2002).

[9] A. Abashian *et al.* (Belle Collab.), "The K(L)/Mu Detector Subsystem for the BELLE Experiment at the KEK B-Factory", *Nucl.Instrum.Meth.A449:112-124,2000*

[10] K. Abe (Belle Collab.), "RPC and Muon Detection at BELLE", *talk given at Belle-BaBar Workshop; February 14-16, 2002, Vancouver, British Columbia, Canada*

[11] M.Akatsu et al., Nucl. Instr. Meth. A **440**, 124 (2000); T.Ohshima, ICFA Instrum. Bull. 20, 2 (2000); T.Ohshima, Nucl. Instr. Meth. A **453**, 331 (2000).

[12] B. Aubert *et al.* (BaBar Collaboration), Nucl. Inst. Meth. A **479**, 54 (2002);

[13] M.Hirose et al., Nucl. Instr. Meth. A **460**, 326 (2001).

[14] Talks presented by K.Inami and also by A.Drutskoy at the Super B Factory Workshop in Hawaii (2004).

[15] M.Cantin et al. Nucl. Instr. Meth. **118** (1974) 177.

[16] A.Abashian et al., Nucl. Instr. and Meth. A **479** (2002) 117.

[17] T.Sumiyoshi et al., Nucl. Instr. and Meth. A **433** (1999) 385.

[18] T.Iijima et al., Nucl. Instr. and Meth. A **453** (2000) 321.

[19] I. Adachi et al., Nucl. Instr. and Meth. A **355** (1995) 390390; T. Sumiyoshi et al., J. Non-Cryst. Solids **225** (1998) 369.

[20] D.E.Fields et al. Nucl. Instr. Meth. A **349** (1994) 431.

[21] N.Akopov et al. Nucl. Instr. Meth. A **479**(2002) 511.

[22] T.Ypsilantis and J.Seguinot, Nucl. Instr. Meth. A **368** (1995) 229.

[23] T.Iijima, "Aerogel Cherenkov Counter in Imaging Mode", JPS Meeting, Tokyo Metropolitan University, September 1997.

[24] DEP catalog

[25] I. Adachi et al., "Test of a proximity focusing RICH with aerogel as radiator", Proceedings for the IEEE Nuclear Science Symposium, Norfolk, VA, November 10-15, 2002; hep-ex/0303038; T.Iijima et al., Nucl. Instr. Meth. A **502** (2003) 231.

[26] T. Matsumoto et al., to be published in NIM A; physics/0309032.

[27] H8500 data sheet, Hamamatsu Photonics K.K.

[28] aerogel transmission

[29] Hamamatsu Photonics K.K.

[30] Matsushita Electric Works Ltd. has a Japanese patent (No. 2659155) for usage of DMF as solvent to make aerogel.

[31] A.R. Buzykaev et al. , Nucl. Instr. Meth. A **433** (1999) 396.

[32] H.Ikeda et al., Nucl. Instr. Meth. A **372** (1996) 125.

[33] M. Artuso et al., Nucl. Instr. Meth. A **502** (2003) 91.

[34] Ideas SA, Oslo.

[35] K. Kazui *et al. Nucl.Instrum.Meth.A394:46-56,1997* ,

[36] M. Tanaka, H. Ikeda, K. Tamai, M. Takemoto and H. Hayashii, it IEEE Trans. Nucl. Sci.,**41**(1993) 1208; KEK-Preprint 93-156.

[37] V. M. Aulchenko *et al. Nucl.Instrum.Meth.A379:491-494,1996* , H. S. Ahn *et al. Nucl.Instrum.Meth.A410:179-194,1998* , H. Ikeda *et al. Nucl.Instrum.Meth.A441:401-426,2000* .

[38] A. Para, "Solid Scintillator-based Muon Detector for Linear Collider Experiments", *Proceedings of the Linear Collider Workshop 2000 (LCWS2000); October 24-28, 2000, Batavia, pp 865-869*

[39] M. Guler *et al.*, "OPERA Experiment Proposal", *CERN/SPSC 2000-028 (2000)*

[40] B. Bobchenko *et al.*, "HERA-B Electromagnetic Calorimeter", *Proceedings of the VIII International Conference on Calorimetry in High Energy Physics; June 13-19, 1999, Lisbon, Portugal, pp 511-517*

[41] G. Bondarenko *et al.*, " Limited Geiger-mode Microcell Silicon Photodiode: New Results." Nucl.Instrum.Meth.**A**442, 187 (2000)

[42] P. Buzhan *et al.*, "An Advanced Study of Silicon Photomultiplier", *ICFA Instrum.Bull.23:28-41,2001*

[43] "Multianode Photomultiplier Tube R5900-00-M64", *HAMAMATSU, January, 1999*

[44] S. Boyarinov *et al.*, "Neutron and Gamma Sensitivity of Gas Detectors", *GEM TN-93-345*

[45] N. Koch, *et al.* Nucl.Instrum.Meth. **A 373** (1996) 387-405.

[46] W.R. Nelson, H. Hirayama and D.W. Rogers, SLAC-265; H. Hirayama and Y. Namito, KEK Internal 2000-4.

[47] http://wwwasd.web.cern/wwwasd/geant4/geant4.html

[48] K.L. Brown and Ch. Iselin, Decay TURTLE, CERN 74-2 (1974).

[49] S.K. Sahu, Belle Note 97-172.

[50] GEANT3: Detector Description and Simulation Tool, CERN Program Library Long Writeup W5013 (1993).

[51] S. Stanic, Belle Note 341.

[52] T. Weiland, DESY 84-006 (1984).

[53] Y.H. Chin, LBL-35258 (1994).

[54] I. Adachi *et al.*, proc. in CHEP03, La Jolla, California, March 24-28, 2003.
I. Adachi *et al.*, presented at ACAT03, Tsukuba, KEK, December 1-5, 2003.

[55] National Institute of Informatics. `http://www.sinet.ad.jp/s_sinet/`.

[56] LHC Computing Grid Project. `http://lcg.web.cern.ch/LCG/`.

[57] O. Tatebe *et al.*, proc. in CHEP03, La Jolla, California, March 24-28, 2003. `http://www.gtrc.aist.go.jp/en/index.html`.

[58] San Deigo supercomputer center at UCSD. `http://www.npaci.edu/DICE/SRB/`.

[59] M.Nakao, *et al.*, "Switchless Event Building Farm for Belle", IEEE Trans. on Nucl. Sci. **48**, 2385 (2001)